Non-Commensurate Epitaxy of Organic Layers

Dissertation
zur Erlangung des akademischen Grades

doctor rerum naturalium (Dr. rer. nat.)

seit 1558

vorgelegt dem Rat der Physikalisch-Astronomischen Fakultät
der Friedrich-Schiller-Universität Jena

von Dipl.-Phys. Matthias Meißner
geboren am 15.07.1984 in Berlin-Marzahn

1. Gutachter: Prof. Dr. rer. nat. Torsten Fritz (Friedrich-Schiller-Universität Jena)

2. Gutachter: Prof. Dr. rer. nat. Christian Kumpf (Forschungszentrum Jülich)

3. Gutachter: Prof. Dr. phil. et rer. nat. Christian Loppacher Voirol (Aix-Marseille Universität, Frankreich)

Tag der Disputation: 22.09.2016

I have yet to see any problem, however complicated, which, when you looked at it in the right way, did not become still more complicated.

Poul William Anderson

Kurzfassung

Das Verständnis der Mechanismen hochgeordneten Wachstums, sprich der Epitaxie, dünner Schichten aus organischen Molekülen ist entscheidend für die kontrollierte Herstellung und weitere Effizienzsteigerung organischer Dünnschichtelektronik auf Basis optimierter Grenzflächen und Schichtstrukturen. In dieser Arbeit wird hierzu zunächst eine umfassende Übersicht über den aktuellen Wissensstand gegeben, um mit historisch bedingten doppelten Bedeutungen oder Widersprüchen in der Terminologie der Epitaxietypen aufzuräumen und gleichzeitig die Grundlagen für ihre Unterscheidbarkeit in Experiment und Theorie zu legen. Ein besonderer Fokus liegt hier auf der Abgrenzung von Epitaxietypen auf Grundlage regelmäßiger Gitterstrukturen gegenüber der sogenannten Orientierungsepitaxie, die minimale Auslenkungen von Atomen aus ihren Gitterplätzen heraus postuliert und somit Kristalle beschreibt, die nicht strikt periodisch sind. In diesem Zusammenhang wird die in der Literatur meist kompliziert dargestellte Beugungstheorie modulierter Strukturen aufgegriffen, um sie durch vereinfachende Annahmen greifbarer zu machen und sie auf den Fall von niederenergetischer Elektronenbeugung (LEED) anzuwenden. Anhand beispielhafter Beugungsexperimente an Strukturen wie Graphen auf Siliciumcarbid oder Blei-Phthalocyanin auf Graphit und vergleichender Rechnungen werden die wichtigsten Konsequenzen der Modulation von Atom-/Molekülgittern für LEED untersucht. Es wird dabei eine Möglichkeit dargelegt, die Epitaxierelation zwischen der Schicht und dem Substrat in vielen Fällen hochgenau mittels LEED oder Rastertunnelmikroskopie zu bestimmen. Zuletzt münden viele dieser Schlussfolgerungen und methodischen Ansätze in der umfassenden Aufklärung der Struktur einer Monolage Hexa-*peri*-hexabenzocoronen auf Graphit. Es wird gezeigt, dass sie ein Beispiel der Orientierungsepitaxie darstellt, indem die dazu notwendigen minimalen Auslenkungen der Moleküle mittels Rastertunnelmikroskopie direkt gemessen und durch ein Modell auf Grundlage von Dichtefunktionaltheorie-Berechnungen als alleinige Ursache für die Schichtorientierung ausgemacht werden können. Die Datenlage für dieses System stellt den ersten eindeutigen und direkten Nachweis dieses Effektes dar und ermöglicht in Zukunft seine Modellierung und Berücksichtigung auch in anderen Schichten aus organischen Molekülen.

Contents

1 Introduction

The field of organic electronics is flourishing amidst successful applications and favorable conditions in the entertainment and energy sectors. It is based on the discovery that organic materials, such as polycyclic aromatic molecules or polymers, can be semiconductive or even conductive [1]. While the conductivity is lower than in inorganic materials, organics feature a higher degree of flexibility than inorganic materials without significantly further decreasing conductivity [2, 3]. Since organic field effect transistors (OFETs) have been created [2], flexible electronic devices are conceivable and have been demonstrated [4]. Another outstanding attribute of organic chemistry is that such organic semiconductors can be tailored to feature a broad range of optical absorption (and emission) characteristics [5]. This allows for devices with unique properties such as flexible high-contrast displays [6], transparent organic light-emitting diodes (OLEDs) [7], or flexible solar cells [8].

While in inorganic semiconductors p-n junctions can be created in the same material (e.g., silicon) by using different dopants in relatively low concentrations, typically stacks or mixtures of different combinations of organic materials are needed in organic electronics. In fact, it is common that an organic electronic device consists of a large number of layers with different organic materials and inorganic electrodes [6]. Each layer or interface between layers serves a special purpose. There may be injection, extraction, transport, and blocking layers for charge carriers or excitons, all sandwiched between potentially different electrode materials [9]. In order to achieve high efficiencies, every layer or interface needs to be carefully optimized. For several reasons, much of the research is concerned with well-ordered molecular films: While in industrial applications polycrystalline films are often more cost-effective, it is films with a high degree of long-range order that excel in performance since low molecular order [10, 11] and grain boundaries [12] reduce the charge carrier mobility. Moreover, even in thicker organic films charge transport may be dominated by only a few monolayers close to an interface [12]. And finally, the fundamental properties and mechanisms governing molecular layers and interfaces can usually be studied more easily and selectively with thin well-ordered structures. Therefore, it is important to understand, characterize, and control ordered growth of molecular layers.

Often, the method of choice to obtain such ordered molecular structures is organic molecular beam epitaxy (OMBE), in which molecules are slowly evaporated onto a crystal surface from a crucible mounted to an ultra-high vacuum (UHV) chamber. Under such conditions, many molecular species are known to form crystalline structures on the surface with distinct orientations that are governed by the underlying crystal [13]. This is the phenomenon of epitaxy, which is derived from Greek and can be read as “on top, in an ordered manner”. For decades, the epitaxy of inorganic layers has been studied and usually fits into rather simple models within which the epitaxial orientations of the layers could be understood or even predicted. With the rise of organic epitaxy, the increased complexity of the molecular species compared to inorganic material was accompanied by an increased complexity in models needed to explain epitaxial orientations of molecular films, many of which are not consistent with the so-called commensurate epitaxy [13]. And while a lot of progress has been made in that respect, there is still much room for improvement. Due to the long history of epitaxy models there are common misconceptions about epitaxy mechanisms and terms therefor. Moreover, improvements in experimental techniques such as electron diffraction and scanning tunneling microscopy have not been exploited to full extent when it comes to the determination of the epitaxial relation of molecular layers which could lead to more insight into molecular interactions with the substrate.

Therefore, this work aims to improve the experimental determination and characterization of epitaxy types governing the growth of highly ordered molecular films as well as the understanding of the mechanisms driving the epitaxy of organic molecules. First, an up-to-date, comprehensive classification of epitaxy types is given. Thereby, the foundation is laid for their experimental distinction and for the discussion of potential energy calculations for epitaxial layers. Thereafter, it is discussed which implications for diffraction experiments, especially for low-energy electron diffraction (LEED), arise from non-commensurate epitaxy types that are typical for molecular layers. For this, a simplified theoretical treatment in the form of a derivation of a structure factor for such cases allows for a quite intuitive and helpful insight into an otherwise complicated diffraction theory of modulated structures. On that basis, a procedure to improve the experimental determination of the epitaxial relation between a non-commensurate film and the substrate is described and tested with exemplary structures, using LEED or scanning tunneling microscopy (STM). Finally, the combination of these findings allows for the clarification of the epitaxy in an interesting system, namely a monolayer of the molecule hexa-*peri*-hexabenzocoronene adsorbed on graphite. By applying state-of-the-art analysis of LEED and STM images, as well as first-principle based potential energy calculations, it is shown that the system unequivocally represents an example of an epitaxy type called orientational epitaxy [14]. Moreover, the findings constitute the first direct prove of the mechanism leading to this type of epitaxy.

2 Experimental methods and materials

The experiments reported here are concerned with thin films of well-ordered organic molecules that are deposited on inorganic crystal surfaces by organic molecular beam epitaxy (OMBE). In the following, the used materials as well as the techniques for surface characterization and the details of the sample preparation will be introduced.

2.1 Organic and substrate materials

Organic substances

Polycyclic aromatic hydrocarbons (PAHs) are a class of organic molecules with interesting characteristics. They contain rings of sp^2-hybridized carbon atoms bonded with each other by forming hybrid orbitals from one s and two p orbitals. The bonds can be described as a combination of strong σ bonds within the ring plane, made of the hybrid orbitals, and weaker π bonds above and below the ring plane, originating from the remaining unhybridized p$_\mathrm{z}$ orbitals. Both the σ and the π bonding states are accompanied by anti-bonding σ^* and π^* states, respectively. This system of molecular orbitals (in the ground state) is filled with electrons according to Hund's rule [15], and the highest occupied molecular orbital (HOMO) and lowest unoccupied molecular orbital (LUMO) can be defined accordingly (cf. Fig. 2.1).

In an aromatic hydrocarbon the π (and π^*) states are conjugated, i.e., delocalized over multiple atoms, and account for many of the characteristic electronic and optical features of this class of molecules. However, whether or not a molecule is aromatic cannot be ascertained by a simple rule and rather depends on the existence of favorable symmetries in the molecule [18]. Because of the delocalization the electrons easily move throughout the conjugated system and hence the polarizability in that plane is relatively high [15]. More importantly, the optical absorption depends roughly reciprocally on the size of the delocalized electronic system [15] and therefore can be tuned by choosing the molecular material according to the desired optical properties.

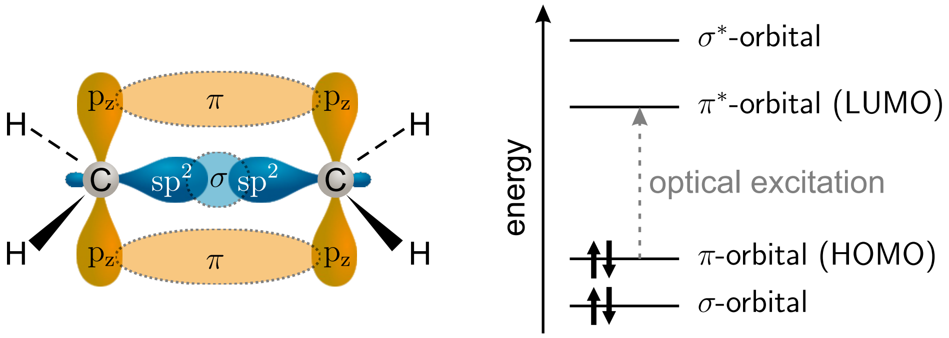

Figure 2.1: Schematic illustration of the σ and π bonds between two sp^2-hybridized carbon atoms in an ethylene molecule, and the corresponding molecular orbital diagram (based on [16] and [17]).

In this work, two different PAHs are deployed, namely lead phthalocyanine (PbPc) and hexa-*peri*-hexabenzocoronene (HBC) (cf. Fig. 2.2), both of which are large enough to feature absorption bands in visible light.

Phthalocyanines are chemically and thermally very stable molecules that are used as dye material [19, 20] and in OLEDs [21] or organic solar cells [22]. They can serve as ligands for the inclusion of metal atoms in their centers which can slightly change the molecular shape and therefore its packing behavior. In contrast to planar phthalocyanines such as zinc(II) phthalocyanine [23], the ligand slightly bends to a shuttlecock shape if large atoms like lead are incorporated [24]. However, different phthalocyanines are known to form similar square unit cells with sidelengths of ≈ 14 . . . 15 Å and flat-lying molecules when arranged in a single monolayer (ML) on different crystalline substrates [25–28]. For the experiments presented here, the PbPc material was purchased by the group of Prof. Dr. Toshiaki Munakata (Dept. of Chemistry, Osaka University, Japan) from Tokyo Chemical Industry (TCI) CO., LTD. in Tokyo, Japan. It was purified by the Munakata group in 3 temperature-gradient sublimation cycles.

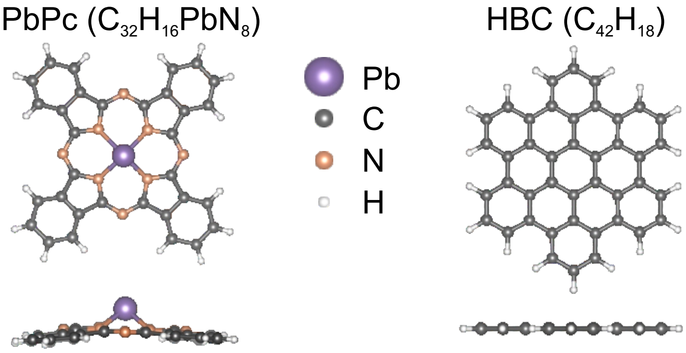

Figure 2.2: Experiments presented here involve these two molecules, lead phthalocyanine (PbPc) and hexa-*peri*-hexabenzocoronene (HBC). Their shape is given in top and side view, respectively.

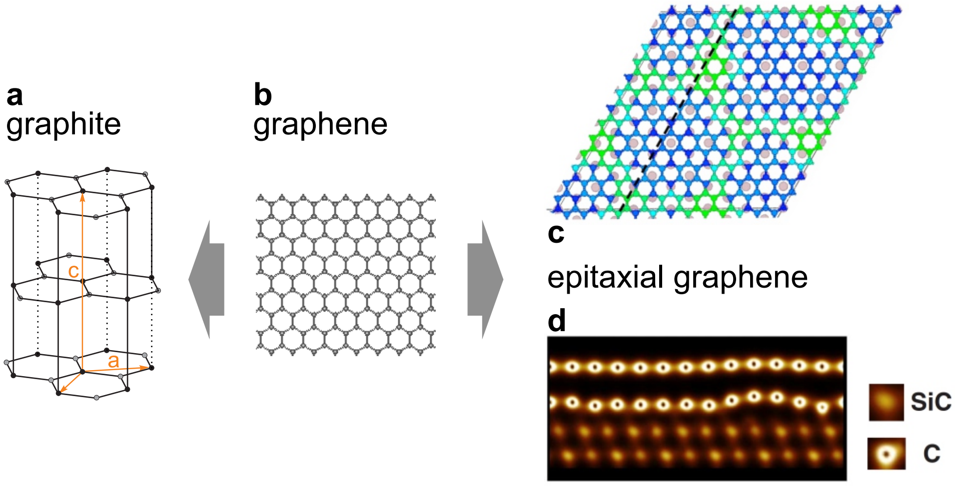

Figure 2.3: **a**) Crystal structure of graphite, adapted from [36]. The unit cell dimensions of graphite are $a = 2.461$ Å and $c = 6.71$ Å [37]. **b**) A single sheet of graphene. It can be regarded as a building block for both natural graphite (NG) and epitaxial graphene (EG). **c**) Top view of the corrugated carbon buffer layer (green and blue) on top of a SiC(0001) surface (brown). Blue carbon atoms lie lower than green ones. **d**) Side view of the buffer layer and one graphene sheet on top of SiC(0001). The lattice constant of the hexagonal SiC(0001) surface lattice is 3.073 Å [38]. Panels **c** and **d** were adopted from [39].

HBC is a planar molecule and a pure hydrocarbon. It features a high point symmetry (D_{6h}) and resembles a cutout of a sheet of graphene, albeit being hydrogen saturated. To emphasize this similarity, it has been dubbed nanographene by some authors [29, 30]. Due to its ability to form well-ordered films on different substrates [31–33] it is well suited for studying fundamental growth processes in organic epitaxy. Further, it served as ultra-thin but efficient decoupling layer for other organic molecules on gold [34] and is therefore potentially interesting for interface optimization. The HBC used here was synthesized and provided by the group Prof. Dr. Klaus Müllen (MPI for Polymer Research, Mainz, Germany). Details on the synthesis process can be found elsewhere [35]. The material was purified as well by means of temperature gradient sublimation.

Substrate material

Two forms of graphite are used as substrates for the molecular layers, namely single-crystalline natural graphite (NG) and few-layer epitaxial graphene (EG) grown on the (0001) face of silicon carbide (SiC) single crystals. NG features the standard hexagonal graphite crystal structure depicted in Fig. 2.3a. There, the honeycomb graphite sheets are arranged in ABAB (bernal) stacking. The crystals were obtained from Naturally Graphite, Michigan Technological University, and range in diameter between 3 and 5 mm.

EG growths epitaxially on SiC(0001) via evaporation of Si and graphitization of the excess carbon into one or few layers of graphene. This results in a large SiC(0001)$6\sqrt{3} \times 6\sqrt{3} - 30°$

commensurate superstructure which includes 13×13 graphene unit cells (cf. Fig. 2.3c), the hexagonal graphene lattice being rotated by 30° with respect to the hexagonal SiC surface lattice. Since the layer can include several graphene sheets, it can be regarded as few-layer graphene or very thin graphite. The graphitic character of this surface has long been known [40], however, its exact structure was contentious for long. While the original suggestion only involved a flat graphite layer, later investigations invoked more complex surface reconstruction models [41–43]. Today, the widely cited model is that of a honeycomb-like buffer layer with graphene sheets on top and SiC below [39, 44, 45]. However, in that buffer layer about every third carbon atom binds to an underlying adjacent silicon atom, leading to a corrugation of the buffer layer and preventing it from developing the special electronic properties of graphene [44, 45]. The density functional theory (DFT) calculations in Ref. [39] confirming the corrugation (cf. Fig. 2.3d) suggest that the buffer layer atoms bind to the silicon atoms if they lie close enough to each other. Hence the corrugation constitutes a real surface reconstruction observable in STM [39] and manifests the periodicity of the $6\sqrt{3} \times 6\sqrt{3} - 30°$ registry with the SiC substrate. It can even be reproduced approximately with a very simple model where the adsorption height of a buffer layer atom is scaled with its lateral proximity to the underlying silicon atoms [P1].

SiC can exhibit may polytypes that differ in terms of the order in which bilayers of silicon and carbon atoms are stacked on top of each other. The lattice constant of 3.073 Å of the hexagonal surface lattice, however, is the the same for the most common polytypes [38].

The EG on SiC(0001) samples used here were produced by Dr. Bernd Schröter (Institute for Solid State Physics, FSU Jena, Germany) via high-temperature annealing SiC in an argon atmosphere following a procedure proposed in Ref. [46] which allows for very uniform graphene growth. The pristine SiC samples (4H polytype) were purchased from Sterling Semiconductor. The nominal thickness was estimated previously to be $2 \ldots 3$ ML on the buffer layer via X-ray photoelectron spectroscopy [47].

2.2 Characterization techniques

Differential reflectance spectroscopy (DRS)

With differential reflectance spectroscopy (DRS) the reflectance R of a sample in vacuum is measured *in situ* as a function of time and photon energy E while depositing (organic) material. Details of the optical setup can be found elsewhere [48, 49]. In short, the light of a halogen or xenon lamp is focused onto, and reflected by, the sample at nearly normal incidence. DRS is capable of detecting relative changes in the reflectance of well below

10^{-3}. This is usually much less than the typical reflectance change in the visible range due to an adsorbed monolayer of aromatic polycyclic hydrocarbons (see Publication [P1] and the Supplementary Material of Publication [P7]). Therefore, it is possible to determine the nominal molecular layer thickness *in situ* with a resolution of typically 0.1 ML or better.

The DRS spectral signal is defined as the relative change of the reflectance R at a certain layer thickness d with respect to the reflectance of the bare sample ($d = 0$):

$$DRS(E, d) = \frac{R(E, d) - R(E, d = 0)}{R(E, d = 0)} \tag{2.1}$$

Typically, the spectra are accumulated over periods of 30 s each. From this measure it is possible to obtain the complex dielectric function of the layer on the substrate if that of the substrate is known from complementary measurements or from the literature. In this work, however, the optical properties of the overlayers are not as much of interest as the possibility of thickness control via DRS. The DRS spectra change in shape when the optical properties of the molecular layer change. In the case of Frank-van der Merwe (layer-by-layer) growth of the molecular layer, it has been found that the optical properties of thin molecular layers depend (sometimes drastically) on the number of monolayers that are stacked on top of each other [48]. In short, the reason is that, especially within the first ML of flat polycyclic aromatic molecules, their centers are relatively far away from each other as compared to a vertical stack of these molecules. In fact, on weakly interacting substrates the optical properties of the first ML are often found to closely resemble those of isolated molecular monomers, e.g., in a solution [P1, P3, P8]. Hence, the optical and electronic coupling can be much stronger when molecules start stacking on top of each other, changing the optical properties of the layer. Therefore, the layer thickness can be concluded via DRS under favorable circumstances, which is often the case. For this purpose, a measure called ΔDRS can be obtained from the data and is more sensitive to sudden changes within the molecular layer. It is defined as the relative change of reflectance compared to the preceding spectrum from the layer with thickness $d - \Delta d$, not to the bare substrate:

$$\Delta DRS(E, d) = \frac{R(E, d) - R(E, d - \Delta d)}{R(E, d - \Delta d)}. \tag{2.2}$$

The ΔDRS signal will be used for thickness control in the following. Note, however, that the first ML is not necessarily completely closed when the molecules start stacking on top of each other, depending on the growth dynamics. Therefore, it is useful to obtain information about the structure with complementary techniques, such as scanning tunneling microscopy (STM).

Scanning tunneling microscopy (STM)

If the surface structure of a sample shall be determined with atomic or molecular resolution in a non-destructive way, scanning tunneling microscopy (STM) is an ideal technique if the sample is sufficiently conductive. By bringing a metallic tip in close proximity to the surface ($\approx 0.1 \ldots 1$ nm) and applying a suitable bias voltage between tip and sample, a current can be measured because electrons tunnel through vacuum from occupied states of the sample into the tip and from the tip into unoccupied states of the sample. STM therefore approximately maps the so-called local density of states (LDOS) [50]. The tunnel current sensitively depends on the distance between tip and sample, exponentially decaying with increasing distance. Therefore, the sample surface can be imaged by scanning it with the tip and measuring the tunnel current or keeping the current constant by adjusting the tip-sample distance during the scan with a feedback loop.

Because of the strong distance sensitivity the topmost atom or atoms of the tip usually dominate the total tunnel current, and it is possible to achieve atomic or submolecular resolution with a sufficiently sharp tip. However, there can be physical limits to the resolution of structures. Since the above-mentioned π-conjugated electron system is delocalized over the entire molecule in the case of polycyclic aromatic hydrocarbons, the contrast is usually not atomic. However, depending on the bias voltage [51] or a functionalization of the tip [52] different molecular orbitals may be imaged.

Low-energy electron diffraction (LEED)

Besides imaging the surface of a crystal directly via STM it can be examined via diffraction experiments which can contain important information on the quality and structure of the surface. The most common diffraction technique for surface analysis is low-energy electron diffraction (LEED). Therein, electrons are accelerated with voltages of typically $\approx 10 \ldots 200$ V from an electron gun onto the sample in UHV and the particle-wave duality allows for an electron to diffract on the crystal. The interference pattern of the backscattered electrons is detected by a phosphorous screen or a channeltron detector. Except for spot-profile analysis LEED devices, that are not used here, inelastically scattered electrons are partially filtered by a series of two to four spherical grids, depending on the individual setup. Due to the relatively low kinetic energy the electrons hardly penetrate the surface, by only one or few atomic layers of the crystal surface, before they are scattered inelastically [53]. Hence, the elastic scattering that produces sharp LEED patterns is very surface sensitive. More importantly, it allows for an easy observation of the sample's two-dimensional reciprocal surface lattice (cf. Sec. 4.1 for details).

The LEED devices from Scienta Omicron and OCI Vacuum Microengineering used here are equipped with microchannel plates (MCPs) to amplify the scattered electrons. This allows for a large reduction of the incident beam intensity and therefore beam-induced damage to the organic layers.

As-measured LEED images, especially those of MCP LEED devices, always suffer from systematic distortions due to imaging techniques, the device setup, or experimental conditions [P2, P4]. All LEED images discussed here are corrected for such distortions using the software LEEDCal [54] so that they provide a nearly undistorted view of the reciprocal space of the surface. This includes the correction of axial distortions occurring if the sample normal is tilted with respect to the incident beam in order to observe higher diffraction orders [P4]. The most important remaining source of error is the sample-surface-to-LEED distance. If this distance is different from the one used in the device calibration, the dominating effect is a deviating scaling of the resulting LEED image [P2]. The corrected and calibrated images are then analyzed with LEEDLab [55] to obtain geometric information about the sample's surface lattice via fitting of lattice parameters to many spots simultaneously.

2.3 UHV chamber overview and sample preparation

All molecular films prepared for this work were grown by OMBE in three ultra-high vacuum (UHV) chambers at base pressures of 10^{-9} mbar or better by evaporation from custom-made effusion cells. To allow for an overview, the chambers are labeled and the attached experimentation devices relevant for this work are listed in Table 2.1. Experiments involved two UHV chambers in Jena, Germany (chambers A and B) and one UHV chamber in Osaka, Japan (chamber C).

Prior to the introduction of NG samples into the vacuum they were glued to molybdenum sample holders with PELCO High Temperature Carbon Paste (purchased from Plano GmbH) and cleaved in air via tape exfoliation. After introduction into the vacuum, both NG and EG samples were heated by electron bombardment to temperatures > 800 K to remove any contaminants. Before any new deposition of organic material it was sufficient to heat all samples with an adjacent filament to temperatures that ensured a desorption of previously deposited molecular layers. Due to the lack of a reliable temperature calibration in chambers A and B the bare samples were examined with LEED for indications of remaining organic molecules (intensity rings, disks, or diffuse background). In the case of PbPc experiments in chamber C, after heating PbPc-covered samples to temperatures of ≈ 500 K (determined by a calibrated type K thermocouple) no such indications where observable anymore in LEED. Therefore a slightly higher cleaning temperature of ≈ 600 K was chosen for all succeeding experiments in that chamber.

Table 2.1: List of UHV chambers used for this work, including two chambers in Jena, Germany (chambers A and B) and one in Osaka, Japan (chamber C), including the experimentation techniques or devices relevant to further discussions.

chamber A	chamber B	chamber C
DRS	DRS	
OCI MCP LEED	Omicron MCP LEED	OCI MCP LEED
Specs JT-STM		

Thickness control in chambers A and B was facilitated via DRS based on characteristic changes in the spectral features of the first few molecular monolayers explained in the previous section. In chamber C the LEED device and molecule evaporator are mounted in such a geometry that LEED measurements could be performed during the material deposition. Hence, it was possible to judge the layer thickness from characteristic changes of the LEED patterns.

The STM measurements presented in this work were carried out in chamber A with a commercial device from SPECS Surface Nano Analysis. It can be cooled with liquid nitrogen (LN_2), liquid helium (LHe), and a Joule-Thompson cooling stage to a minimum temperature of 1.1 K. For all measurements, the tungsten KolibriSensors of SPECS were used. They are capable of conducting STM measurements as well as scanning force microscopy measurements at the same time. However, only the STM mode was used. Post-measurement image processing was performed with Gwyddion [56]. Every image has been corrected for plane tilt, additional image processing (if any) will be mentioned in the caption of each figure.

3 Classification of epitaxy

Historically, the term epitaxy refers to the phenomenon where a crystal grows on the surface of another such that both share a common two-dimensional lattice at the interface [57]. One can say that their lattices match each other and that lattice points of one crystal coincide with lattice points of the other. This understanding was based on the observation of crystals of different inorganic materials, naturally grown on top of each other. They assume fixed mutual alignments in which crystallographic directions of the adjacent crystals coincide. Nowadays, this amounts to so-called commensurate epitaxy.

However, in surface physics, and especially in the field of organic thin films, a wider variation of crystal growth modes required a more detailed classification of epitaxy for understanding observed film growth modes. Such a classification has been detailed in works of Hooks et al. [13] and Mannsfeld et al. [36, 58]. Assuming rigid crystals that can be described with perfect lattices the authors are able to explain a range of epitaxial systems which will therefore be referred to as examples of lattice epitaxy hereafter. This model is often sufficient to theoretically describe an energetic minimum of an adsorbate-substrate system and thereby the epitaxy between the two crystals. Since it is important for the presented work to strictly distinguish between different types of lattice epitaxy, an overview shall be given on the current state of knowledge in this regard. Thereby, it shall be attempted to simplify the historically grown list of names for lattice epitaxy types and to highlight the physical differences between the different types. Additional concepts not requiring perfect lattices to explain epitaxy will be introduced thereafter.

3.1 Lattice epitaxy

The term lattice epitaxy implies that a distinct relation between two crystals is based on their respective lattices. In the following, the 2D surface lattice of a substrate crystal generated by the primitive lattice vectors $\boldsymbol{s}_1$ and $\boldsymbol{s}_2$ and the 2D lattice of an overlayer (or adsorbate) crystal generated by the primitive lattice vectors $\boldsymbol{a}_1$ and $\boldsymbol{a}_2$ shall be considered. The relation between these lattices can be given using different notations.

The Wood notation [59] ascribes the term “substrate(surface orientation)”$|\boldsymbol{a}_1|/|\boldsymbol{s}_1| \times |\boldsymbol{a}_2|/|\boldsymbol{s}_2|$−“rotation angle” to an overlayer. The term contains the ratios of the respective vector lengths and a possible angle of rotation between the overlayer and the substrate, and it is useful to easily define some simple cases. However, the notation can fail in many cases of organic epitaxy due to incompatible symmetries, and, as Wood noted himself, it is not a unique definition and inferior to a description in terms of vectors. Therefore, the latter will be preferred in this work, except when referring to well-established overlayer structure names in Wood notation from the literature such as the SiC(0001)$6\sqrt{3} \times 6\sqrt{3} - 30°$ reconstruction. Specifically, the epitaxy matrix notation [13, 36, 58, 60] will be applied here. Therein, the so-called epitaxy matrix $\underline{C}$ links the primitive adsorbate vectors to the primitive substrate vectors, such that it satisfies the equation

$$\underline{A} := \begin{bmatrix} \boldsymbol{a}_1 \\ \boldsymbol{a}_2 \end{bmatrix} = \underline{C} \begin{bmatrix} \boldsymbol{s}_1 \\ \boldsymbol{s}_2 \end{bmatrix} =: \underline{C}\,\underline{S}, \tag{3.1}$$

with the matrices $\underline{A}$ and $\underline{S}$ containing the respective primitive vectors *as rows*.

Lattice epitaxy types can then be distinguished by discussing properties of the epitaxy matrix $\underline{C}$. An equally valid yet more instructive approach makes use of the reciprocal space equivalents of the respective lattices. The construct of reciprocal space is helpful in understanding diffraction experiments and essentially describes a real space structure in terms of directed, spatial frequencies. The adsorbate and substrate lattices in real space translate into respective lattices in reciprocal space and generated by primitive vectors $\boldsymbol{a}_i^*$ and $\boldsymbol{s}_i^*$, fulfilling the relations

$$\begin{aligned} \boldsymbol{a}_i^* \cdot \boldsymbol{a}_j &= 2\pi\delta_{ij} \\ \boldsymbol{s}_i^* \cdot \boldsymbol{s}_j &= 2\pi\delta_{ij} \end{aligned} \tag{3.2}$$

which can also be written as

$$\begin{aligned} \underline{A}^*\underline{A}^\top &= 2\pi\mathbb{1} \\ \underline{S}^*\underline{S}^\top &= 2\pi\mathbb{1}. \end{aligned} \tag{3.3}$$

Both concepts will be useful for this work. Therefore, Fig. 3.1 gives an overview of both the real space and reciprocal space classification of all possible lattice epitaxy types by means of general examples. In real space (left column), the lattice epitaxy types differ in terms of the registries of adsorbate lattice points with the substrate lattice. Note that in Fig. 3.1 only lattices without an atomic basis are displayed and compared to each other and that real atoms or molecules may be shifted with respect to the lattice points. In reciprocal space (right column), the differences lie in the reciprocal lattice points that

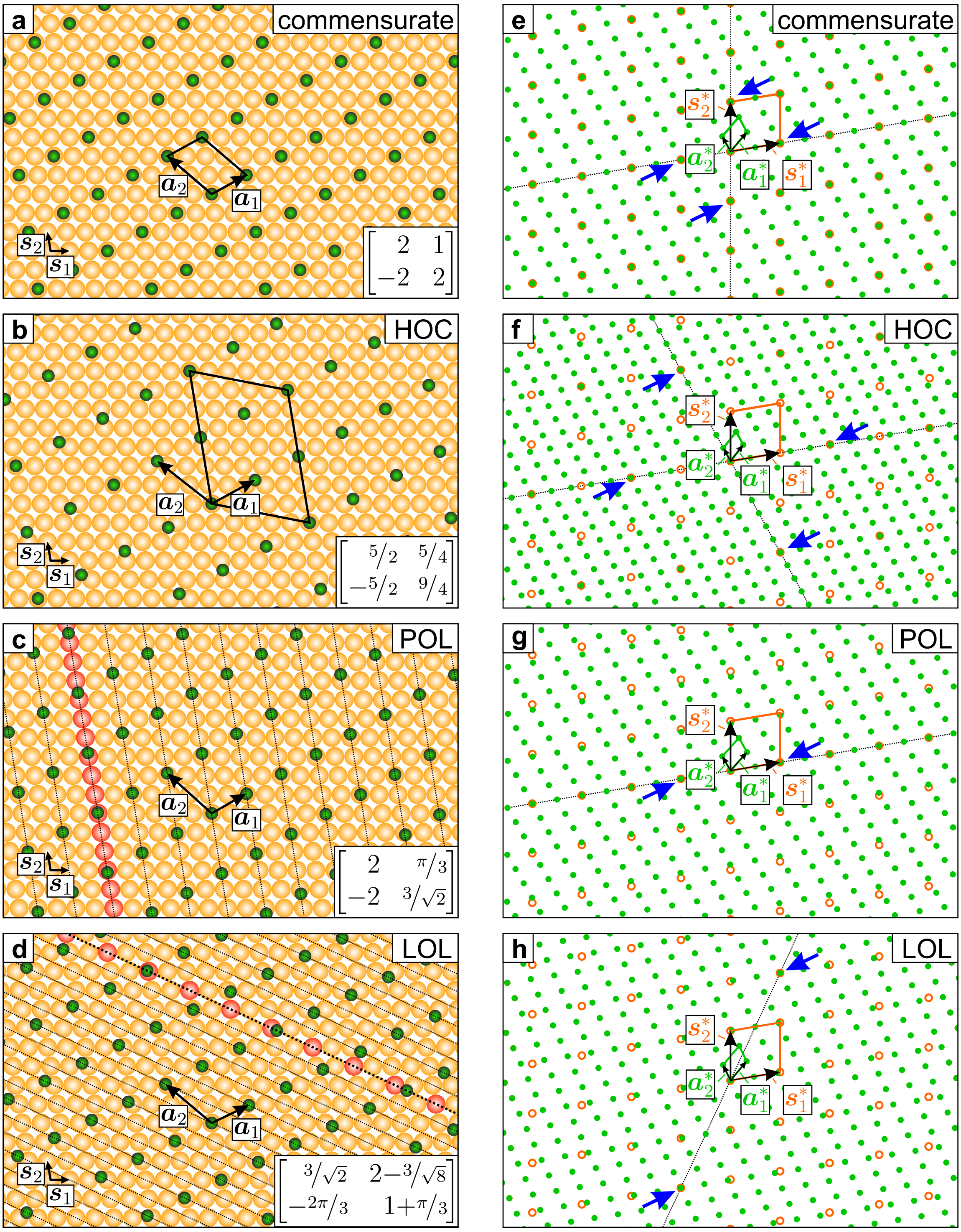

Figure 3.1: All types of lattice epitaxy in real (left column) and reciprocal space (right column). Commensurate and HOC types feature periodic coincidences of lattice points in both real space (**a-b**, smallest commensurate cells marked with black lines) and reciprocal space (**e-f**). Real space lattice points of point-on-line (POL) and line-on-line (LOL) types (**c-d**) lie on primitive and non-primitive substrate lattice lines, respectively (exemplary substrate lattice lines highlighted in red). Equivalently, in reciprocal space there is only a single direction of coincidences (**g-h**). Dotted lines mark matching lattice lines in real space and directions of coincidences in reciprocal space. Blue arrows mark exemplary coincidences.

coincide exactly and hence in the spatial frequencies that match each other.

3.1.1 Lattice epitaxy in real space

The given examples display two general cases in real space: a mutual arrangement of lattices which *is* two-dimensionally periodic, and one which *is not*. The **first group** consists of commensurate (cf. Fig. 3.1a) and higher-order commensurate (HOC) structures (cf. Fig. 3.1b). In the commensurate case, all adsorbate lattice points coincide exactly with substrate lattice points, while this is only true for a sub-group of HOC lattice points. In both cases, however, the mutual arrangements are periodic over the entire two-dimensional surface because the HOC unit cell produces a *supercell* that is *commensurate*. Generally, the supercell does not have a shape geometrically similar shape to the HOC unit cell because the substrate and adsorbate symmetries are combined (cf. Fig. 3.1b). The epitaxy matrix contains only integers for a commensurate structure and rational numbers in case of an HOC structure.

In the **second group**, each adsorbate lattice point has a unique registry with the substrate lattice – the arrangement is not periodic over the 2D surface. Therefore, they can be called non-commensurate. At first glance, it is not obvious why such a structural characteristic should provide any energetic advantage compared to an arbitrary orientation of the adsorbate lattice with respect to the substrate where the adsorbate lattice points have a statistical registry with the substrate lattice. However, at second glance, every overlayer lattice point in Fig. 3.1c lies on a primitive (1,0) substrate lattice line, while every overlayer lattice point in Fig. 3.1d lies on a non-primitive (1,2) substrate lattice line – the overlayer and substrate lattices share common sets of lattice lines. While the latter is true in both cases, it is useful from an adsorption energy point of view to distinguish between the case of primitive and non-primitive substrate lattice lines (cf. Sec. 3.1.3), and the two types have been termed point-on-line (POL) [61] and line-on-line (LOL) [58], respectively[a]. If conveniently defined (see the following paragraph), a POL epitaxy matrix features a column with integers and a column with irrational numbers – all points lying on lattice lines parallel to $\boldsymbol{s}_i$ correspond to the i^{th} column containing irrational numbers. The matrix of a LOL overlayer consists of exclusively irrational numbers as noted exemplarily in Fig. 3.1d.

---

[a] As a side note, the sharing of lattice lines is not to be confused with the necessary but not sufficient condition for lattice epitaxy that the $[1,1]$ adsorbate direction is parallel to the $[0,1]$ substrate direction in the POL example or that the $[\bar{1},1]$ adsorbate direction is parallel to $[\bar{2},1]$ of the substrate in the LOL example. The parallelism of lattice directions is not sufficient to ensure that all overlayer lattice points reside on the same set of substrate lattice lines.

The distinction between POL and LOL is somewhat ambiguous since a lattice can be defined based on different sets of primitive lattice vectors, and what is a non-primitive lattice line in one set may be primitive in another. However, following the conventional definition of 2D Bravais lattices, this ambiguity affects only the case of a hexagonal substrate: For every definition of two primitive substrate lattice vectors there exists a third lattice vector that is equivalent, but is not primitive in the sense of Equ. 3.1. As a consequence, if the substrate lattice is chosen such that all overlayer lattice points of a POL structure lie on substrate lattice lines parallel to that third vector, the epitaxy matrix also contains only irrational numbers. However, this special case can be recognized by both line differences being integers (if $\angle(\boldsymbol{s}_1, \boldsymbol{s}_2) = 120°$) or both line sums being integers (if $\angle(\boldsymbol{s}_1, \boldsymbol{s}_2) = 60°$) [62]. Since the distinction of lattice epitaxy types by means of the epitaxy matrix can obviously be challenging, it is highly recommendable to resort to the means of reciprocal space (cf. Sec. 3.1.2).

The irrationality of (some of) the matrix elements prevents a 2D periodic registry of POL/LOL structures with the substrate and sets them apart from commensurate or HOC ones. This may seem only of academic interest since, of course, an experimental determination of the epitaxy relation will always have a finite error margin. Therefore, it can never be concluded with certainty from an experiment whether a matrix element is truly irrational or a fraction of very large integers. However, energetic preference can be explained analytically even for irrational epitaxy matrices (see Sec. 3.1.3), thereby advancing the understanding of epitaxy from 2D periodic to more general cases and justifying the classification.

3.1.2 Lattice epitaxy in reciprocal space

The non-commensurate epitaxy types POL/LOL, but also the HOC type, may be difficult to be identified in real space. However, the mentioned sharing of lattice points or lines translates into a coincidence of lattice points in reciprocal space [58], since the orientation and magnitude of each reciprocal lattice vector represent the orientation and separation of a set of real space lattice lines – the spatial frequencies match in the corresponding directions. And such coincidences usually can be analyzed more easily and objectively than atomic or molecular positions with respect to the substrate.

The right column of Fig. 3.1 shows the reciprocal lattices corresponding to the examples in the left column. The commensurate and HOC types feature coincidences with the substrate lattice in more than one direction (cf. panels e and f of Fig. 3.1). This is tantamount to the 2D periodicity for both types since in two independent directions their lattices match in both orientation and lattice line separation. In a reverse fashion compared to the real space, in the commensurate case all reciprocal substrate lattice points (including the primitive ones) coincide with overlayer lattice points, while in the HOC case only a subset of substrate spots coincides with overlayer lattice points, partly or completely excluding the primitive substrate points.

The POL example displays coincidences only with one primitive reciprocal substrate vector and multiples thereof, hence only in one reciprocal lattice direction. LOL-type adsorbate lattice points only coincide with a non-primitive reciprocal substrate lattice point and multiples thereof. Both epitaxy types therefore share only one distinct set of lattice lines – one could say their lattices match only in one dimension, not in two as in the case of commensurate and HOC types. However, it has been shown that such a coincidence of reciprocal lattice points *can* produce an energy minimum for such a mutual orientation of lattices compared to an arbitrary orientation [63, 64]. The formalism to this important concept will be briefly addressed next.

3.1.3 Energy minima due to reciprocal space coincidences

Different approaches have been pursued to predict the epitaxial alignment of an adlayer on a substrate, purely based on geometry or based on actual energy calculations in search for energetically preferred arrangements. Especially in the community of epitaxial layers of organic molecules epitaxy types are common that do not fit into the commensurate category [58, 65–68]. Due to the lack of (small) commensurate unit cells in such cases, a realistic calculation of the adsorption energy had to cover a sufficiently large overlayer domain. Since this proved computationally too demanding in the past, models with different levels of simplification have been applied previously. Hoshino et al. proposed a geometric measure for the magnitude of deviation of adsorbate lattice points from the nearest substrate lattice points [61], later termed local misfit sum [36, 60, 62]. Though this measure is not directly related to the adsorption energy of an overlayer it has been shown that it features distinct minima for the different types of lattice epitaxy [61, 62]. Subsequently, but before the discovery of the LOL epitaxy type, it was argued that this geometric calculation can be omitted in favor of a simple analysis of the epitaxy matrix elements, searching for overlayer orientations which allow for integer matrix elements within a given margin of lattice parameters [62]. While this approach is obviously not applicable to LOL structures due to their irrational epitaxy matrices, it has been generalized [36] to a search of integer number pairs (h, k) and (m, n) that satisfy the equation

$$\begin{pmatrix} h \\ k \end{pmatrix} = \underline{C} \begin{pmatrix} m \\ n \end{pmatrix}. \tag{3.4}$$

If such pairs exist then the reciprocal adsorbate lattice vector $\boldsymbol{G}_{hk}^{\text{ads}} = h\boldsymbol{a}_1^* + k\boldsymbol{a}_2^*$ coincides with the reciprocal substrate vector $\boldsymbol{G}_{mn}^{\text{sub}} = m\boldsymbol{s}_1^* + n\boldsymbol{s}_2^*$ and a corresponding type of lattice epitaxy can be inferred (cf. Section 3.1.2). This is tantamount to simulating the reciprocal lattices geometrically based on the epitaxy matrix and looking for a coincidence of lattice points directly.

Others attempted to calculate a measure crudely proportional to the adsorption energy of an overlayer domain with a given lattice: They approximated the adsorbate-substrate potential energy $E_{\text{ads-sub}}^{\text{single}}$ of a single overlayer particle with a cosine function and summed the respective phase terms of the cosine corresponding to the registries of the adsorbate lattice points with the substrate lattice to obtain the domain energy $E_{\text{ads-sub}}^{\text{domain}}$ [60]. More sophisticated approaches to calculate actual adsorption energies of domains consisting of aromatic polycyclic hydrocarbons on different substrates relied on force-field calculations to model atomic interactions, applying various methods of simplification to keep numerical costs manageable [69, 70]. Such methods included that all molecules in a domain remained rigid and their positions and orientations were exactly repeated with the unit cell, i.e., the domain structure was strictly periodic.

Both the cosine and the force-field approaches have in common that they feature distinct minima in $E_{\text{ads-sub}}^{\text{domain}}$ when the adsorbate and substrate lattices share common sets of lattice lines. A minimum in $E_{\text{ads-sub}}^{\text{domain}}$ alone does not automatically predict a minimum in the total adsorption energy because intralayer interactions within the adsorbate layer might prohibit such a mutual arrangement with the substrate. However, obviously, a minimum in $E_{\text{ads-sub}}^{\text{domain}}$ is a necessary condition for (and the physical meaning behind) lattice epitaxy. And in turn, it has been shown for rigid lattices that a necessary condition for the existence of such a minimum in $E_{\text{ads-sub}}^{\text{domain}}$ is a coincidence of reciprocal lattice vectors of the adsorbate and the substrate, respectively [58, 63, 64, 71]. This crucial fact will be briefly demonstrated again below, thereby providing a full derivation which is not available in the cited works.

Assuming strictly additive potential energies at zero Kelvin, the adsorbate-substrate energy of a crystalline overlayer domain is generally obtained by summing the single adsorbate particle's contribution $E_{\text{ads-sub}}^{\text{single}}(\boldsymbol{R} + \boldsymbol{\Delta})$ over all adsorbate lattice vectors $\{\boldsymbol{R}\}$, where $\boldsymbol{\Delta}$

represents a rigid shift of the entire adsorbate domain:

$$E_{\text{ads}-\text{sub}}^{\text{domain}} = \sum_{\{\boldsymbol{R}\}} E_{\text{ads}-\text{sub}}^{\text{single}}(\boldsymbol{R} + \boldsymbol{\Delta}). \tag{3.5}$$

Since the substrates considered here are periodic crystals, $E_{\text{ads}-\text{sub}}^{\text{single}}(\boldsymbol{R})$ can be expanded into a Fourier series

$$E_{\text{ads}-\text{sub}}^{\text{single}}(\boldsymbol{R}) = \sum_{\{\boldsymbol{G}^{\text{sub}}\}} \varphi(\boldsymbol{G}^{\text{sub}}) \mathrm{e}^{-i\boldsymbol{G}^{\text{sub}}\cdot\boldsymbol{R}} \tag{3.6}$$

of reciprocal substrate lattice vectors $\{\boldsymbol{G}^{\text{sub}}\}$ giving:

$$\begin{aligned} E_{\text{ads}-\text{sub}}^{\text{domain}} &= \sum_{\{\boldsymbol{R}\}} \sum_{\{\boldsymbol{G}^{\text{sub}}\}} \varphi(\boldsymbol{G}^{\text{sub}}) \mathrm{e}^{-i\boldsymbol{G}^{\text{sub}}\cdot\boldsymbol{R}} \mathrm{e}^{-i\boldsymbol{G}^{\text{sub}}\cdot\boldsymbol{\Delta}} \\ &= \sum_{\{\boldsymbol{G}^{\text{sub}}\}} \varphi(\boldsymbol{G}^{\text{sub}}) \mathrm{e}^{-i\boldsymbol{G}^{\text{sub}}\cdot\boldsymbol{\Delta}} \sum_{\{\boldsymbol{R}\}} \mathrm{e}^{-i\boldsymbol{G}^{\text{sub}}\cdot\boldsymbol{R}}. \end{aligned} \tag{3.7}$$

The factor

$$L = \sum_{\{\boldsymbol{R}\}} \mathrm{e}^{-i\boldsymbol{G}^{\text{sub}}\cdot\boldsymbol{R}} \tag{3.8}$$

is sometimes called the lock-in term [14, 70, 72]. In the limit of infinite lattices, i.e., if the adsorbate domain is large enough, it will average the sum to zero unless $\boldsymbol{G}^{\text{sub}}$ matches a reciprocal adsorbate lattice vector $\boldsymbol{G}^{\text{ads}}$. This can be understood via the so-called "Dirac comb" of Dirac delta functions $\sum_{m=-\infty}^{\infty} \delta(\tau - m)$ and its Fourier series representation $\sum_{m=-\infty}^{\infty} \delta(\tau - m) = \sum_{m=-\infty}^{\infty} \mathrm{e}^{-2\pi i m\tau}$ [73]. The adsorbate lattice vector $\boldsymbol{R}$ in Equ. 3.7 can be written as an integer linear combination of primitive vectors $\boldsymbol{R} = m\boldsymbol{a}_1 + n\boldsymbol{a}_2$, and the reciprocal substrate vector $\boldsymbol{G}^{\text{sub}}$ as an *arbitrary* linear combination of *reciprocal* primitive vectors $\boldsymbol{G}^{\text{sub}} = \alpha\boldsymbol{a}_1^* + \beta\boldsymbol{a}_2^*$. In combination with Equ. 3.2 this leads to a lock-in term of $\sum_{m,n} \mathrm{e}^{-2\pi i m\alpha} \mathrm{e}^{-2\pi i n\beta} = \sum_{m,n} \delta(\alpha - m)\delta(\beta - n)$. The coefficients α and β must hence be any pair of integers for the term not to disappear. This in turn corresponds to $\boldsymbol{G}^{\text{sub}}$ equaling a reciprocal adsorbate lattice vector $\boldsymbol{G}^{\text{sub}} = \boldsymbol{G}^{\text{ads}} = m\boldsymbol{a}_1^* + n\boldsymbol{a}_2^*$. The component-wise representation of the original sum over real space lattice vectors can therefore be written as a sum over reciprocal adsorbate vectors $\sum_{m,n} \delta(\alpha - m)\delta(\beta - n) = \sum_{\{\boldsymbol{G}^{\text{ads}}\}} \delta(\boldsymbol{G}^{\text{sub}} - \boldsymbol{G}^{\text{ads}})$[b].

Making use thereof and separating the $\boldsymbol{G}^{\text{sub}}$-independent term with $\varphi(\boldsymbol{G}^{\text{sub}} = 0)$, namely E_0, Equ. 3.7 can be written as

$$E_{\text{ads}-\text{sub}}^{\text{domain}} = E_0 + \sum_{\{\boldsymbol{G}^{\text{sub}} \neq 0\}} \varphi(\boldsymbol{G}^{\text{sub}}) \mathrm{e}^{-i\boldsymbol{G}^{\text{sub}}\cdot\boldsymbol{\Delta}} \sum_{\{\boldsymbol{G}^{\text{ads}}\}} \delta(\boldsymbol{G}^{\text{sub}} - \boldsymbol{G}^{\text{ads}}). \tag{3.9}$$

Two important and related definitions can be derived from Equ. 3.9 and will be used

---

[b] using the definition $\delta(\boldsymbol{r}) = \delta(x)\delta(y)\delta(z)$ [74, p. 26]

throughout this work. If the adsorbate and substrate lattices don't exhibit *any coincidence* $\boldsymbol{G}^{\text{sub}} = \boldsymbol{G}^{\text{ads}}$ in reciprocal space (i.e., if the classification in Fig. 3.1 fails) the lock-in term in Equ. 3.9 vanishes for all $\boldsymbol{G}^{\text{sub}}$ and the adsorption energy is equal to E_0. Following previous definitions [64, 70], such structures will be called *incommensurate* hereafter and the associated adsorption energy $E^{\text{domain}}_{\text{ads-sub}} = E_0$, which is independent of $\boldsymbol{G}^{\text{sub}}$ and real space coordinates, will be called *incommensurate energy.* Note that contrary to a comment in Ref. [64], an overlayer structure may have a well-defined epitaxial, yet incommensurate relation to the underlying substrate (cf. Sec. 3.2). Further, the definition of incommensurate structures used here explicitly excludes POL and LOL ones and thereby follows other studies [13, 58] but deviates from works where POL/LOL structures were called incommensurate [75–77]. Others used the terms "uniaxially incommensurate" [78] and "one-dimensionally incommensurate" [79] for POL/LOL cases. However, these alternatives do not directly give credit to the matching of a set of lattice lines between overlayer and substrate which is the crucial mechanism behind the model of lattice epitaxy:

If a reciprocal adsorbate lattice vector $\boldsymbol{G}^{\text{ads}}$ and its multiples do coincide with a reciprocal substrate lattice vector $\boldsymbol{G}^{\text{sub}}$ and its multiples, i.e., if the corresponding sets of lattice lines match in real space, the respective terms in Equ. 3.9 contribute to $E^{\text{domain}}_{\text{ads-sub}}$, provided that the Fourier coefficients $\varphi(\boldsymbol{G}^{\text{sub}})$ of the interaction energy are different from zero. The contribution can be positive or negative, depending on the phase $\mathrm{e}^{-i\boldsymbol{G}^{\text{sub}}\cdot\boldsymbol{\Delta}}$ and thus on the shift of the entire overlayer with respect to the wave corresponding to $\boldsymbol{G}^{\text{sub}}$ [36]. However, assuming that the physical solution generally is the one where the overlayer exploits the chance to lower $E^{\text{domain}}_{\text{ads-sub}}$ below the incommensurate energy by shifting to an optimal $\boldsymbol{\Delta}$ [64], a single coincidence of reciprocal adsorbate and substrate lattice vectors (and multiples thereof) can already lead to an energy decrease with respect to the incommensurate energy.

This is the very nature of lattice epitaxy. The POL and LOL epitaxy types feature coincidences in only one reciprocal lattice direction, preventing a two-dimensionally periodic arrangement in real space. However, provided that the corresponding coefficients $\varphi(\boldsymbol{G}^{\text{sub}})$ are not zero, these coincidences lead to a decrease of $E^{\text{domain}}_{\text{ads-sub}}$ below the incommensurate energy even for infinitely large overlayers. This is why Equ. 3.9 is sometimes called the lock-in term [14, 70] – the entire domain is able to lock into registry in as many directions as there are coincidence directions in reciprocal space. Hence, it can be understood why an overlayer, with a structure that matches the substrate in at least one direction, prefers such an orientation over an arbitrary one. Such a minimum in adsorption energy will be called epitaxial energy minimum.

Additionally, the historically founded distinction between POL and LOL epitaxy types

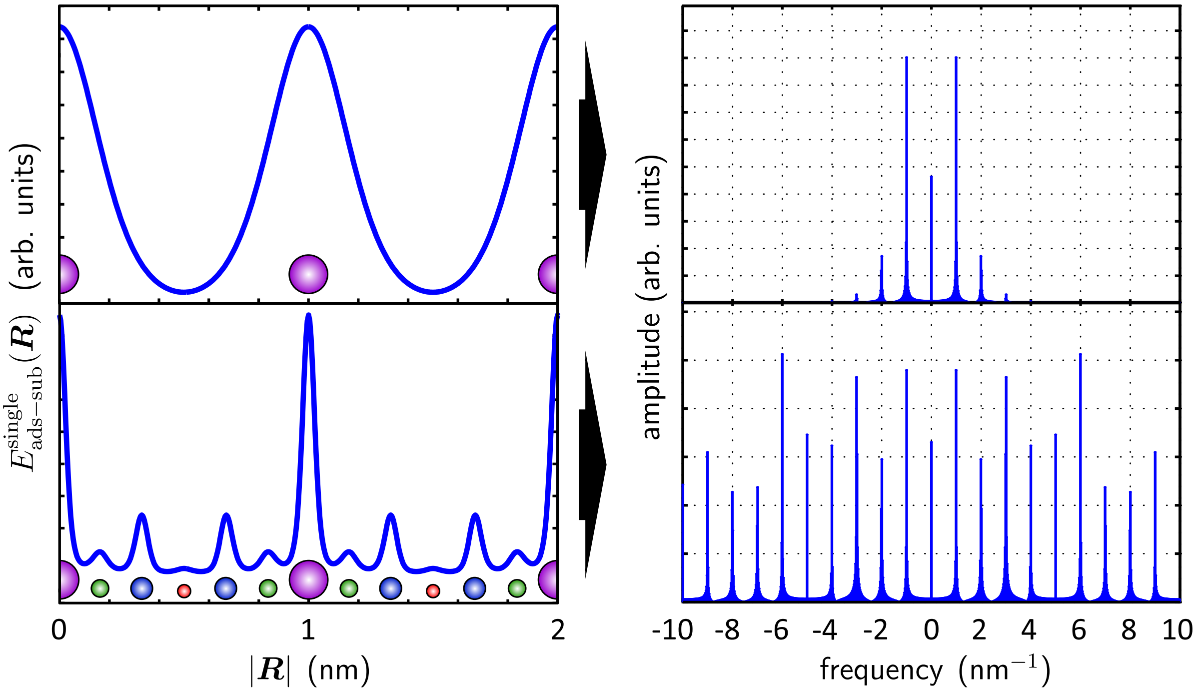

Figure 3.2: Comparison of the adsorption energies $E_{\mathrm{ads-sub}}^{\mathrm{single}}(\boldsymbol{R})$ of a hypothetical particle on two different "surfaces", shown left, and the corresponding frequency spectra, shown right. The nearly sinusoidal function of the top example is represented by very few frequencies. Conversely, the more complicated example below with more than one atom in the unit cell (e.g., the surface of an organic crystal) requires much higher frequencies in the Fourier representation.

obtains a physical meaning through the discussion of the Fourier coefficients $\varphi(\boldsymbol{G}^{\mathrm{sub}})$. Simple surfaces such as metal crystals provide nearly sinusoidal interaction potentials to adsorbates, leading to Fourier representations of the adsorbate-substrate interaction $E_{\mathrm{ads-sub}}^{\mathrm{single}}(\boldsymbol{R})$ that quickly converge to zero with higher orders in reciprocal space, as is schematically shown in Fig. 3.2. However, more complicated surfaces such as those of organic crystals require higher frequencies in the Fourier series [58, 64]. This gives rise to the possibility of higher-order coincidences with still significant values of $\varphi(\boldsymbol{G}^{\mathrm{sub}})$, which is the driving force of LOL epitaxy on organic crystals [58, 64].

On the other hand, it is convenient to emphasize again that an epitaxial alignment of an overlayer cannot be explained or expected within this lattice epitaxy model if there are no relevant coincidences with the substrate in reciprocal space. There are, however, concepts for explaining reproducible overlayer orientations by abandoning perfect and infinite lattices, as will be introduced next.

3.2 Epitaxy concepts beyond lattice epitaxy

If two structures are incommensurate, yet reproducibly align in a distinct way, other mechanisms than lattice epitaxy must be at play to provide epitaxial energy minima. First, the concept of orientational epitaxy will be introduced which abandons the exact translational symmetry of an overlayer lattice. The layer itself, however, is still assumed to be infinite. Finally, for the sake of completeness, finite-size effects are discussed. They can lead to multiple coexisting domains of similar or the same orientation but require the domains to be of a certain, finite size.

3.2.1 Orientational epitaxy

Novaco and McTague suggested already decades ago that an overlayer, which is incommensurate with the substrate lattice, can prefer a distinct orientation if the overlayer atoms locally optimize their lateral position with respect to the substrate [14, 72, 80, 81]. In an infinite, incommensurate overlayer with a *rigid* lattice all possible registries of adsorbate lattice points with the substrate occur, favorable as well as unfavorable ones. Hence, there is potential energy in the system that can be lowered by locally deviating from the unfavorable adsorbate lattice points. The authors approached this idea from a phonon perspective and analytically described the displacements from lattice sites as static phonons (at zero Kelvin), calling the resulting displacements static distortion waves (SDWs). The driving force is the potential energy in the adlayer-substrate interaction and the resulting straining of intralayer bonds acts as a counterbalance. Therefore, both interactions must be modeled in order to predict an epitaxial orientation.

The simplest way to describe an overlayer's response to the periodic potential of a substrate probably is its one-dimensional equivalent described in the Frenkel-Kontorova model [82], or in works of Frank and van der Merwe [83, 84]. The model assumes a chain of atoms, connected by identical springs with harmonic potentials, which is exposed to a sinusoidal potential $E^{\mathrm{single}}_{\mathrm{ads-sub}}$ with a different period, i.e., the substrate (cf. Fig. 3.3). Due to the periodic potential, each atom experiences an individual force $\frac{\partial}{\partial x_i} E^{\mathrm{single}}_{\mathrm{ads-sub}}$ and moves accordingly. The springs are therefore compressed or stretched and build up stress within the chain, i.e., adsorbate-adsorbate potential energy $E^{\mathrm{domain}}_{\mathrm{ads-ads}}$. The problem can be solved analytically to obtain the resulting displacements and the system's total (lowered) energy. The energy is lowered because the springs start from a relaxed state: already infinitesimal atomic displacements decrease $E^{\mathrm{domain}}_{\mathrm{ads-sub}}$ but do not yet increase $E^{\mathrm{domain}}_{\mathrm{ads-ads}}$, due to the vanishing slope at the bottom of the springs' harmonic potentials. Hence, the

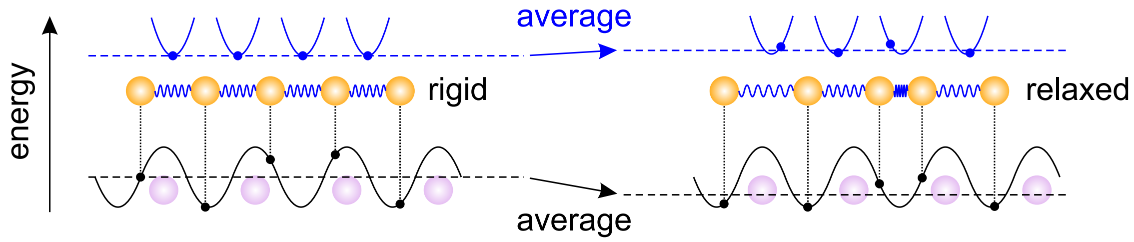

Figure 3.3: Schematic illustration of the Frenkel-Kontorova model. A chain of atoms connected by harmonic springs is subject to a sinusoidal potential, e.g., from an underlying substrate. Without relaxation (left), the respective lattice constants do not match. Small dots mark the individual atoms' contributions to the adsorbate-substrate potential (black), as well as the harmonic springs' contributions to the intralayer potential (blue). The relaxed chain (right) is locally distorted, building up intralayer stress in the springs, but lowering the mean total energy.

Novaco-McTague effect can be expected if the corrugation of $E_{\mathrm{ads-sub}}^{\mathrm{single}}$ is large enough against the springs to drive the relaxation, but not too large so that atoms are not forced into commensurate registry.

The Frenkel-Kontorova model describes a relaxation of lateral atomic coordinates, i.e., parallel to the surface. In the model of Novaco and McTague (NM), displacements perpendicular to the surface are generally included. However, perpendicular displacements do not determine the overlayer orientation [72, 85]. On the other hand, the Novaco-McTague theory (NM theory) has its own limits. Besides the harmonic springs, it assumes $E_{\mathrm{ads-sub}}^{\mathrm{single}}$ to be purely sinusoidal, with sufficiently small corrugation [86]. Additionally, it is limited to the so-called linear response regime [14] in which the modulation of the overlayer is sinusoidal as well. This breaks down, however, if the overlayer structure is close to a commensurate registry [87].

In the case discussed by NM, namely rare gases (Ar and Ne) adsorbed on graphite, the approximations and assumptions seem reasonable. The result are overlayers that are structurally modulated due to the interaction with the substrate. Strictly speaking, since Novaco and McTague discussed incommensurate lattices, this modulation leads to never-repeating patterns of displacements. The irrationality of the epitaxy matrix elements prevents a periodic registry of both adsorbate and substrate structures. This means such structures belong to one of the three possible deviations from crystals with translational symmetry: quasicrystals, incommensurate composite crystals, and incommensurately modulated crystals [88]. Nevertheless, they feature sharp diffraction patterns which will be discussed in more detail in the following chapter.

Since the amplitudes of SDW displacements are expected to be small compared to the separation of the overlayer atoms (or molecules) their influence has only been confirmed indirectly. For example, an experimental study on Ar adsorbed on graphite found overlayer orientations consistent with the Novaco-McTague theory (NM theory) [89]. In organic-inorganic heteroepitaxy, some regarded orientational epitaxy as unlikely to occur [36], while others applied the NM theory to optimal-orientation calculations concerning one fullerene monolayer on Pb(111), qualitatively agreeing with the experimental findings [90]. Of course, structural relaxation at the interface between two crystals by itself has been studied before [79, 91–93]. But in none of these reports lattice epitaxy is excluded as the simpler explanation for the overlayer orientations. In a study about rubrene molecules on Bi(001) the authors report a modulated molecular orientation as a result of "incommensurate" epitaxy and claim the NM mechanism to be responsible for the film growth [94]. However, due to the STM resolution the orientational modulation can be suspected at best, and the authors do not elaborate either on the possibility of POL or LOL epitaxy. Therefore, it can hardly be regarded as a confirmation of the NM theory. Further, Novaco and McTague state that the SDWs should lead to satellite peaks around the parent peaks in diffraction experiments [14, 72], but they expected them to be weak [72]. Experimental studies such as in Ref. [89] found such satellite peaks but attributed them fully to multiple scattering effects. Hence, there is no unequivocal prove to date of SDWs that explicitly and solely determine the orientation of an incommensurate overlayer.

3.2.2 Finite-size effects

The observation of epitaxy in the absence of "matching lattices" has been called "quasiepitaxy" in the past by Burrows et al. and Forrest et al. [69, 95, 96]. However, as has been derived in Sec. 3.1.3 within the model of perfect lattices, which was applied by Burrows and Forrest as well, such systems do not prefer any overlayer orientation. Rather, the small energy minima concluded from calculations in the cited works must be a consequence of the finite sizes of the calculated systems. Such a finite system leads to a lock-in term (Equ. 3.8) that can be different from zero even if no adsorbate reciprocal lattice vector $\boldsymbol{G}^{\text{ads}}$ exactly matches a substrate reciprocal lattice vector $\boldsymbol{G}^{\text{sub}}$. This is both reasonable, since only in the limit of infinite lattices the Kronecker Delta appeared in Equ. 3.9, and can be inferred from calculations directly considering the lock-in term [36] or a finite adsorbate domain [97].

Alternatively, an overlayer may tolerate a certain amount of strain to adapt its lattice over a finite region and become "locally commensurate" with the substrate [14]. The accumulating stress is then relieved in form of domain walls and/or incommensurate regions [93].

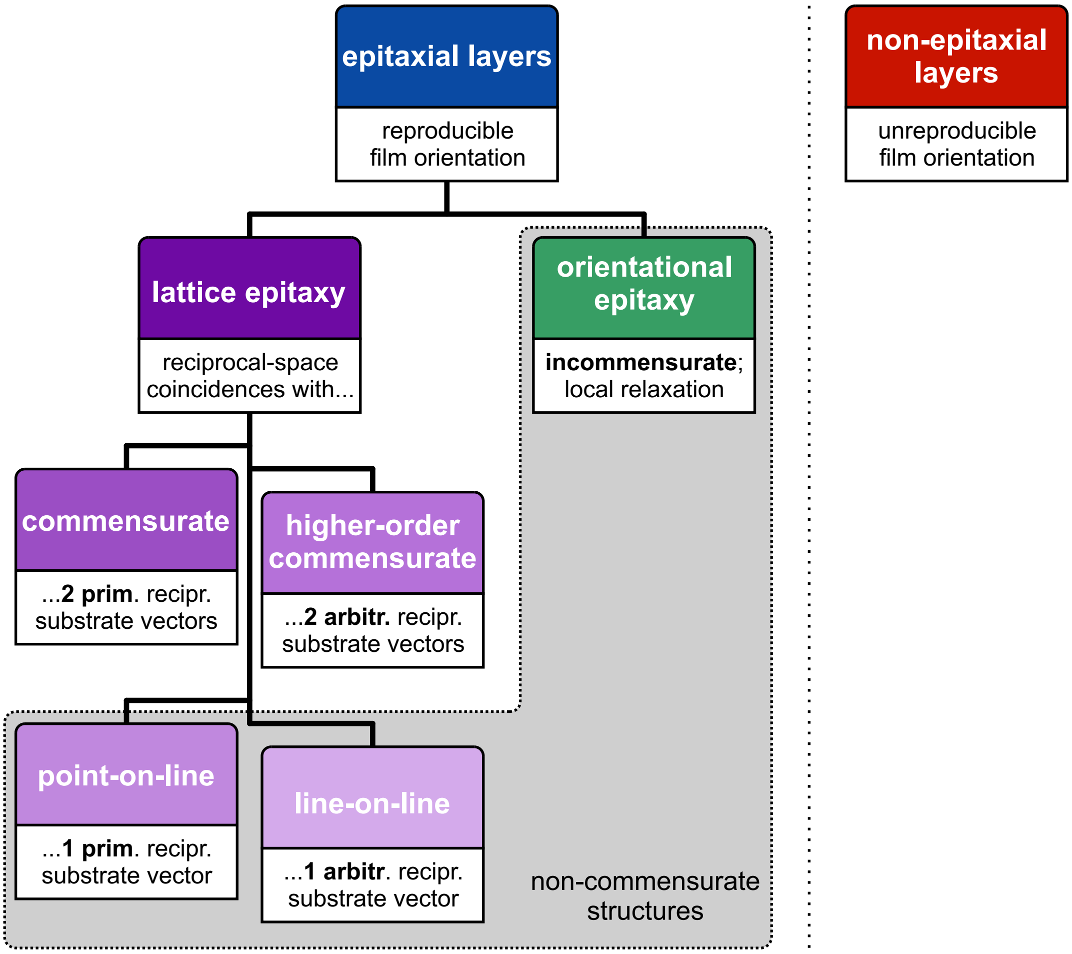

Figure 3.4: Schematic overview of the different concepts for explaining the epitaxy of very large (potentially infinite) domains. All types of lattice epitaxy rely on different degrees of coincidence of overlayer and substrate reciprocal lattices. Without such coincidences, orientational epitaxy abandons the strict translational symmetry of an (infinite) overlayer lattice to lower the adsorption energy through local relaxation.

Film growth on a crystalline substrate may be governed by finite-size effects such that domains of limited size (due to terrace sizes, growth dynamics,. . .) prefer a domain-size-dependent orientation with respect to the substrate [92, 97–100] and the final film morphology is then an agglomeration of many domains with that orientation. Even though this likely gives rise to a high concentration of domain boundaries such films may feature sharp diffraction patterns. An imaging technique in real space might therefore be necessary to confirm the growth mode of such a system.

3.2.3 Overview

Figure 3.4 summarizes the overview within this chapter about the various mechanisms which can provide an epitaxial energy minimum to a large and potentially infinite overlayer on a crystalline substrate, i.e., which lead to distinct orientations that are preferred by the overlayer. The concept of lattice epitaxy is likely the most commonly employed one due to its simplicity and because many systems are sufficiently explained with it. The mechanism behind epitaxial energy minima is a matching of sets of lattice lines between both the adsorbate and the substrate lattices. This becomes most obvious through coincidences of respective reciprocal lattice vectors.

If no such matches are present, yet the domains are still very large, the atoms/molecules of the overlayer must relax locally for an epitaxial energy minimum to be conceivable. This effect is therefore inherently different from lattice epitaxy. However, a combination of lattice epitaxy and local relaxation (or finite-size effects) may be at work within the same overlayer [79, 101]. Note that, while POL and LOL epitaxy types are not commensurate, they should not and will not be called incommensurate. This term is reserved for layers without reciprocal space coincidences, which, of course, are not commensurate as well (cf. gray box in Fig. 3.4).

This overview is thought to be generally complete for infinite domains – all known possibilities of epitaxial energy minima, especially concerning lattice epitaxy, are assumed to be included. Therefore, there is no need for additional terms of epitaxy types such as “coincidence I/II(a/b)” proposed by Hooks et al. [13] which, as defined in the paper, do not clearly distinguish between overlayers with 2D periodic registry (commensurate or HOC) and those without (POL, LOL).

In the next chapter, the consequences of the non-commensurate epitaxy types common in epitaxial organic films on diffraction experiments in general and low-energy electron diffraction (LEED) in particular will be discussed.

4 Modulated surfaces in reciprocal space

In the previous chapter, epitaxy types have been presented that may produce structural modulations within an epitaxial overlayer. A question arises quickly: How does a modulation of the overlayer structure by the substrate influence a diffraction pattern thereof? The question has been pursued in previous studies mostly in the context of structure determination for inorganic overlayers via complicated dynamic LEED simulations [102–104], fully taking into account effects such as multiple scattering in order to predict LEED intensities. For example, it has been found this way that a layer of graphene is incommensurate with an Ir(111) surface and exhibits a corrugation, i.e., a structural modulation perpendicular to the sample surface, due to the varying registry with the substrate [103]. A lateral modulation was considered but could not be confirmed.

However, the dynamic LEED theory of modulated surface structures has not received much attention [104] – possibly due to its complexity. The geometric analysis of LEED patterns from modulated surface structures [105] is more commonly used instead. It is known that an overlayer lattice on top of a substrate with a different lattice constant can generally cause Moiré patterns in imaging experiments such as STM. This can be due to merely electronic effects [106], or due to a real buckling of the overlayer [103]. Often, only a modulation perpendicular to the surface is found [102, 103, 107]. Both such modulations and multiple scattering, sometimes referred to as double diffraction/scattering, produce additional (satellite) spots in LEED patterns. Geometrically, the resulting patterns cannot be distinguished [108, 109]. Therefore, it is seldom clear which effect produces or dominates such satellites. Yet, they have been used to geometrically determine the expected period of Moiré patterns, or to compare it with the directly observed one [105]. Due to their apparent periodicity, Moiré patterns can lead to not independently verified conclusions of a commensurate (periodic) superstructure [110], or a confirmed incommensurate registry is intentionally approximated as HOC in order to efficiently perform dynamic LEED intensity calculations [102].

In the following, a structure factor shall be derived for modulated surface structures, with a focus on incommensurately modulated structures, that allows for a more intuitive insight into corresponding LEED patterns. Rather than describing the modulation in terms of its resulting period like elsewhere [78, 104], the substrate and (unmodulated) adsorbate unit cells will be used as a starting point for an approximation of LEED spot intensities. This renders the approach more flexible than the above-mentioned ones where the Moiré cell has to be redetermined every time the overlayer lattice or its orientation changes slightly. The origin of the concept lies in a general X-ray diffraction theory of incommensurately modulated 3D crystals by van Smaalen [73], which shall therefore be introduced via a simple example first. Moreover, in combination with software developed by Falko Sojka (Institute for Solid State Physics, FSU Jena, Germany) it is possible to exploit the geometric consequences of this approach in order to obtain the epitaxy matrix of an overlayer from LEED *and* STM images with drastically improved precision. This will be shown based on two exemplary systems: One with an organic epitaxial layer, namely PbPc on graphite, and an inorganic epitaxial layer, namely epitaxial graphene on SiC. Beyond the examples discussed here, the algorithm has already proved very useful in an additional publication [P7]. Consequences for other effects like disorder in modulated layers or systematic absences of diffraction orders will also be discussed.

4.1 Diffraction theory for modulated crystals

4.1.1 Unmodulated crystals

In order to establish quantities and definitions necessary for the following chapters, diffraction on periodic crystals in the kinematic limit shall be briefly covered first. In that context, diffraction by X-rays, electrons, or other suitable probes is often discussed in terms of the structure factor F, since it can be easily conceived, and the observed diffraction intensities are proportional to $|F|^2$ it in usually good approximation[c]. This factor is a direct consequence of the translation symmetry of a periodic crystal when it scatters a plane wave with wave vector $\boldsymbol{k}_0$ elastically. Depending on the outgoing wave $\boldsymbol{k}$ being considered, the change in the wave vector $\boldsymbol{S} = \boldsymbol{k}_0 - \boldsymbol{k}$, also referred to as momentum transfer, determines the phases of the waves interfering at the detector. The wave function

---

[c] Depending on the situation, effects of multiple scattering may have a strong influence on LEED spot intensities [108]. However, as will be explained in the following, the structure factor of modulated surfaces can be the dominant quantity.

at the detector, far away from the crystal,

$$\Psi(\boldsymbol{S}) \propto \int n(\boldsymbol{r}) \mathrm{e}^{i\boldsymbol{S}\cdot\boldsymbol{r}} d^3r \tag{4.1}$$

is obtained by integrating the corresponding phase factors, multiplied with the scattering density $n(\boldsymbol{r})$, over the crystal. Since a crystal with a periodic lattice is considered here, the scattering density $n(\boldsymbol{r}+\boldsymbol{R}) = n(\boldsymbol{r})$ repeats with the lattice vectors $\{\boldsymbol{R}\}$, where $\boldsymbol{R}$ is an integer linear combination of the primitive lattice vectors $\boldsymbol{a}_i$. Hence, it is sufficient to integrate over only one unit cell (UC) and add up the phase factors $\mathrm{e}^{i\boldsymbol{S}\cdot\boldsymbol{R}}$ of all unit cells:

$$\Psi(\boldsymbol{S}) \propto \int_{\mathrm{UC}} n(\boldsymbol{r}) \mathrm{e}^{i\boldsymbol{S}\cdot\boldsymbol{r}} d^3r \sum_{\{\boldsymbol{R}\}} \mathrm{e}^{i\boldsymbol{S}\cdot\boldsymbol{R}}. \tag{4.2}$$

Further, in the limit of an infinitely large lattice the phases $\mathrm{e}^{i\boldsymbol{S}\cdot\boldsymbol{R}}$ will average out and $\Psi(\boldsymbol{S})$ will vanish unless $\boldsymbol{S}$ equals a reciprocal lattice vector[d] $\boldsymbol{G}_{hkl} = h\boldsymbol{a}_1^* + k\boldsymbol{a}_2^* + l\boldsymbol{a}_3^*$, where the primitive reciprocal lattice vectors $\boldsymbol{a}_i^*$ satisfy the relation

$$\boldsymbol{a}_i^* \cdot \boldsymbol{a}_j = 2\pi\delta_{ij}. \tag{4.3}$$

In that case, every unit cell contributes the same phase leaving only the integral part of Equ. 4.2 to be analyzed. Therefore, only $\boldsymbol{S} = \boldsymbol{G}_{hkl}$ will be considered from here on. This is also referred to as Laue equation.

Sometimes the scattering density in one unit cell can be split into N different contributions $n_\mu(\boldsymbol{r})$ at the positions

$$\boldsymbol{r}_\mu = \xi_{\mu,1}\boldsymbol{a}_1 + \xi_{\mu,2}\boldsymbol{a}_2 + \xi_{\mu,3}\boldsymbol{a}_3 \tag{4.4}$$

with the relative coordinates $\boldsymbol{\xi}_\mu$. In case the individual contributions are atoms, this constitutes the well-known independent-atom approximation [112]. However, they may be defined to comprise whole molecules as well. In both cases the wave function turns into a sum over the contributing densities:

$$\Psi(\boldsymbol{G}_{hkl}) \propto \sum_{\mu=1}^{N} \left[\int_{\mathrm{atom}\ \mu} n_\mu(\boldsymbol{r}) \mathrm{e}^{i\boldsymbol{G}_{hkl}\cdot\boldsymbol{r}} d^3r \right] \mathrm{e}^{i\boldsymbol{G}_{hkl}\cdot\boldsymbol{r}_\mu}. \tag{4.5}$$

The remaining integral is usually called the scattering amplitude $f_\mu(\boldsymbol{G}_{hkl})$ or (atomic) form factor, as it contains the information about the scattering density of the μ^{th} contribution

---

[d] This represents an alternative version of the well-known Bragg law [111] $n\lambda = 2d_{hkl}\sin\theta'$ (with $2\theta' = \theta = \angle(\boldsymbol{k}_0, \boldsymbol{k})$), because $d_{hkl} = 2\pi/|G_{hkl}|$ and $|S|/2 = 2\pi\sin\theta'/\lambda$. Hence, $|S| = n|G_{hkl}|$.

$n_\mu(\boldsymbol{r})$ and thus depends on its "shape". The final result is the structure factor $F(\boldsymbol{G}_{hkl})$

$$\Psi(\boldsymbol{G}_{hkl}) \propto F(\boldsymbol{G}_{hkl}) = \sum_{\mu=1}^{N} f_\mu(\boldsymbol{G}_{hkl}) \mathrm{e}^{i\boldsymbol{G}_{hkl}\cdot\boldsymbol{r}_\mu}. \tag{4.6}$$

Even though it has been derived from a scattering point of view it can be interpreted as the Fourier coefficient $F(\boldsymbol{G})$ of a series expansion of the scattering density $n(\boldsymbol{r}) = \sum_{\boldsymbol{G}} F(\boldsymbol{G})\mathrm{e}^{-i\boldsymbol{G}\cdot\boldsymbol{r}}$, underlining its close connection with the periodicity of the crystal. Hence, in analogy to the illustrative discussion of Fourier coefficients in Fig. 3.2, more complicated atomic bases such as those of organic molecules lead to significant Fourier coefficients for relatively high orders (h, k, l).

Using Equs. 4.3 and 4.4, the phase of the structure factor only depends on the diffraction order (h, k, l) of interest and the relative atomic basis coordinates $\boldsymbol{\xi}_\mu$:

$$F(h, k, l, \boldsymbol{r}_\mu) = \sum_{\mu=1}^{N} f_\mu(\boldsymbol{G}_{hkl}) \mathrm{e}^{2\pi i(h\xi_{\mu,1}+k\xi_{\mu,2}+l\xi_{\mu,3})}. \tag{4.7}$$

In certain situations, a 3D translational symmetry of a crystal is not present or cannot be probed. For example, in LEED the inelastic mean free path of the diffracting electrons is so short that usually only one or few atomic layers contribute to the diffraction pattern [53]. Moreover, real 2D crystals exist, e.g., graphene or ordered monolayers of adsorbates on surfaces. In these cases, there is no periodicity perpendicular to the 2D plane, and the reciprocal space degenerates into so-called lattice rods along that direction [108]. As a result, the momentum transfer $\boldsymbol{S} = \boldsymbol{G}_{hk}^{\mathrm{ads}} + S_\perp \boldsymbol{e}_\perp$ can be described by integer multiples of reciprocal lattice vectors in only two dimensions and the component $S_\perp$ along the surface normal $\boldsymbol{e}_\perp$, changing the structure factor to

$$F(\boldsymbol{S}) = \sum_{\mu=1}^{N} f_\mu(\boldsymbol{S}) \mathrm{e}^{2\pi i(h\xi_{\mu,1}+k\xi_{\mu,2})+S_\perp r_{\mu,\perp}}. \tag{4.8}$$

Therein, the last phase containing the basis' third absolute (perpendicular) component can only be discarded if the 2D crystal's atomic basis is flat, i.e., all $r_{\mu,\perp}$ can be set to zero.

4.1.2 Incommensurately modulated 3D crystals

The above path towards a structure factor becomes more complicated if the crystal does not have a strict translational symmetry. As mentioned in Chapter 3 in the case of the Novaco-McTague orientational epitaxy, this is the case if the crystal structure is

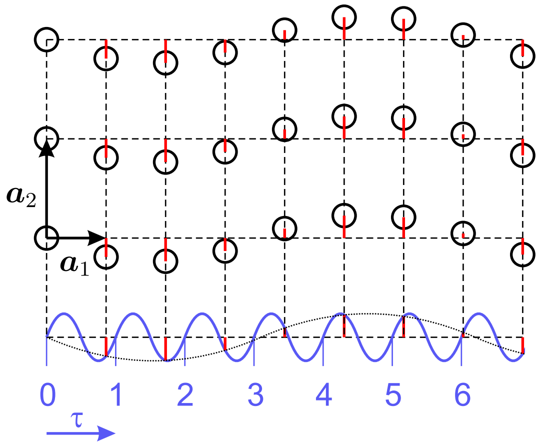

Figure 4.1: Two-dimensional projection of a crystal incommensurately modulated in one dimension, adapted from Ref. [73]. Unmodulated lattice sites are located at the crossing of dashed lines and circles represent the modulated atomic positions. Numbers count periods of the modulating function $\boldsymbol{u}(\tau)$ which are incommensurate with the lattice. Note that the period of displacements (thin dotted line) is different from the one of the modulating function.

modulated incommensurately. In his book about incommensurate crystallography [73] van Smaalen derives an X-ray structure factor for an arbitrary 3D crystal modulated by a one-dimensional periodic function with wave vector $\boldsymbol{q}$ of arbitrary orientation. In order to help understanding the more complex case of modulated surface structures and in order to synchronize van Smaalen's definitions with the ones used here, this simplest possible case will be introduced first.

While the incommensurate modulation can take the form of altered occupation probabilities for lattice sites, only displacements $\boldsymbol{u}$ of the atomic positions (termed "displacive modulation" in Ref. [73]) will be discussed here. Because of the assumed one-dimensionality of the modulation, the displacement at the location $\boldsymbol{r}$ only depends on the (projected) phase $\boldsymbol{q} \cdot \boldsymbol{r}$ with respect to the wave described by $\boldsymbol{q}$. Due to the definitions in this work, the modulating function $\boldsymbol{u}(\boldsymbol{q} \cdot \boldsymbol{r} + 2\pi) = \boldsymbol{u}(\boldsymbol{q} \cdot \boldsymbol{r})$ would be 2π-periodic, differing from Ref. [73] where the period is 1. This arises because the definition of the reciprocal lattice in Equ. 4.3 includes the factor of 2π while van Smaalen's equivalent definition does not. Therefore, a phase $\tau = \boldsymbol{q} \cdot \boldsymbol{r}/2\pi$ is introduced, divided by 2π as compared to Ref. [73], so that the periodicity of the displacements becomes

$$\boldsymbol{u}(\tau + 1) = \boldsymbol{u}(\tau) \tag{4.9}$$

and the following equations are directly comparable to Ref. [73] (see also Fig. 4.1). Note that the period of the final displacements depends on how the lattice constant of the unmodulated lattice scales in comparison to the modulating wave with wave vector $\boldsymbol{q}$ (cf. Fig. 4.1).

It is also important to note again that van Smaalen's structure factor is explicitly valid for incommensurate modulations, i.e., modulations where $\boldsymbol{q}$ is an irrational linear combination of the primitive lattice vectors such as in Fig. 4.1. This results in a crystal that, strictly speaking, is not translation-symmetric anymore. Nevertheless, for a sufficiently large lattice, sharp diffraction orders arise at positions $\boldsymbol{S} = \boldsymbol{G} + m\boldsymbol{q}$ that consist of a reciprocal lattice vector $\boldsymbol{G}$ of the crystal for the trivial case of a zero-amplitude modulation (unmodulated crystal) and an integer multiple of the modulation vector $\boldsymbol{q}$. Hence, geometrically a diffraction pattern corresponds to a reciprocal space convolution of the unmodulated crystal lattice and the 1D modulation lattice defined by $\boldsymbol{q}$. In that, it is geometrically equivalent to the optical diffraction on gratings resulting in the convolution of the gratings in the Fourier plane [113–115].

In the limit of infinitely large lattices and incommensurate modulations, van Smaalen's structure factor for a given $\boldsymbol{S} = \boldsymbol{G} + m\boldsymbol{q}$ can be written in the form

$$F(\boldsymbol{S}) = \sum_{\mu=1}^{N} f_\mu(\boldsymbol{S}) g_\mu(\boldsymbol{S}, m) \mathrm{e}^{i\boldsymbol{G}\cdot\boldsymbol{r}_\mu}. \tag{4.10}$$

Therein, $f_\mu(\boldsymbol{S})$ is similar to the form factor of the unmodulated crystal's atoms, with the only difference that it is evaluated at the new reciprocal vectors $\boldsymbol{S} = \boldsymbol{G} + m\boldsymbol{q}$ instead of merely $\boldsymbol{G}$. Note that the momentum transfer in the exponent, however, is not $\boldsymbol{S}$, but is reduced to a reciprocal lattice vector $\boldsymbol{G}$ of the unmodulated crystal. Therefore, Equ. 4.10 almost resembles an unmodulated crystal's structure factor from Equ. 4.6, except for the additional form factor

$$g_\mu(\boldsymbol{S}, m) = \int_0^1 \mathrm{e}^{i\boldsymbol{S}\cdot\boldsymbol{u}_\mu(\tau)} \mathrm{e}^{2\pi i m\tau} d\tau. \tag{4.11}$$

Its integration interval runs over one period of the modulating function $\boldsymbol{u}_\mu(\tau)$ for the μ^{th} atom in the unit cell, and g_μ is the only part of Equ. 4.10 that includes information about the shape of the modulation. Even though the modulated crystal is not strictly periodic the structure factor can be interpreted again as the coefficient of a regular 3D Fourier series expansion of the scattering density, with an additional dimension due to the 1D modulation: $n(\boldsymbol{r}) = \sum_{\boldsymbol{G}} \sum_m F(\boldsymbol{G} + m\boldsymbol{q}) \mathrm{e}^{-i(\boldsymbol{G}+m\boldsymbol{q})\cdot\boldsymbol{r}}$ (adapted from [73]). Therefore, even though the crystal does not have translational symmetry, it is regularly periodic in a (3+1)D superspace [73] and gives rise to sharp diffraction patterns.

4.1.3 Incommensurately modulated surface structures

Up to this point, the source of the modulation was not relevant and it was purely 1D. In the following, van Smaalen's general equations for 3D crystals shall be adapted to explicitly describe the case of a 2D crystalline overlayer modulated by a crystalline substrate. Thereafter, approximations will be made to show specific characteristics of the structure

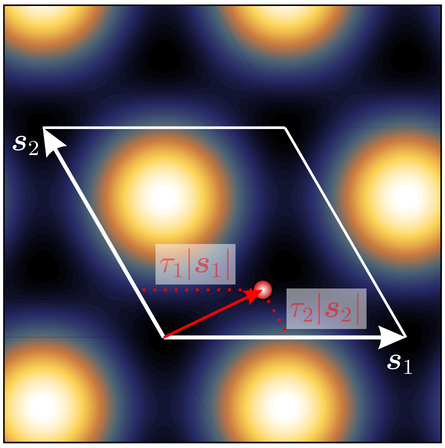

Figure 4.2: Exemplary illustration of the phases $\tau_{1/2}$ in Equ. 4.12. They correspond to a relative position within the substrate unit cell (marked in white on an exemplary map resembling the substrate surface).

factor that can be used to more easily understand and analyze LEED images of such systems.

Consider a 2D crystalline layer that is adsorbed incommensurately on the surface of a crystal, and its lattice is modulated due to the interaction with the substrate's surface structure. This could be a modulation of the adsorption height (z), the lateral position (x, y), or both, due to the varying adsorption sites of the overlayer atoms or molecules (particles). Hence, the substrate, more precisely the interaction energy $E_{\text{ads-sub}}^{\text{single}}$ as in Equ. 3.6, takes the role of the modulating function $\boldsymbol{u}(\boldsymbol{r})$. For simplicity, it is assumed in the following that the substrate is the dominant driving force of the displacements $\boldsymbol{u}(\boldsymbol{r})$. Intralayer interactions may influence the exact orientation and magnitude of the displacements. However, if the displacements are small enough that influence will be minor, and it will definitely not affect the periodicity of $\boldsymbol{u}(\boldsymbol{r})$. Therefore, if the substrate is assumed rigid, the function modulating the particles' positions must have the same periodicity as the substrate surface lattice (with primitive vectors $\boldsymbol{s}_1$ and $\boldsymbol{s}_2$). For example, the displacement $\boldsymbol{u}(\boldsymbol{r})$ of a particle at $\boldsymbol{r}$ would be the same as for a particle at $\boldsymbol{r} + \boldsymbol{s}_1$. Hence, in equivalence to Equ. 4.9, the displacements now depend periodically on the two independent phases $\tau_{1/2} = \boldsymbol{s}^*_{1/2} \cdot \boldsymbol{r}/2\pi$, with the corresponding reciprocal substrate vectors $\boldsymbol{s}^*_{1/2}$:

$$\boldsymbol{u}(\tau_1 + 1, \tau_2 + 1) = \boldsymbol{u}(\tau_1, \tau_2). \tag{4.12}$$

As depicted in Fig. 4.2, τ_1 and τ_2 can be read as relative coordinates with respect to the substrate unit cell vectors $\boldsymbol{s}_1$ and $\boldsymbol{s}_2$. Figuratively speaking, depending on its relative adsorption site (τ_1, τ_2) on the substrate unit cell, an adsorbate particle will be displaced due to the interaction with the substrate by $\boldsymbol{u}(\tau_1, \tau_2)$.

Equivalently to the above-discussed case of a 1D modulation, the geometric diffraction pattern will yield a convolution of the 2D reciprocal adsorbate lattice vectors $\boldsymbol{G}_{hk}^{\text{ads}}$ and the 2D reciprocal substrate lattice $\boldsymbol{G}^{\text{sub}}_{mn}$. Therefore, the possible reciprocal vectors are

$$\begin{aligned}\boldsymbol{S} =&\boldsymbol{G}^{\text{ads}}_{hk} + \boldsymbol{G}^{\text{sub}}_{mn} + S_\perp \boldsymbol{e}_\perp \\ =&h\boldsymbol{a}^*_1 + k\boldsymbol{a}^*_2 + m\boldsymbol{s}^*_1 + n\boldsymbol{s}^*_2 + S_\perp \boldsymbol{e}_\perp .\end{aligned} \tag{4.13}$$

and each diffraction order can be thought of as being a combination of a substrate and an (unmodulated) adsorbate reciprocal lattice point (cf. Fig. 4.3) – the diffraction orders could be indexed in (2+2) dimensions with four integer numbers (h, k, m, n). This includes both original lattices since either (h, k) or (m, n) can be $(0, 0)$. Hence, each reciprocal adsorbate lattice point obtains a number of satellite spots corresponding to the substrate reciprocal lattice. Alternatively, the adsorbate reciprocal lattice may be viewed as originating from the specular spot $(0, 0, 0, 0)$, but additionally also from all other substrate diffraction orders (m, n). This is illustrated in Fig. 4.3 where each lattice rod's position is a combination of both lattices. Depending on how the adsorbate lattice scales in comparison to the substrate lattice, this can lead to satellite-like patterns as well as complicated intermixture patterns. Note that this calculation only includes the overlayer atoms in a single-scattering process. Yet, even without the modulation, multiple scattering can produce the same geometric patterns [108, 109] (see Sec. 4.2.2 for details).

With that, Equ. 4.10 can be rewritten as follows:

$$F(\boldsymbol{S}) = \sum_{\mu=1}^{N} f_\mu(\boldsymbol{S}) g_\mu(\boldsymbol{S}, m, n) \mathrm{e}^{i(\boldsymbol{G}^{\text{ads}}_{hk} \cdot \boldsymbol{r}_\mu + S_\perp r_{\mu,\perp})} \tag{4.14}$$

with the factor

$$g_\mu(\boldsymbol{S}, m, n) = \int_0^1 \int_0^1 \mathrm{e}^{i\boldsymbol{S}\cdot\boldsymbol{u}_\mu(\tau_1,\tau_2)} \mathrm{e}^{2\pi i(m\tau_1+n\tau_2)} d\tau_1 d\tau_2 . \tag{4.15}$$

In accordance with the above 1D case, the integration runs over one period of each modulating wave, i.e., over one unit cell of the substrate surface lattice. Apart from this, the factor g_μ is not easy to grasp in its form in Equ. 4.15. The difficulty lies in the nature of the modulating function $\boldsymbol{u}(\tau_1, \tau_2)$ as an exponent. However, if the product $\boldsymbol{S} \cdot \boldsymbol{u}(\tau_1, \tau_2)$ is much smaller than 1, a Taylor series expansion $\mathrm{e}^x = 1 + x + \frac{1}{2!}x^2 + \dots$ can be performed up to the linear term in order to dispose of the exponential character:

$$\begin{aligned}g_\mu(\boldsymbol{S}, m, n) \approx &\int_0^1 \int_0^1 \mathrm{e}^{2\pi i(m\tau_1+n\tau_2)} d\tau_1 d\tau_2 \\ &+ \int_0^1 \int_0^1 i\boldsymbol{S} \cdot \boldsymbol{u}_\mu(\tau_1, \tau_2) \mathrm{e}^{2\pi i(m\tau_1+n\tau_2)} d\tau_1 d\tau_2 .\end{aligned} \tag{4.16}$$

Note that the condition $\boldsymbol{S} \cdot \boldsymbol{u}(\tau_1, \tau_2) \ll 1$ is fulfilled for sufficiently small displacement amplitudes or momentum transfers $\boldsymbol{S}$, or if their respective directions are close to perpen-

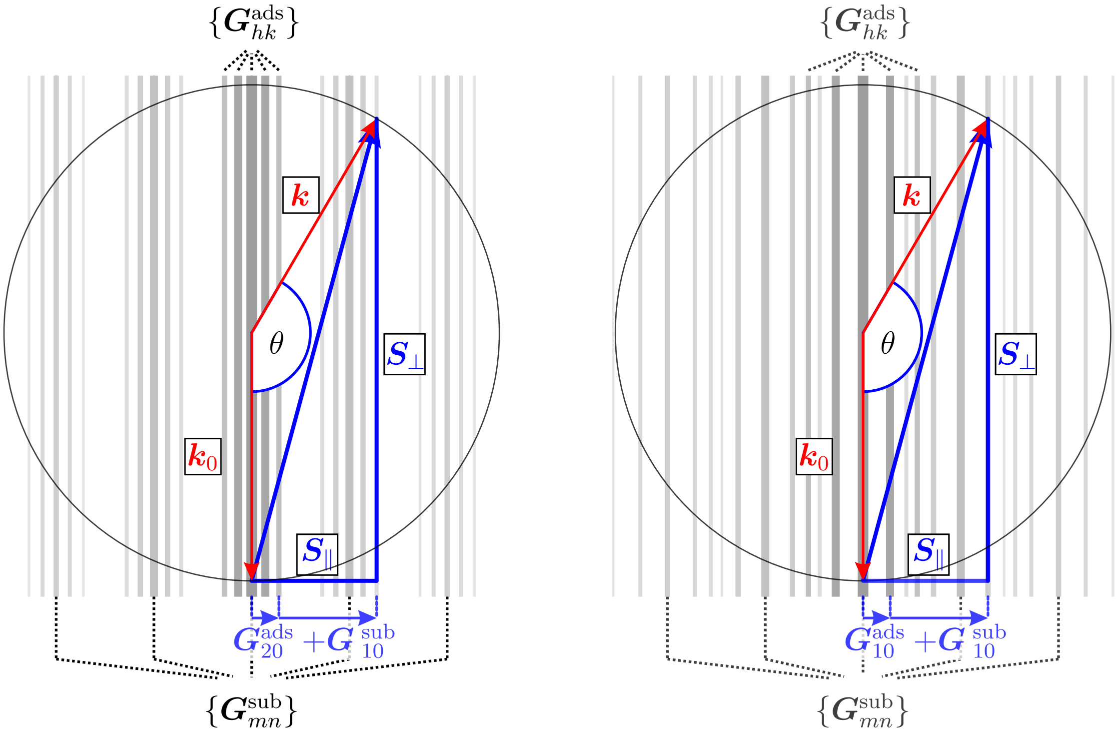

Figure 4.3: Schematic Ewald constructions in backscattering LEED geometry [108] for two different adsorbate lattices ($\{G^{\mathrm{ads}}_{mn}\}$ rods up to the second diffraction order) modulated by the same underlying substrate ($\{G^{\mathrm{sub}}_{mn}\}$ rods). The resulting pattern is a convolution of both lattices. The adsorbate lattice constant in the right panel is half the one in the left panel, producing a much more complex intermixed LEED pattern. The thickness and faded colors of the rods illustrate tendencies of intensities (see text) and increase the visual differentiability.

dicular. In a backward-scattering setup like LEED $S_\perp$ is relatively close to the maximum value of $2k_0$ (cf. Fig. 4.3)[e]. Therefore, LEED is very sensitive to modulations perpendicular to the surface. However, in a typical beam energy range of 10. . . 100 eV the approximation requirement for the perpendicular modulation seems to become prohibitively small: $u_\perp \ll 0.01 \ldots 0.1$ Å. Yet, the main conclusions from this chapter still hold, as will be shown in Section 4.2.2. Lateral displacements fulfill the condition more easily. $S_\parallel$ vanishes in the vicinity of the specular spot. Hence, spots due to lateral modulations are better observable the further they are away from it. The minimal diffraction angle θ (cf. Fig. 4.3) needed for a spot to be observable with the Omicron MCP LEED device used here is 150°. Therefore, the maximum value for $S_\parallel$ is $\frac{1}{2}k$, and a realistic $u_\parallel \ll 0.4 \ldots 1.2$ Å is required for the approximation in the mentioned energy range.

In its approximated form Equ. 4.16 can be understood more intuitively. The first term is zero for any combination of the “substrate indexes” m and n except for $(m, n) = (0, 0)$, i.e., for the original (unmodulated) adlayer diffraction orders $\{G^{\mathrm{ads}}_{hk}\}$ originating from the

---

[e] For clarity, absolute values of vectors such as $\boldsymbol{S}$, $\boldsymbol{k}$, $\boldsymbol{G}$, etc. are written as S, k, and G in this chapter.

specular spot, in which case the first term equals 1. For the more interesting new diffraction orders due to the modulation it can thus be dropped. Taylor terms of higher than the linear order are negligible within the approximation, but always lead to $|g_\mu| < 1$ for non-vanishing modulations [73]. Hence, intensity of the spots from the unmodulated adsorbate lattice is transferred to the satellites arising from the modulation, and a satellite spot is generally weaker than the one it originates from, unless $f_\mu(\boldsymbol{S})$ completely compensates this tendency. This is illustrated by the line thicknesses and faded gray shades in Fig. 4.3.

Modulation of the adsorption height

Assuming for simplicity a pure height modulation $\boldsymbol{u}(\tau_1, \tau_2) = u_\perp(\tau_1, \tau_2)\boldsymbol{e}_\perp$ first, the integral becomes

$$g_\mu(\boldsymbol{S}, m, n) \approx iS_\perp \int_0^1 \int_0^1 u_{\mu,\perp}(\tau_1, \tau_2) \mathrm{e}^{2\pi i(m\tau_1 + n\tau_2)} d\tau_1 d\tau_2. \tag{4.17}$$

Alternatively, it can be written in terms of its dependence on $\boldsymbol{G}_{mn}^{\mathrm{sub}}$ as an integral over a substrate unit cell (subUC):

$$g_\mu(\boldsymbol{S}, m, n) \approx iS_\perp \iint\limits_{\mathrm{subUC}} u_{\mu,\perp}(\boldsymbol{r}) \mathrm{e}^{i\boldsymbol{G}_{mn}^{\mathrm{sub}} \cdot \boldsymbol{r}} d^2 r. \tag{4.18}$$

Importantly, the integral can be recognized as the Fourier coefficient $h_{\mu,\perp}(\boldsymbol{G}_{mn}^{\mathrm{sub}})$ of a 2D Fourier series expansion of $u_{\mu,\perp}(\boldsymbol{r})$ in terms of reciprocal substrate lattice vectors $\boldsymbol{G}_{mn}^{\mathrm{sub}}$:

$$u_{\mu,\perp}(\boldsymbol{r}) = \sum_{\{\boldsymbol{G}_{mn}^{\mathrm{sub}}\}} h_{\mu,\perp}(\boldsymbol{G}_{mn}^{\mathrm{sub}}) \mathrm{e}^{-i\boldsymbol{G}_{mn}^{\mathrm{sub}} \cdot \boldsymbol{r}} \tag{4.19}$$

Since the interaction between an adsorbate particle and the substrate (via $E_{\mathrm{ads-sub}}^{\mathrm{single}}$) is assumed to dominate the displacements as mentioned above, the modulation function $u_{\mu,\perp}(\boldsymbol{r})$ reflects symmetry of the substrate, more precisely that of $E_{\mathrm{ads-sub}}^{\mathrm{single}}$. In the case of atomic adsorbates and some molecules, the substrate's atomic basis will be directly reproduced in a map of $E_{\mathrm{ads-sub}}^{\mathrm{single}}(\boldsymbol{r})$. Hence, the factor g_μ is comparable to the structure factor of the substrate. The independent atom approximation allows for including the atomic basis (M atoms in substrate unit cell at positions $\boldsymbol{r}_\nu$) into g_μ and thus all the substrate symmetries that come with it:

$$g_\mu(\boldsymbol{S}, m, n) \approx iS_\perp \sum_{\nu=1}^{M} h_{\mu\nu,\perp}(\boldsymbol{G}_{mn}^{\mathrm{sub}}) \mathrm{e}^{i\boldsymbol{G}_{mn}^{\mathrm{sub}} \cdot \boldsymbol{r}_\nu}. \tag{4.20}$$

Therein, the coefficients $h_{\mu\nu,\perp}(\boldsymbol{G}_{mn}^{\mathrm{sub}}) = \iint_{\mathrm{atom}\ \nu} u_{\mu\nu,\perp}(\boldsymbol{r}) \mathrm{e}^{i\boldsymbol{G}_{mn}^{\mathrm{sub}} \cdot \boldsymbol{r}} d^2 r$ are the form factors that contain the information about how the μ^{th} adsorbate atom is displaced by the ν^{th} substrate atom, i.e., they are not determined by scattering processes but by characteristics of the modulation.

In the case of a general molecular adsorbate, the $E^{\text{single}}_{\text{ads-sub}}(\boldsymbol{r})$ map can be more complex because it contains the information of the extended molecular structure as well [64]. However, the periodicity of the substrate is retained as in the case of an atomic adsorbate, and a more complex shape of $E^{\text{single}}_{\text{ads-sub}}(\boldsymbol{r})$ can in principal be described with an adapted form factor in equivalence to Equ. 4.20.

Therefore, the structure factor of a 2D overlayer lattice with an incommensurately modulated adsorption height due to the underlying substrate can be regarded as the combination of two rather simple structure factors, one from the unmodulated overlayer (first one) and one from the substrate (via $E^{\text{single}}_{\text{ads-sub}}$) (second one):

$$F(\boldsymbol{S}) \approx iS_\perp \sum_{\mu=1}^{N} \left[f_\mu(\boldsymbol{S}) \mathrm{e}^{i(\boldsymbol{G}^{\text{ads}}_{hk}\cdot \boldsymbol{r}_\mu + S_\perp r_{\mu,\perp})} \sum_{\nu=1}^{M} h_{\mu\nu,\perp}(\boldsymbol{G}^{\text{sub}}_{mn}) \mathrm{e}^{i\boldsymbol{G}^{\text{sub}}_{mn}\cdot \boldsymbol{r}_\nu} \right] . \tag{4.21}$$

Note that the only components in Equ. 4.21 that depend on the incident beam energy are $S_\perp = k(1 - \cos\theta)$, and $f_\mu(\boldsymbol{S})$, with the former being a smooth function of the diffraction angle θ. Especially in the case of a flat adsorbate basis[f] (atoms or flat molecules), this means that the total structure factor and thus the diffracted intensities are dominated by characteristics of the modulating function and the atomic bases of the adsorbate and the substrate, all of which are energy-independent. Since $S_\perp$ decreases towards the LEED screen edge, intensities of satellite spots due to a perpendicular modulation can be expected to be tendentially weaker there. With $\theta > 150^\circ$ in the case of the MCP LEED devices, however, the effect is rather small: $\left(\frac{S_\perp(\theta=150^\circ)}{S_\perp(\theta=180^\circ)}\right)^2 \approx 0.87$.

Hence, within the above assumptions and approximations only a weak energy dependence of the diffraction pattern as a whole is expected from such structures – one could think of the diffraction pattern as being imprinted by the modulation. Evidence for the validity of this conclusion and a general description of the behavior of Equ. 4.21 will be given in Sec. 4.2.2.

Modulation of the lateral positions

Similar conclusions can be drawn for a lateral modulation of the overlayer due to the substrate. In the previous case of a modulated adsorption height, no explicit assumptions had to be made concerning the exact shape of the displacement function $u_\perp(\tau_1, \tau_2)$ because of its scalar character in only one dimension. It did not matter for the discussion whether atoms moved up or down at a given site (τ_1, τ_2), only whether the displacement was periodic with the substrate lattice, i.e., could be developed as a Fourier series of reciprocal substrate

---

[f] With all $r_{\mu,\perp} = 0$, the value of $S_\perp$ is not relevant in the exponents of Equ. 4.21.

lattice vectors. In order to keep the results for more complex lateral displacements as simple as possible again, two rather natural assumptions are made, which will also be corroborated in Chapt. 5:

i) The perpendicular displacement is proportional to (the corrugation of) the adsorbate-substrate potential energy: $u_\perp(\boldsymbol{r}) = c_\perp \left(E_{\text{ads}-\text{sub}}^{\text{single}} - E_0\right)$. It follows immediately that the coefficients of the Fourier expansion of $u_\perp(\boldsymbol{r})$ in Equ. 4.19 are identical to those of $E_{\text{ads}-\text{sub}}^{\text{single}}$, except for an offset and scaling $c_\perp$.

ii) The lateral displacement $\boldsymbol{u}_\parallel(\boldsymbol{r})$ is proportional to the gradient $\boldsymbol{u}_\parallel(\boldsymbol{r}) = c_\parallel \nabla E_{\text{ads}-\text{sub}}^{\text{single}}(\boldsymbol{r})$.

This can be pictured by the Frenkel-Kontorova model in Fig. 3.3 again. While the atoms move sideways due to the driving force $\nabla E_{\text{ads}-\text{sub}}^{\text{single}}(\boldsymbol{r})$ to adopt more advantageous adsorption sites, they can adjust their adsorption height accordingly.

If $E_{\text{ads}-\text{sub}}^{\text{single}}(\boldsymbol{r})$ is expanded again into a Fourier series of reciprocal substrate lattice vectors

$$\begin{aligned} E_{\text{ads}-\text{sub}}^{\text{single}}(\boldsymbol{r}) &= \sum_{m,n} \varphi(\boldsymbol{G}_{mn}^{\text{sub}}) \mathrm{e}^{-i\boldsymbol{G}_{mn}^{\text{sub}}\cdot\boldsymbol{r}} \\ &= \sum_{m,n} \varphi(\boldsymbol{G}_{mn}^{\text{sub}}) \mathrm{e}^{-2\pi i(m\tau_1+n\tau_2)} \\ &\sim u_\perp(\tau_1,\tau_2), \end{aligned} \tag{4.22}$$

the partial derivatives with respect to the substrate lattice vectors provide the displacements in the respective directions of $\boldsymbol{s}_1$

$$u_{\parallel,1}(\tau_1) = c_\parallel \frac{\partial}{\partial\tau_1} E_{\text{ads}-\text{sub}}^{\text{single}}(\tau_1,\tau_2) = -2\pi i \sum_{m,n} m\varphi(\boldsymbol{G}_{mn}^{\text{sub}}) \mathrm{e}^{-i\boldsymbol{G}_{mn}^{\text{sub}}\cdot\boldsymbol{r}} \tag{4.23}$$

and $\boldsymbol{s}_2$

$$u_{\parallel,2}(\tau_2) = c_\parallel \frac{\partial}{\partial\tau_2} E_{\text{ads}-\text{sub}}^{\text{single}}(\tau_1,\tau_2) = -2\pi i \sum_{m,n} n\varphi(\boldsymbol{G}_{mn}^{\text{sub}}) \mathrm{e}^{-i\boldsymbol{G}_{mn}^{\text{sub}}\cdot\boldsymbol{r}}. \tag{4.24}$$

Hence, the Fourier coefficients of $u_{\parallel,1/2}(\tau_1,\tau_2)$

$$\begin{aligned} \varphi_1' &= -2\pi i m c_\parallel \varphi(\boldsymbol{G}_{mn}^{\text{sub}}) \\ \varphi_2' &= -2\pi i n c_\parallel \varphi(\boldsymbol{G}_{mn}^{\text{sub}}) \end{aligned} \tag{4.25}$$

are merely modified versions of those of the height modulation $u_\perp$ (cf. Equ. 4.22). Therefore, with the above assumptions connecting the modulation to the adsorbate-substrate potential energy, the Fourier coefficients of all components of the modulating function $\boldsymbol{u}(\boldsymbol{r})$ are proportional to the Fourier coefficients $\varphi(\boldsymbol{G}_{mn}^{\text{sub}})$.

Now, the modulation form factor g_μ of Equ. 4.16 can be stated in a rather simple form for the case including a lateral modulation. If $\boldsymbol{S}_\parallel$ is split into its projections $S_{\parallel,1/2}$ along the substrate vectors $\boldsymbol{s}_{1/2}$ as well, the scalar product $\boldsymbol{S}\cdot\boldsymbol{u}_\mu$ becomes $S_{\parallel,1}u_{\mu,\parallel,1}+S_{\parallel,2}u_{\mu,\parallel,2}+S_\perp\cdot u_{\mu,\perp}$, and Equ. 4.16 can be written as follows for diffraction orders (h,k,m,n) with $(m,n)\neq(0,0)$:

$$\begin{aligned} g_\mu(\boldsymbol{S},m,n) &\approx \int_0^1\int_0^1 i\boldsymbol{S}\cdot\boldsymbol{u}_\mu(\tau_1,\tau_2)\mathrm{e}^{2\pi i(m\tau_1+n\tau_2)}d\tau_1 d\tau_2 \\ &= i\varphi(\boldsymbol{G}^{\mathrm{sub}}_{mn})\left[-2\pi i c_\parallel\left(mS_{\parallel,1}+nS_{\parallel,2}\right)+c_\perp S_\perp\right]. \end{aligned} \tag{4.26}$$

Obviously, the modulation factor $g_\mu(\boldsymbol{S})$ remains proportional to the Fourier coefficients $\varphi(\boldsymbol{G}^{\mathrm{sub}}_{mn})$ of $E^{\mathrm{single}}_{\mathrm{ads-sub}}$ even if a lateral modulation is included in the above form. Further, none of the factors or terms in Equ. 4.26, except for the last one, depend on the incident beam energy since both $\boldsymbol{G}^{\mathrm{sub}}_{mn}$ and $\boldsymbol{S}_\parallel$ are fixed by the diffraction order (h,k,m,n) for which the structure factor is to be determined – and the last term only adds the weak dependence discussed above. The weak energy dependence of the LEED intensities concluded above for the case of a height modulation is retained in the general case. Note again, however, that spots in the vicinity of the specular spot lead to vanishing values of $S_{\parallel,1/2}$. Hence, spots dominantly due to a lateral modulation will hardly be observable there. As noted above, however, the opposite is the case for a modulation perpendicular to the surface.

4.1.4 Debye-Waller factor - Disorder in modulated 2D crystals

Up to this point all real-space atomic positions have been assumed fixed, i.e., temperature and other dynamical effects were not included. However, especially the former can be important in order to understand the appearance of a LEED pattern, of modulated as well as unmodulated structures. A standard approach to account for the increased movement of particles at temperatures above 0 K is the Debye-Waller factor. In the most general case it is introduced by calculating the structure factor for atomic positions $\boldsymbol{r}_\mu+\boldsymbol{\delta}_\mu(t)$ and averaging over time, since these movements will be fast compared to the observation time. In the limit of small and isotropic mean displacements $\langle\delta(t)\rangle$, this results in a structure factor $F_0(\boldsymbol{S})$ that is reduced by the Debye-Waller factor [116]

$$\langle F(\boldsymbol{S},t)\rangle = F_0(\boldsymbol{S})\exp\left(-\frac{1}{2}S^2\left\langle\delta^2(t)\right\rangle\right). \tag{4.27}$$

The usual conclusion is that such a thermodynamically induced disorder reduces the intensity of the Bragg reflections with increasing temperature due to the increasing displacements. *Static* disorder induced by statistical defects in the crystal has the same effect, with the averaging being performed over space instead of time, due to the space-averaging character of diffraction techniques probing macroscopic sample areas or volumes [P5].

Note that with isotropic displacements $\boldsymbol{\delta}$, the Debye-Waller factor decreases with S, becoming the smallest for a scattering angle of $\theta = 180°$ where $S = 2k_0$, i.e., for the reflection closest to the center in a LEED measurement. On the surface of crystals, however, the disorder parallel to the surface $\left\langle \delta_\parallel \right\rangle$ might be of different magnitude than the one perpendicular to the surface $\langle \delta_\perp \rangle$. Hence, a distinction of these contributions, adapting an approach from the literature [117], leads to independent Debye-Waller factors for lateral and perpendicular disorder, respectively[g]

$$\langle F(\boldsymbol{S},t)\rangle = F_0(\boldsymbol{S}) \exp\left(-\frac{1}{4} S_\parallel^2 \left\langle \delta_\parallel^2 \right\rangle\right) \exp\left(-\frac{1}{2} S_\perp^2 \left\langle \delta_\perp^2 \right\rangle\right) . \tag{4.28}$$

If the squared lateral disorder $\left\langle \delta_\parallel^2 \right\rangle$ is more than twice as large as the perpendicular one $\langle \delta_\perp^2 \rangle$, the lateral factor dominates and higher-order reflections (higher $S_\parallel$) are weakened more than the ones around the specular spot. This situation can easily occur on crystal surfaces. On unmodulated surfaces this is part of the reason why higher-order reflections are often weaker than low-order ones. Another reason is the atomic form factor which will be discussed in Sec. 4.2.2.

For modulated crystals, the Debye-Waller factor has already been calculated [118–121], with varying conclusions on the qualitative and quantitative consequences for the intensities. However, all of those approaches start with modulated phases or amplitudes of the modulating function in Equ. 4.12 themselves, treating the displacements in a correlated (phonon-like) fashion. The resulting Debye-Waller factors are quite complicated and will not be discussed here.

However, simply introducing a random anisotropic disorder $\boldsymbol{\delta}$ as above into the real space coordinate in the structure factor of a modulated overlayer (cf. Equ. 4.14) should be valid in first approximation. Assuming that the average displacements of the different particles in the lattice basis are similar $\langle \delta_\mu \rangle = \langle \delta \rangle$, this results again in the structure factor F_0 from Equ. 4.14, reduced by two Debye-Waller factors:

$$\begin{aligned} \langle F \rangle &= \sum_{\mu=1}^{N} f_\mu(\boldsymbol{S}) g_\mu(\boldsymbol{S}, m, n) \left\langle \exp\left(i(\boldsymbol{G}_{hk}^{\text{ads}} \cdot (\boldsymbol{r}_\mu + \boldsymbol{\delta}_{\mu,\parallel}) + S_\perp (r_{\mu,\perp} + \delta_{\mu,\perp}))\right)\right\rangle \\ &= F_0 \exp\left(-\frac{1}{4} \left(G_{hk}^{\text{ads}}\right)^2 \left\langle \delta_\parallel^2 \right\rangle\right) \exp\left(-\frac{1}{2} S_\perp^2 \left\langle \delta_\perp^2 \right\rangle\right) . \end{aligned} \tag{4.29}$$

The second Debye-Waller factor is identical to the one in Equ. 4.28. The first one, however,

---

[g] For a derivation of Equ. 4.28 see Appendix A.I.

only depends on the length of the reciprocal adsorbate lattice vector $\boldsymbol{G}_{hk}^{\mathrm{ads}}$ that contributes to the vector $\boldsymbol{S}_{hkmn} = \boldsymbol{G}_{hk}^{\mathrm{ads}} + \boldsymbol{G}_{mn}^{\mathrm{sub}} + \boldsymbol{S}_{\perp}$.

Hence, in the picture of the convoluted adsorbate and substrate lattices, every set of reciprocal adsorbate lattice points originating from any reciprocal substrate lattice point is tendentially decreased in intensity for increasing distances from the corresponding substrate lattice point, independent of the total parallel momentum transfer $S_{\|}$. This, in addition to the arguments given in Sec. 4.1.3, is why each set of $\boldsymbol{G}_{hk}^{\mathrm{ads}}$ lattice rods in Fig. 4.3 is depicted as decreasing in intensity with increasing orders (h, k).

Of course, this tendency can be offset to some degree by the shape of the adsorbate's atomic basis and form factors. Moreover, Equ. 4.29 only describes lateral disorder $\left\langle \delta_{\|} \right\rangle$ (static or dynamic) in the overlayer. A possible correlation with atomic movements in the substrate is neglected thereby. The Debye-Waller factor for the unmodulated substrate can be obtained separately from Equ. 4.28.

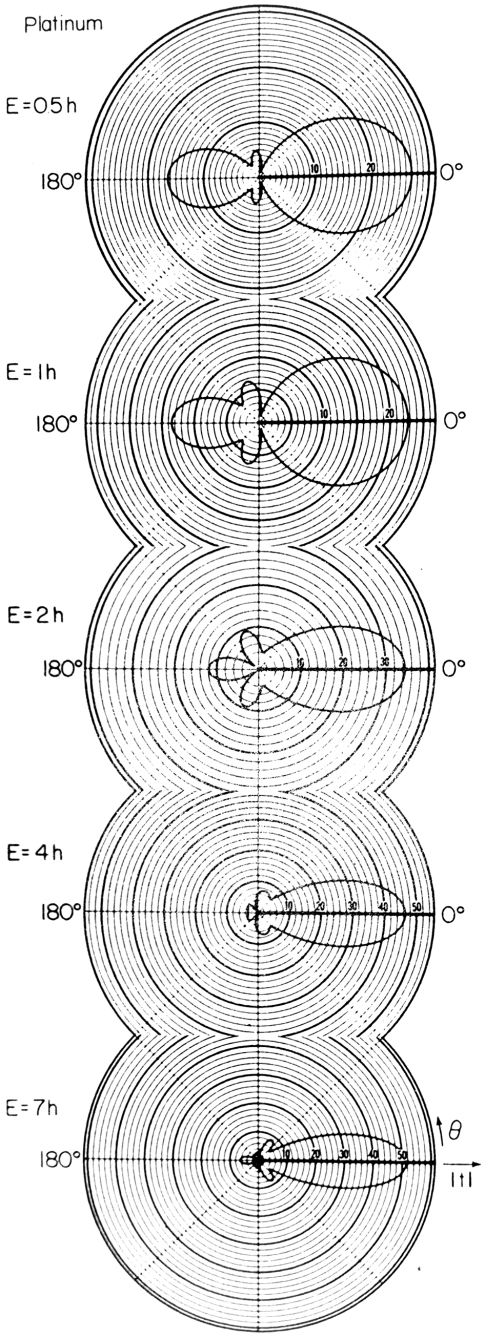

Figure 4.4: Calculated scattering cross sections $|f(\theta)|^2$ for platinum in dependence of the incident electron energy E, given in Hartree $h \approx 27.2$ eV [108, p. 130].

4.1.5 The role of the form factors

For a given structure, the atomic form factors $f_{\mu}(\boldsymbol{S})$ are the big unknowns in the calculation of structure factors and hence the intensities of LEED spots. In the case of low scattering potentials or high-energy electrons (not valid in LEED) the so-called Born approximation (perturbative ansatz) can be applied and exchange correlation effects between the scattered electrons and the atomic electron shells can be neglected. This results in a scattering amplitude (form factor) proportional to the Fourier transform the atom's electron density [122]. As apparent from Fig. 4.4 this leads to dominant forward scattering (small momentum transfers) and decreasing form factors for increasing scattering angles, with the lowest values for backward scattering – a dependency disagreeing with general LEED patterns where the (0,0) reflection is usually the strongest one.

For low-energy electrons in the range < 100 eV, however, the Born approximation is not valid. In that case, more sophisticated approaches need to be deployed that take into account the interaction with the atomic electron shells in the sample. Experiments with rare gases and small molecules like CO [123–126] and theoretical models [108, 127, 128] show that in this energy range the ratio of backscattered electrons increases again to values comparable with forward-scattered electrons. Additionally, the shape in the backward-scattering regime often qualitatively resembles the one for forward-scattered electrons (cf. Fig. 4.4). Therefore, a scattering amplitude f_μ tendentially decreasing towards the LEED screen edge can be expected. As such, it adds to the same trend that has already been concluded from Equ. 4.21 for spots arising from a perpendicular modulation, due to the factor $S_\perp$. In the case of lateral modulations, it counterbalances the decreasing intensity towards the screen center to some degree. Yet, a vanishing value of $S_\parallel$ erases any spots solely due to lateral modulations, for any shape of f_μ. Therefore, the atomic form factors are not expected to strongly affect the other conclusions in this chapter.

The other form factors $h_{\mu\nu,\perp}(\boldsymbol{G}_{mn}^{\mathrm{sub}})$ in Equ. 4.20 for perpendicular modulations or $\varphi(\boldsymbol{G}_{mn}^{\mathrm{sub}})$ in Equ. 4.26 for general modulations describe how the displacements depend on the (unmodulated) adsorption sites. It is reasonable to assume that a natural modulation of an adsorbate's lattice due to an underlying substrate is a smooth function of space. Hence, it will always be possible to expand the modulating function $\boldsymbol{u}(\tau_1, \tau_2)$ into a Fourier series with a finite number of coefficients $h_{\mu\nu,\perp}(\boldsymbol{G}_{mn}^{\mathrm{sub}})$ or $\varphi(\boldsymbol{G}_{mn}^{\mathrm{sub}})$, becoming less relevant with higher orders of (m, n). Hence, higher indexes (m, n) of the reciprocal substrate lattice vector contributing to $\boldsymbol{S}_{hkmn}$ lead to tendentially weaker spots. Note that this property does not depend on the total momentum transfer $\boldsymbol{S}$ and therefore not on (h, k). However, the same tendency was independently concluded for increasing orders (h, k) in the context of Debye-Waller factors. Therefore, the longer either $\boldsymbol{G}_{mn}^{\mathrm{sub}}$ *or* $\boldsymbol{G}_{hk}^{\mathrm{ads}}$ are, the less likely it is for the spot at $\boldsymbol{G}_{mn}^{\mathrm{sub}} + \boldsymbol{G}_{hk}^{\mathrm{ads}}$ to be intense.

4.1.6 Summary of important conclusions

While low-energy electron diffraction on modulated lattices is a complicated matter, the following simple conclusions were drawn in the previous sections:

i) The LEED pattern of an overlayer modulated by the underlying substrate consists of a convolution of the overlayer and substrate lattices, respectively.

ii) With sufficiently small modulation amplitudes, a generally weak energy dependence of the entire LEED pattern is expected.

iii) Spots arising from modulations perpendicular to the surface are best observed in the vicinity of the specular spot. Those due to lateral modulations disappear around the specular spot, but may be observed further away from it.

iv) Satellite spots due to a modulation are generally weaker than the parent spot, and the intensity of a (h, k, m, n) reflection tendentially decreases with increasing orders (h, k) *or* (m, n).

The last point prevents the appearance of infinite orders in a LEED image, as one might have intuitively assumed in the first place. Otherwise a convolution of incommensurate adsorbate and substrate lattices would produce ever new spot positions with an increasing number of lattice vectors incorporated into the convolution.

Note that the calculated structure factors are valid even if there are coincidences of reciprocal adsorbate and substrate lattice points, e.g., in the case of POL or LOL epitaxy. However, for a given reflection (h, k, m, n) in that case, an infinite number of additional combinations of (h', k') and (m', n') orders exist that result in the same spot position, i.e., they overlap. Hence, to be exact, one would have to sum up all of the corresponding structure factors in order to obtain the intensity of this one spot. With conclusion iv), however, it can be rationalized that only a limited number needs to be accounted for. If the factors decrease quickly enough and the most intense combination (h, k, m, n) dominates each spot, the above approach for incommensurate modulations is still valid. The advantage is the avoidance of the definition of commensurate super cells as an approximation to non-commensurate structures and therefore the retention of the convolution approach's flexibility: if one lattice, e.g., the overlayer lattice, changes in shape, scaling, or orientation, no new supercell has to be defined to describe the geometric pattern in reciprocal space or to calculate approximate intensities.

4.2 Application to LEED measurements

4.2.1 Improving geometric LEED analysis

As mentioned in the beginning of this chapter, in a thin epitaxial layer on top of a crystalline substrate, both multiple scattering and a substrate-induced modulation of the top layer result in a geometric convolution of both lattices in reciprocal space[h]. If there are diffraction spots due to either effect in a LEED experiment, they can be exploited to obtain highly precise structural information about the epitaxial layer. Qualitatively, this can be rationalized in the following way. Since the diffraction orders of those spots can be thought of as originating from both a substrate and an adsorbate lattice point (cf. Equ. 4.13), they carry the information of both lattices. Therefore, a simulation fitted to the entire pattern via LEEDLab [55] is very sensitive to the relative relation between the lattices, i.e., the epitaxy matrix.

Figure 4.5 shows a very illustrative example (same image twice with different overlays). Since the beam diameter of ≈ 1 mm is much larger than typical domain sizes of organic adsorbates deposited by OMBE, a LEED pattern usually consists of a superposition of domains with different, but symmetry-equivalent orientations [P1]. However, Fig. 4.5 displays a LEED image of a monolayer of PbPc on NG, exhibiting a single (point-on-line [129, 130]) domain over the entire substrate. This conclusion can be drawn because the LEED measurements feature only spots that can be explained with a single nearly square unit cell, without employing rotational or mirror symmetries of the substrate. Deviating from the other experiments in this work, the sample was prepared in chamber C by evaporating the molecules onto a heated NG substrate, namely at 380 K, and then cooled with liquid nitrogen. In contrast to the deposition of PbPc on NG as well as EG at room temperature, where rotational and mirror domains are observable [129, 130], the elevated thermal energy likely causes a higher mobility of the molecules on the substrate, facilitating the dominance of one domain and, supposedly, a mm-size organic 2D single crystal. Repeating this procedure with different samples produced films with dominating domains over large areas of the samples, even though falling short of a single domain covering the entire surface, but confirming reproducibility in principal.

Besides this remarkable property, the sample provides a visual confirmation of a geometric convolution, as a result of either multiple scattering between the PbPc lattice and the substrate or a modulation of the PbPc film due to the substrate: The image contains

---

[h] Note that the results of this section do not depend on the physical origin of the convolution. For an evaluation which process likely dominates see Sec. 4.2.2.

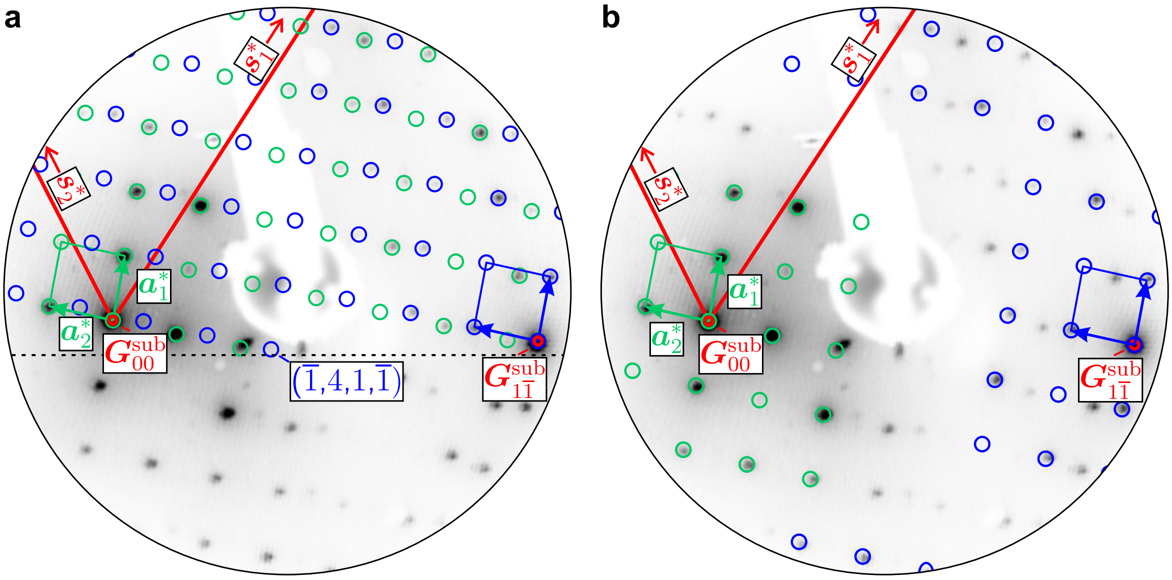

Figure 4.5: Intensity-inverted, distortion-corrected LEED image of 1 ML PbPc on NG at 63.1 eV and ≈ 130 K, with different overlays and featuring a single domain. The sample normal was tilted by 10° with respect to the incident beam. **a**: (Unmodulated) PbPc lattice originating from specular spot (green circles) is convoluted with a first order $(1, \bar{1})$ substrate spot (blue circles). An exemplary diffraction order is denoted in (h, k, m, n) notation (see text). **b**: Convolution of up to the second diffraction order with all first order substrate spots to avoid overlap (blue circles, except for the green ones originating from the specular spot).

spots that cannot be explained with the bare PbPc lattice alone which originates from the specular spot $(0, 0)$. Yet, they can be simulated by the same PbPc unit cell, originating from a first diffraction order of the substrate (depicted on the right-hand side of the image). The entire spot pattern hence can only be described satisfactorily if both the PbPc and the substrate unit cells have the correct shapes, sizes, and orientations. If, e.g., the PbPc unit cell is described well but the substrate lattice slightly deviates from the observed one, all adsorbate spots originating from substrate orders (except $(0, 0)$) will lie beside the corresponding observed spots as well. While the adsorbate lattice in organic-inorganic epitaxy is usually the one of interest, the substrate lattice is known in most cases. Nevertheless, as mentioned in Section 2.2 there are sources of error, such as the distance between the sample surface and the LEED device, that can lead to a wrong scaling of the LEED pattern [P2]. Instead of relying on only a few substrate spots to overcome scaling errors, *all* spots of the convoluted lattices can be used to determine the relation between adsorbate and substrate, which increases the reliability of the analysis drastically.

Based on these facts, a new fit routine that allows to exploit the additional information included in the convoluted lattices was suggested for LEEDLab. It was implemented by Falko Sojka (Institute for Solid State Physics, FSU Jena, Germany). It not only varies

Table 4.1: Epitaxy matrices of 1 ML PbPc on NG and EG, fitted with LEEDLab. Experimental uncertainties of the last significant digit, if available, are given in parentheses. Left column: Previous result from a multiple-domain LEED image on EG [129] without convoluted spots. An equivalent matrix has been chosen because the single domain in Fig. 4.5 represents a mirror domain with respect to Ref. [129]. Center column: Fit result of the structure in Fig. 4.5a with overlapping simulated spots. Right column: Fit result of the structure in Fig. 4.5b without overlapping simulated spots. For explanation see text.

no convolution [129]	convolution	convolution (no overlap)
$1.000(6) \cdot \begin{bmatrix} 6.072(4) & 4.956(4) \\ -2.469(4) & 3.967(4) \end{bmatrix}$	$\begin{bmatrix} 6.085(7) & 5.000(5) \\ -2.464(7) & 4.000(5) \end{bmatrix}$	$\begin{bmatrix} 6.12(4) & 5.00(2) \\ -2.50(3) & 4.01(2) \end{bmatrix}$
$a_1 = 13.8(2)$ Å	$a_1 = 13.84(7)$ Å	$a_1 = 13.9(1)$ Å
$a_2 = 13.8(2)$ Å	$a_2 = 13.91(7)$ Å	$a_2 = 14.0(1)$ Å
$\Gamma = 92.28(7)^\circ$	$\Gamma = 91.8(1)^\circ$	$\Gamma = 92.2(3)^\circ$
$\Phi = 50.1^\circ$	$\Phi = 50.38(8)^\circ$	$\Phi = 50.1(3)^\circ$

the adsorbate lattice vectors, but also scales and rotates the substrate lattice. Only for a certain epitaxial relation (epitaxy matrix) both the simulated spots originating from the $(0, 0)$ specular spot and the ones starting from higher substrate diffraction orders will match all the observable spots. With this analysis of the convoluted pattern, one can obtain similarly precise epitaxy matrix elements in the presented case of single-domain PbPc on NG and $\approx$ 70 evaluable spots as other works [129, 130] with $\approx$ 200 spots but without convolution analysis (cf. the first two columns of Table 4.1).

The epitaxy relation with respect to NG in this work does not differ significantly from that with respect to EG [129], confirming a previous identical comparison [130]. More importantly, the scaling error margin from the cited work is naturally canceled with the convolution approach applied here while the integer column, representative for the POL epitaxy, is perfectly met within the margin of error. Note that for this technique it is not necessary to directly observe diffraction orders from the substrate in the same image. The spots convoluted with a substrate diffraction order already carry the same information, if indexed correctly. However, it is advisable to take images at energies that allow for the observation of substrate spots in order to have a good starting point in terms of its orientation and potential scaling errors.

Further, special care has to be applied if a point-on-line or line-on-line registry with the substrate shall be verified objectively. In the point-on-line case of PbPc on NG for example, both the PbPc and NG lattices coincide in the primitive $(0, 1)$ substrate spot (out of range to the top left of the LEED pattern in Fig. 4.5). Hence, PbPc diffraction orders originating from the $(0, 0)$ spot and the $(0, 1)$ substrate spot begin to overlap if enough PbPc orders

(>2 in this case) are simulated from each origin because, e.g., $\boldsymbol{G}^{\mathrm{ads}}_{32} + \boldsymbol{G}^{\mathrm{sub}}_{00} = \boldsymbol{G}^{\mathrm{ads}}_{22} + \boldsymbol{G}^{\mathrm{sub}}_{01}$. If a double assignment of such overlapping spots is allowed, the fitting routine has no way to deviate from an integer column in the epitaxy matrix. To avoid such a potential bias towards coincidences the overlap has to be evaded. In Fig. 4.5b the convolution of both lattices has only been extended to the first substrate and the second PbPc orders so that no orders overlap. Table 4.1 contains the fit result from these 31 spots. It independently confirms the integer matrix elements without losing too much precision, which illustrates once more of the power of this approach.

However, in other cases, the following small and unlikely bias towards integer columns can hardly be excluded: If a structure is almost but not exactly in point-on-line registry with the substrate, additional spots due to the convolution might be so close to the spots originating from the specular spot that they cannot be distinguished by the peak finding algorithm of LEEDLab. Such a case, however, would be difficult to be analyzed correctly with any known technique. Fortunately, the intensity tendencies summarized in Sec. 4.1.6 may help to avoid this situation. One has to find spots where a low-index diffraction order is almost overlapped by only high-index orders which are likely to be too weak to distort the result of the peak finding algorithm (and thus the fit). Excluding all others from the fit may then work sufficiently well to judge the coincidence of reciprocal lattice points objectively.

Finally, the additional spots in Fig. 4.5 arising due to the convolution are stronger around the first substrate diffraction order compared to around the specular spot. This is also the case at various other incident beam energies (not shown). Moreover, while individual spot intensities vary with the beam energy, convoluted spots are always visible around the first-order substrate spot. Based on the discussion of the relatively weak energy dependence in the presence of modulation and the sensitivity of LEED with respect to perpendicular and lateral modulations, it is therefore concluded here that there likely is a sizeable amount of lateral modulation within the PbPc layer. This has not yet been confirmed with complementary techniques though.

4.2.2 Consequences for kinematic LEED

Modulation versus multiple scattering

Up to this point, only single-scattering processes have been considered, even though both multiple scattering between two unmodulated lattices and single scattering on a lattice modulated by another cannot be distinguished via geometric diffraction analysis, as stated before. Hence, it is difficult to determine which effect dominates the appearance of a

LEED pattern. However, it was possible to derive a rather simple LEED structure factor for modulated structures that makes testable predictions. In the following, these will be checked against calculations of a simplified multiple scattering model and compared to real measurements. It will be shown that, even though considering multiple scattering is necessary to calculate LEED intensities in detail (dynamic LEED) [108, 109], it might not be the dominating effect for modulated structures.

Epitaxial graphene on SiC(0001) with its large SiC(0001)$6\sqrt{3} \times 6\sqrt{3} - 30°$ supercell is a promising candidate for this comparison. It is well documented that the atomic positions of the graphene layers directly in contact with or close to the underlying Si-terminated SiC surface are modulated, mainly perpendicular to the surface (cf. Chap. 2 for structural details of EG). In a previous work a rather qualitative approach was pursued to explain the LEED pattern of EG in terms of a convolution of the graphene and the underlying SiC lattice [P1]. The LEED pattern intensities of both lattices were simulated individually in the kinematic limit and convoluted numerically. Even though a very simple procedure, it reproduced an experimental LEED image quite well. Already this simple approach is helpful because it produces only the spots observable in LEED. The definition of a large SiC(0001)$6\sqrt{3} \times 6\sqrt{3} - 30°$ unit cell to describe all spots generates many more potential spots than can be observed.

However, the effects due to the modulation of EG can now be studied in the context of the structure factor in Equ. 4.21 for crystals incommensurately modulated perpendicular to the surface, even though the modulation of EG produces a commensurate supercell with the SiC(0001) lattice. As mentioned in Sec. 4.1.6, even in the case of coincidences in reciprocal space, Equ. 4.21 is still valid. However, an infinite number of pairs of (h, k) and (m, n) lead to the same spot position and, in general, all contributing structure factors would have to be added. Consequently, the energy dependence of the intensity might be complicated. However, contributions with high enough indexes cease to be relevant, simplifying the situation and in the best case making it unnecessary to sum any structure factors for a single reflection $\boldsymbol{S}$.

Hence, it is interesting to compare single-scattering calculations on a modulated graphene layer on top of SiC with calculations including multiple scattering for the case of a flat graphene layer on SiC. A fully dynamic LEED calculation for this example would be challenging due to the size of the supercell and was not available in this work. However, an existing algorithm provided by Dr. Aimo Winkelmann (at that time: Max Planck Institute of Microstructure Physics, Halle, Germany) was adapted, with the main programming work done by Dr. Lars Matthes (at that time: Institute of Condensed Matter Theory and Solid State Optics, FSU Jena, Germany). It performs calculations of double scattering

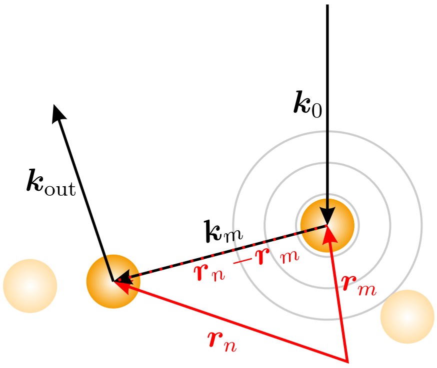

Figure 4.6: Schematic illustration of a simplified model for double scattering between a cluster of atoms and the necessary quantities (see text for details).

between a cluster of atoms via a simplified model of an elastic single and double scattering process ($k_0 = k_{\mathrm{out}}$ is preserved, cf. Fig. 4.6) which shall be described briefly below.

An incoming plane wave $\Psi_0(\boldsymbol{r}) = A_0 \mathrm{e}^{i\boldsymbol{k}_0\cdot\boldsymbol{r}}$ is scattered by an atom at $\boldsymbol{r}_m$ into a spherical wave centered at $\boldsymbol{r}_m$ that is proportional to the incoming wave amplitude Ψ_0. With the scattering amplitude $f_m(\boldsymbol{S}_m)$ (with the momentum transfer $\boldsymbol{S}_m = \boldsymbol{k}_0 - \boldsymbol{k}_m$) one obtains a spherical wave originating from $\boldsymbol{r}_m$:

$$\Psi_m(\boldsymbol{r}) = \Psi_0(\boldsymbol{r}_m) f_m(\boldsymbol{S}_m) \frac{\mathrm{e}^{i\boldsymbol{k}_m\cdot(\boldsymbol{r}-\boldsymbol{r}_m)}}{|\boldsymbol{r}-\boldsymbol{r}_m|}. \tag{4.30}$$

This corresponds to the single-scattering part of the algorithm. If the wave functions $\Psi_m(\boldsymbol{r})$ are evaluated in the direction $\boldsymbol{k}_m = \boldsymbol{k}_{\mathrm{out}}$ at a distance $|\boldsymbol{r}| \approx R$ to the sample that is large compared to atomic distances and summed over all contributing atoms, this would amount to the single scattering wave function Ψ_{SS} only.

For a double scattering model, this spherical wave is taken as a new incoming wave and similarly scattered by a second atom at $\boldsymbol{r}_n$ (with momentum transfer $\boldsymbol{S}_n = \boldsymbol{k}_m - \boldsymbol{k}_n$):

$$\begin{aligned} \Psi_{mn}(\boldsymbol{r}) &= \Psi_m(\boldsymbol{r}_n) f_n(\boldsymbol{S}_n) \frac{\mathrm{e}^{i\boldsymbol{k}_n\cdot(\boldsymbol{r}-\boldsymbol{r}_n)}}{|\boldsymbol{r}-\boldsymbol{r}_n|} \\ &= \frac{A_0 f_m(\boldsymbol{S}_m) f_n(\boldsymbol{S}_n)}{|\boldsymbol{r}-\boldsymbol{r}_n||\boldsymbol{r}_n-\boldsymbol{r}_m|} \mathrm{e}^{i(\boldsymbol{k}_0\cdot\boldsymbol{r}_m + \boldsymbol{k}_m\cdot(\boldsymbol{r}_n-\boldsymbol{r}_m) + \boldsymbol{k}_n\cdot(\boldsymbol{r}-\boldsymbol{r}_n))}. \end{aligned} \tag{4.31}$$

If the interference pattern is detected in the direction of $\boldsymbol{k}_n = \boldsymbol{k}_{\mathrm{out}}$ at a large distance $|\boldsymbol{r}| \approx R$ the total wave function of one double scattering event can be written as

$$\Psi_{mn}(\boldsymbol{r}) = \frac{A_0}{R} \frac{f_m(\boldsymbol{S}_m) f_n(\boldsymbol{S}_n)}{|\boldsymbol{r}_n-\boldsymbol{r}_m|} \mathrm{e}^{ikR} \mathrm{e}^{i(\boldsymbol{k}_0\cdot\boldsymbol{r}_m + k|\boldsymbol{r}_n-\boldsymbol{r}_m| - \boldsymbol{k}_{\mathrm{out}}\cdot\boldsymbol{r}_n)}, \tag{4.32}$$

using the fact that $\boldsymbol{k}_m$ is parallel to $\boldsymbol{r}_n - \boldsymbol{r}_m$. Summing over all contributing atoms m and n results in the double scattering wave function Ψ_{DS}.

As it would not be physically meaningful to determine double scattering intensities without single scattering processes that always take place, the total wave function $\Psi_{\text{total}} = \Psi_{\text{SS}} + \Psi_{\text{DS}}$ has to be calculated before obtaining the intensities $|\Psi_{\text{total}}|^2$. This approach neglects more complicated scattering paths and is thus less powerful in predicting correct LEED intensities due to multiple scattering than more complex models [102]. However, it is deemed sufficient for the following discussion. Moreover, it would allow to calculate even incommensurate systems contrary to existing dynamic LEED methods [102].

Since the main conclusion from the structure factor in Equ. 4.21 was a low energy dependence of the LEED pattern of modulated structures, only the interference part of the scattering process shall be discussed. Hence, as a simplification the form factors in Equ. 4.32 are set to 1 for all atoms. In the present case of graphene on SiC, the only scattering amplitudes of carbon and silicon should be similar enough to avoid a too large distortion of the results. The scaling factor of $A_0 \mathrm{e}^{ikR}/R$ can be ignored as well. The remaining phases are mapped for an incoming wave $\boldsymbol{k}_0 = k(0, 0, -1)$ over all accessible values of $\boldsymbol{k}_{\text{out}}$. Even though backward scattering is of interest here, forward scattering is calculated as well in order to normalize the intensity over an entire 3D sphere. For this, $\boldsymbol{k}_{\text{out}}$ is split into $\boldsymbol{k}_{\text{out},\parallel}$ in the surface plane and $\boldsymbol{k}_{\text{out},\perp} = \sqrt{k^2 - \boldsymbol{k}_{\text{out},\parallel}^2}\,(0, 0, \pm 1)$ perpendicular to the surface (with a positive k_z for backward scattering and a negative one for forward scattering) and the mapping is performed over all $|\boldsymbol{k}_{\text{out},\parallel}| \leq k$ in both backward and forward direction. The sum I_{total} of all intensities obtained this way is used to normalize the backward scattering intensity maps.

The atomic clusters for the calculations were assembled as follows. For the double scattering calculation, flat graphene was positioned at 2.3 Å over one Si-terminated SiC bilayer and a circular domain with a diameter of 20 graphene unit cells was cut out (for crystal parameters see Chap. 2). In accordance with a model for modulations perpendicular to the surface discussed in the context of lateral modulations in Sec. 4.1.3, the modulated graphene layer (buffer layer) was obtained by vertically displacing the atoms proportional to a “map” of the SiC surface. The latter was obtained via VESTA which can model the electron density at the SiC surface based on Fourier transforms of atomic scattering factors from free atoms [131]. The result is a nearly sinusoidal map with the lattice constant of SiC and the resulting modulated graphene layer looks sufficiently similar to one that was calculated via density functional theory (DFT) [39]. The modulation amplitude is 0.4 Å with the mean separation to the SiC bilayer being the same as in the case of the flat graphene, which seems reasonable based on DFT [39]. Different values for both separation and modulation amplitude were tested as well with no significantly different conclusions.

Figure 4.8 shows the results of both the single scattering calculations for modulated

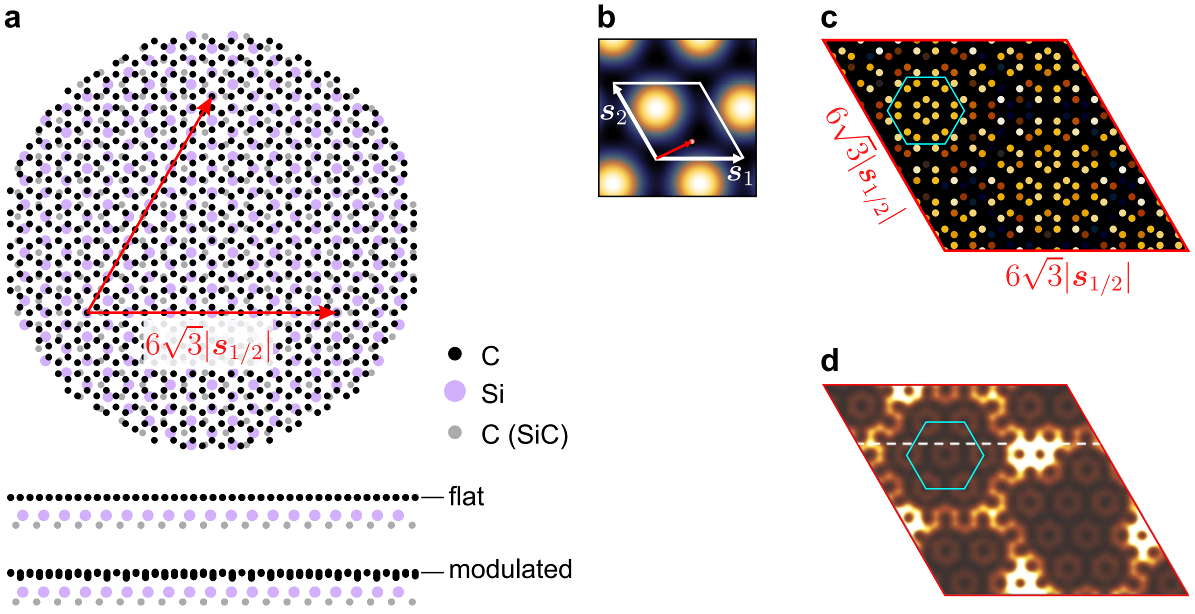

Figure 4.7: **a**: Cluster for single/double-scattering calculations in top view and the side views of the flat and modulated buffer layer configurations, respectively. **b**: Map of approximate SiC surface electron density (with SiC periodicity) used as the modulating function $u_\perp(\tau_1, \tau_2)$. **c**,**d**: Comparison of the simplified height modulation of the buffer layer within the commensurate supercell generated in this work (height color-coded, bright is high) and that from Ref. [39] calculated with DFT. The agreement is reasonable (note features marked in light blue).

graphene on a bilayer of SiC (left column) and double scattering calculations for flat graphene on a bilayer of SiC (center column) at exemplary energies for which LEED measurements were carried out as well, displayed in the right column. All maps represent the backward scattering intensities. As is apparent from Fig. 4.8, the pattern of the modulated structure remains mostly unaltered with increasing energy, except for the widening range of accessible spots, and matches the corresponding measurements very well. Especially the number of observable spots, which is much smaller than the geometrically possible ones due to the large supercell, compares very well. Only in the 126 eV example the similarity is less striking. Note that, while it would have been possible, it is not even necessary to include a full supercell in the atomic cluster (cf. Fig. 4.7a).

Double scattering between the flat crystals, on the other hand, is much more energy-dependent than single scattering on modulated crystals and the resulting patterns do not describe the experiment very well. The different energy dependencies can be validated by extracting the intensities of different reflections in dependence of the beam energy. This has been done for the spots marked in Fig. 4.9b in the energy range of 10. . . 130 eV. By comparing the two charts for single scattering on the modulated crystal and double scattering between the flat layers it is obvious that the latter produces intensities in very limited energy ranges for different spots, resulting in strongly varying LEED patterns at

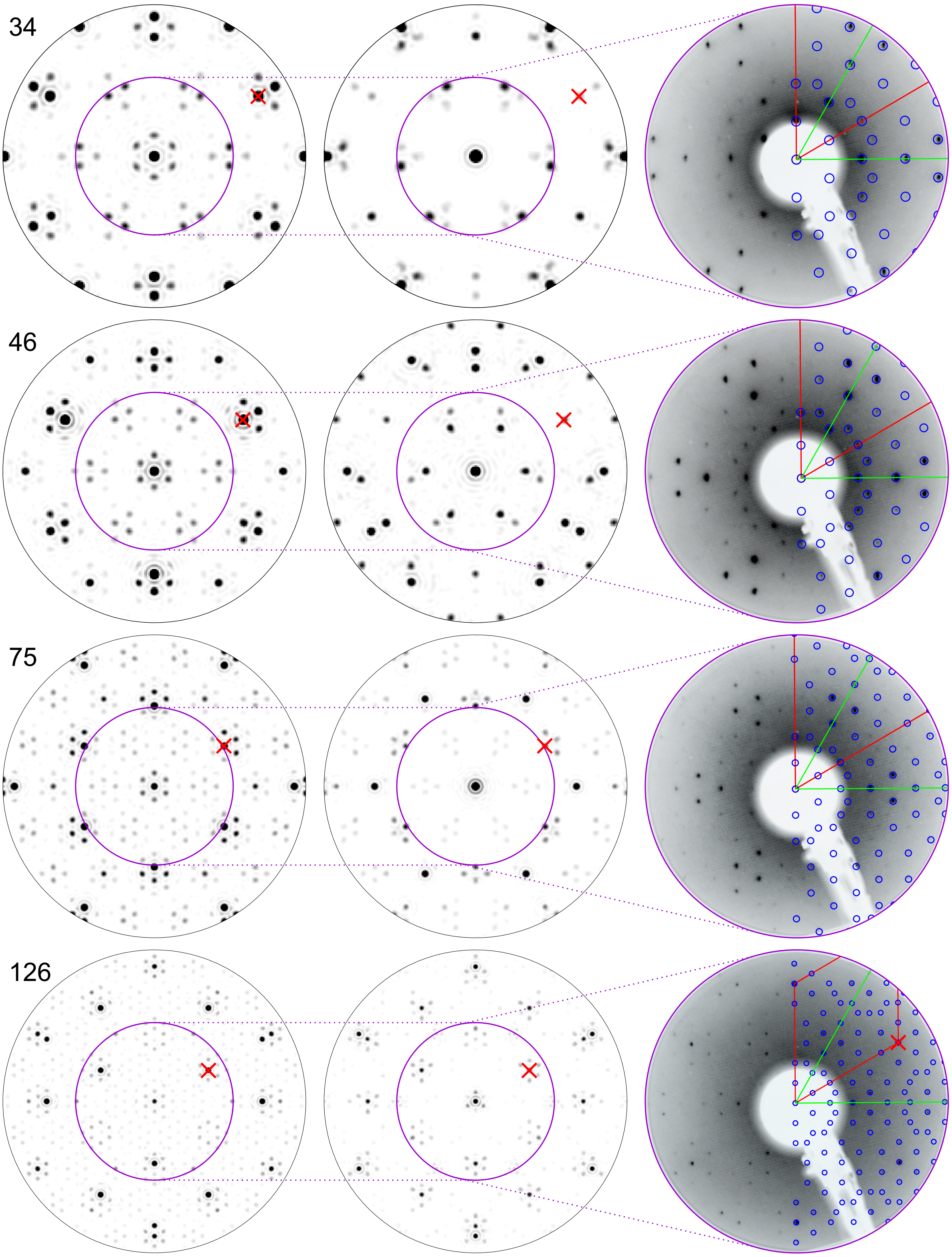

Figure 4.8: Single scattering intensities at energies given in eV for modulated EG (left column), and single+double scattering intensities for unmodulated EG (center column), each on one SiC bilayer. Right column: Corresponding LEED patterns with an overlay of a convolution of SiC (red) and EG (green) lattices to the fourth order (blue circles). Comparable regions (purple circles) and a first-order spot of SiC (crosses) are marked.

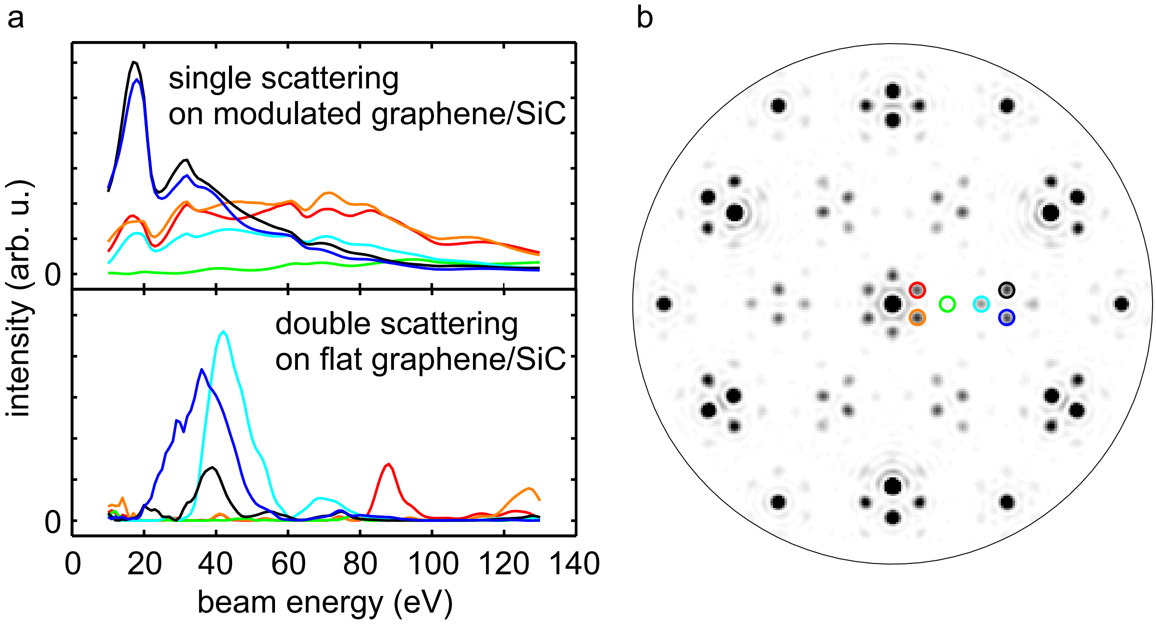

Figure 4.9: **a**: Intensities of different reflections in the single scattering (top chart) and double scattering (bottom chart) images in Fig. 4.8 in dependence of the beam energy. The positions are marked as circles of corresponding color in panel **b**, which shows the 46 eV single scattering calculation of Fig. 4.8 as a reference.

different energies. On the other hand, the curves in the modulated case are much smoother and all spots are visible for an extended energy range. Further, even though the intensity ratio of, e.g., the black and red spots in Fig. 4.9b switches in favor of the latter at ≈ 45 eV, the change of ratios is rather slow. This leads to a slowly changing LEED pattern for the modulated structure, as was concluded from Equ. 4.21. Hence, the approximation $\boldsymbol{u}\cdot\boldsymbol{S} \ll 1$ used to conclude the low energy dependence of LEED patterns from modulated surfaces seems to be justified even for such rather large modulation amplitudes and an energy of ≈ 75 eV. Note that, even though a bilayer of SiC was included below the modulated graphene layer for the sake of higher similarity of the two clusters, it only contributes to the SiC main reflections. This contribution is energy-dependent and the entire pattern would change even less with the incident beam energy with only the modulated layer.

In summary, the LEED pattern of the modulated buffer layer seems to be dominated by the modulation, while multiple scattering effects can only play a minor role. Moreover, the main predictions of the simplified approach to explain LEED patterns of modulated structures are apparently confirmed. Therefore, the structure factors of Equ. 4.15 and more specifically of Equ. 4.21,

$$F(\boldsymbol{S}) \approx iS_\perp \sum_{\mu=1}^{N} \left[f_\mu(\boldsymbol{S}) \mathrm{e}^{i(\boldsymbol{G}_{hk}^{\mathrm{ads}}\cdot\boldsymbol{r}_\mu + S_\perp r_{\mu,\perp})} \sum_{\nu=1}^{M} h_{\mu\nu,\perp}(\boldsymbol{G}_{mn}^{\mathrm{sub}}) \mathrm{e}^{i\boldsymbol{G}_{mn}^{\mathrm{sub}}\cdot\boldsymbol{r}_\nu} \right], \tag{4.33}$$

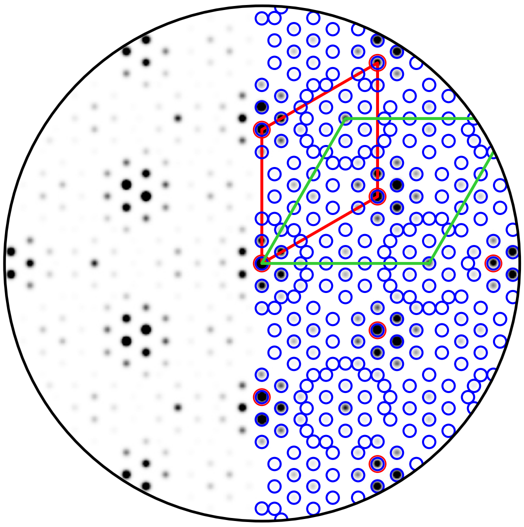

Figure 4.10: Result of the LEED pattern simulation via Equations 4.33 and 4.34, agreeing very well with the single-scattering simulation and the experimental LEED patterns in Fig. 4.8. Spots are plotted as 2D Gaussian functions with a height proportional to the spot intensity. The overlay on the right is the geometric convolution of the SiC (red) and EG lattices (green) up to the fourth order each.

multiplied with the Debye-Waller factor in Equ. 4.29 for statistical disorder in a modulated overlayer,

$$D = \exp\left(-\frac{1}{4}\left(G_{hk}^{\mathrm{ads}}\right)^2\left\langle\delta_{\parallel}^2\right\rangle\right)\exp\left(-\frac{1}{2}S_{\perp}^2\left\langle\delta_{\perp}^2\right\rangle\right), \tag{4.34}$$

can be used to simulate the LEED intensities $|F(\boldsymbol{S})\,D|^2$ of the modulated layer of graphene. The spot positions are obtained via the convolution of both the SiC and graphene reciprocal lattices, each up to the fourth diffraction order. Additional orders are only weaker and thus not necessary. Moreover, no convoluted spots overlap at this level. Since the atomic form factors f_μ are expected to follow the same trend as $S_\perp$ and not to have a significant influence on the pattern, they are assumed as scalar. The atomic basis of graphene is $\boldsymbol{\xi}_\mu = \{(0,0,0),(2/3,1/3,0)\}$.[i] Since the modulating function $u_\perp(\tau_1,\tau_2)$ is dominated by the Si atoms and nearly 2D-sinusoidal (cf. map in Fig. 4.7), the substrate basis can be set to $\boldsymbol{\xi}_\nu = (0,0,0)$ and the Fourier coefficients of the modulation $h_{\mu\nu,\perp} = h_{\mu,\perp}$ are assumed to quickly converge to zero in equivalence to Fig. 3.2: $h_{\mu,\perp}(G_{mn}^{\mathrm{sub}}\ [\text{Å}^{-1}]) \sim \mathrm{e}^{-G_{mn}^{\mathrm{sub}}/4}$. The squared (thermal) disorder is assumed to be $(\delta_\perp)^2 \approx (\delta_\parallel)^2 = (0.05\ \text{Å})^2$, comparable to graphite [132], but the factor is not as decisive here as it presumably is for organic overlayers with more flexible bonds.

Figure 4.10 shows the result of the evaluation of the structure factor at the energy of 75 eV, however, the pattern's appearance is nearly energy-independent. It resembles the corresponding LEED pattern and the single-scattering calculation remarkably well. Hence, it is a useful approach for the given system of EG on SiC(0001). The usefulness will be even higher for overlayers which change the shape or orientation of their unit cells with respect to the substrate. Already the system of graphene layers on the opposite face of

---

[i] The primitive lattice vectors of both the substrate and graphene are defined here as enclosing an angle of 120°.

SiC(0001), i.e., the C-face, shows that a variety of different orientations of the same layer results in widely different modulation periods [133]. This could easily be accounted for with the presented approach by only changing one parameter, namely the orientation of the overlayer lattice.

4.2.3 Systematic absences

Systematic absences in general diffraction

In crystallography, starting from the various symmetry elements like translations, rotations, reflections, or combinations thereof, a maximum of 230 possible space groups are derived. Selected space groups feature certain symmetry elements like glide planes (e.g., reflection on the plane (010) and translation by $\frac{1}{2}\boldsymbol{a}_1$) or screw axes (e.g., a 2_1 axis with 2-fold rotation around $\boldsymbol{a}_1$ and translation by $\frac{1}{2}\boldsymbol{a}_1$)[j], in which case specific selection rules apply to diffraction orders that can be expected, or conversely, to orders that are systematically extinguished – so-called systematic absences: F_{h0l} and F_{h00}, respectively, would be zero for odd values of h in these two cases [134, p. 29].

It is a popular student exercise to validate these extinctions for simple examples by calculating the orders for which the corresponding structure factor vanishes. Here, a brief clarification shall be made on a very common misunderstanding concerning systematic absences due to crystal symmetry versus ones merely due to a disappearing structure factor, before discussing the implications for modulated crystals.

Apparently, the distinct absence of spots in the presence of certain symmetries has led some researchers to assume that the underlying symmetry operations, and with them the different space groups, can be inferred from these absences. For example, the author of Ref. [135] states that the absent reflections "arise from the centring of the unit cell and/or the presence of translational symmetry elements – glide planes and screw axes. The identification of systematic absences is very useful since it provides the 'first step' in crystal structure determination" [135, p. 224]. Referring to the extinctions described above, "Glide-plane symmetry is the only possible cause of this kind of extinction…", according to Ref. [108, p. 76]. However, one counterexample will be presented below to show that *no* symmetry besides the translational one is necessary to produce the absences noted above. Moreover, it will be shown that under favorable circumstances even incommensurately modulated layers, i.e., ones without strict translational symmetry, may feature such systematic absences.

---

[j] Here, the three primitive vectors $\boldsymbol{a}_1$, $\boldsymbol{a}_2$, and $\boldsymbol{a}_3$ are used in agreement with the previous part of this work, but contrary to the conventional $\boldsymbol{a}$, $\boldsymbol{b}$, and $\boldsymbol{c}$.

First, assume a general (triclinic) crystal with primitive vectors $\boldsymbol{a}_1$, $\boldsymbol{a}_2$, and $\boldsymbol{a}_3$ that has no symmetry elements except for the translational symmetry. Further, the crystal shall have an atomic basis consisting of an arbitrary molecule with N atoms at the relative coordinates $\boldsymbol{\xi}_\mu$ and a modified “copy” of that molecule whose atoms are shifted by 0.5 along $\boldsymbol{a}_1$ and by *random* values δ_μ along $\boldsymbol{a}_2$, essentially ripping apart the second molecule. Note though, that this keeps the coordinates along $\boldsymbol{a}_3$ constant. The total basis is thus:

$$\left\{ \begin{pmatrix} \xi_{1,1} \\ \xi_{1,2} \\ \xi_{1,3} \end{pmatrix}, \begin{pmatrix} \xi_{1,1} + 0.5 \\ \xi_{1,2} + \delta_1 \\ \xi_{1,3} \end{pmatrix}, \ldots, \begin{pmatrix} \xi_{N,1} \\ \xi_{N,2} \\ \xi_{N,3} \end{pmatrix}, \begin{pmatrix} \xi_{N,1} + 0.5 \\ \xi_{N,2} + \delta_N \\ \xi_{N,3} \end{pmatrix} \right\} \tag{4.35}$$

Due to the random structure of the second molecule and the least symmetric triclinic crystal there is no chance of symmetry-related systematic absences. Nevertheless, when the structure factor F_{h0l} is calculated for the above basis (thanks to $k = 0$, all random δ_μ are rendered irrelevant)

$$\begin{aligned} F_{h0l} =& f_1 \left(\mathrm{e}^{2\pi i(h\xi_{1,1}+l\xi_{1,3})} + \mathrm{e}^{2\pi i(h\xi_{1,1}+h/2+l\xi_{1,3})} \right) + \cdots + \\ & f_N \left(\mathrm{e}^{2\pi i(h\xi_{N,1}+l\xi_{N,3})} + \mathrm{e}^{2\pi i(h\xi_{N,1}+h/2+l\xi_{N,3})} \right) \\ =& f_1 \mathrm{e}^{2\pi i(h\xi_{1,1}+l\xi_{1,3})} \left[1 + \mathrm{e}^{\pi i h} \right] + \cdots + f_N \mathrm{e}^{2\pi i(h\xi_{N,1}+l\xi_{N,3})} \left[1 + \mathrm{e}^{\pi i h} \right], \end{aligned} \tag{4.36}$$

using $\mathrm{e}^{\pi h i} = (-1)^h$ due to the integer h, the same extinctions are found that would be expected from the exemplary glide plane noted above:

$$\begin{aligned} F_{h0l} &= \left[1 + (-1)^h \right] \sum_{\mu=1}^{N} f_\mu \mathrm{e}^{2\pi(h\xi_{\mu,1}+l\xi_{\mu,3})} \\ &= \begin{cases} 0 & \text{for odd } h \\ 2 \sum_{\mu=1}^{N} f_\mu \mathrm{e}^{2\pi(h\xi_{\mu,1}+l\xi_{\mu,3})} & \text{for even } h \end{cases} \end{aligned} \tag{4.37}$$

While the example with one intact and one torn-apart molecule seems drastic, it corresponds to the most general case and illustrates the necessary and sufficient condition for this specific extinction: For every atom in the atomic basis and a set of lattice planes through this atom ($\{100\}$ in the above case) there needs to be a partner atom of the same kind *anywhere* on a plane that halves the lattice plane distance of this set. Such a setup doubles the frequencies in reciprocal space needed to describe this lattice plane set and hence leads to systematically absent spots.

The condition can be fulfilled for arbitrary lattices, as only the relative basis coordinates are relevant for the structure factor. Further, as can be seen from Equ. 4.37, this is true for any value of l, because the third coordinates of each pair of partner atoms were chosen to be equal. Should the third coordinates of each pair of partner atoms be subject to random changes, too, then Equ. 4.37 is only true for $l = 0$, i.e., $F_{h00} = 0$ for odd h. This resembles the selection rule for the exemplary screw axis mentioned above.

In the case of a tetragonal crystal the exemplary glide plane along $\boldsymbol{a}_1$ is simply a special case of Equ. 4.37. The bases of such crystals could be described by Equ. 4.35 and merely impose a restriction onto the δ_μ, i.e., they would not be independent of each other but need to resemble a reflection on the glide plane. Similarly, a 2_1 screw axis along $\boldsymbol{a}_1$ extinguishing F_{h00} for odd h is included as a special case in which both the second and the third coordinates of the partner atoms cannot be arbitrary anymore, but must conform to the rotation around the screw axis.

For these reasons, systematic absences should *not* be seen as a consequence of special symmetry operations but simply as a result of the atomic basis architecture – the former are included as special cases in the latter. Consequently, even though oblique lattices cannot have glide plane symmetry, they may feature the same absences as if they had it.

Systematic absences in LEED

It has been reported before that LEED spots may be systematically missing for all incident beam energies solely due to the lattice basis [136]. The authors stated that this would be possible only for a flat 2D basis. However, this is proven wrong by Equ. 4.37 which is valid for a 2D crystal with a 3D basis if $l\xi_{\mu,3}$ is replaced with $S_\perp r_{\mu,\perp}$. Hence, systematic extinctions are possible for oblique lattices, 3D bases, and all $S_\perp$, i.e., all beam energies, as long as there are always partner atoms with matching (pairwise the same) values of $r_\perp$.

Such an example is likely shown in Fig. 4.11. The images were provided by Christian Zwick (Institute for Solid State Physics, FSU Jena, Germany). They show a STM measurement, its fast Fourier transform (FFT), and a corresponding LEED image of another phthalocyanine derivative, namely $SnCl_2Pc$ [137], deposited on the (111) face of a Ag crystal. Compared to PbPc, the Pb atom is replaced with Sn, bonded to two Cl atoms above and below the ligand plane. Hence, it is a molecule with a 3D structure. The coverage is ≈ 0.6 ML.

As can be seen easily in the STM image, the $SnCl_2Pc$ unit cell contains two molecules. Apparently, both have the same orientation and height, and one is simply translated with respect to the other by $\frac{1}{2}\boldsymbol{a}_1 + \delta\boldsymbol{a}_2$ with a seemingly arbitrary factor δ, as depicted in Fig. 4.11a. Note that the unit cell is not rectangular which is confirmed by LEED measurements (cf. Fig. 4.11b). Nevertheless, in the LEED image and in the FFT of the STM image all accessible $(h, 0)$ orders are missing for odd h. The absences were retained

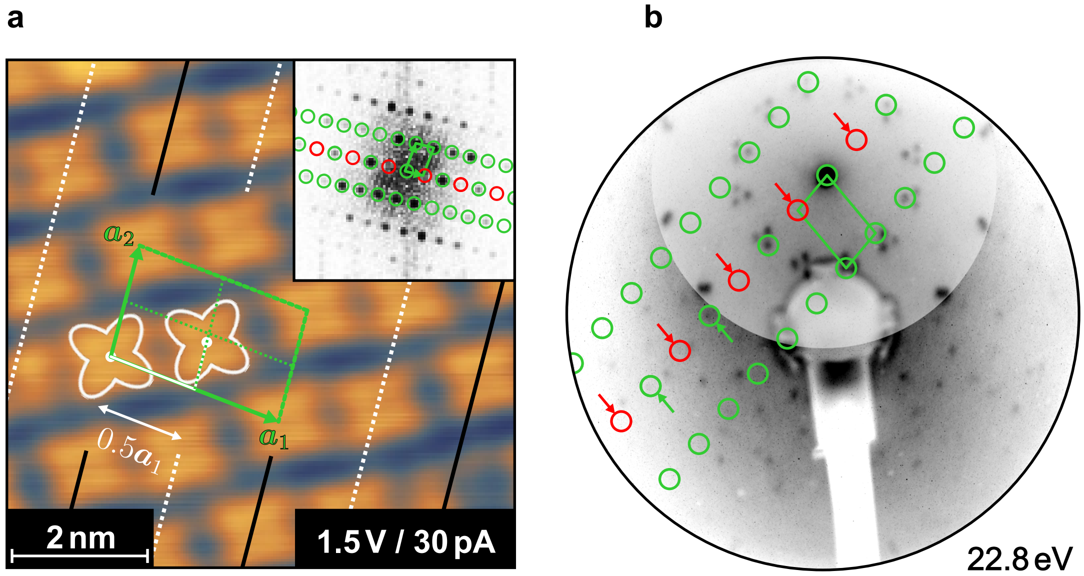

Figure 4.11: **a**: Zoom of a STM image of a 0.6 ML $SnCl_2Pc$ film on Ag(111). The two molecules per unit cell are shifted by $0.5\boldsymbol{a}_1 + \delta\boldsymbol{a}_2$ with respect to each other, with $\delta \neq 0.5$. Lattice lines containing molecular centers are marked with black and dotted white lines. The FFT of the larger original image (not shown) in the inset features absences along $\boldsymbol{a}_1^*$ for odd orders h, marked in red. Two adjacent lines of spots are marked in green for comparison. **b**: LEED image of the structure with the same missing orders, equivalently marked for one exemplary domain. To enhance the very faint higher-order spots the contrast is optimized inhomogeneously. Two very faint, but indeed observable spots are marked with green arrows. All images were kindly provided by Christian Zwick (see text).

as well at other LEED energies tested by Zwick in a range of $\approx 20 \ldots 35$ eV, validating Equ. 4.37 for an oblique lattice and a 3D basis.

It is worth noting again, however, that it would break down if not every atom has a correctly shifted partner atom with the same coordinate $r_\perp$. If, for example, the $SnCl_2Pc$ unit cell contained two shuttlecock-shaped phthalocyanine molecules instead (e.g., PbPc), one with Pb pointing up at $\xi_1 = (0, 0)$ and one with Pb pointing down at $\xi_2 = (0.5, \delta)$ with an arbitrary δ, the partner atoms from each molecule would have different values of $r_{\mu,\perp}$.[k] Hence, F_{h0} would only systematically disappear for odd h in the reciprocal plane of $S_\perp = 0$. However, that plane cannot be probed with LEED and the spots would not be systematically absent.

Systematic absences in modulated 2D lattices

Even though Equ. 4.21 for height-modulated structures in its general form is not the product of two structure factors that can vanish independently, there are (likely common) cases where it is. The only prerequisite is an adsorbate containing exclusively parts (atoms

---

[k] This specific example could be seen as a 2_1 screw axis in 2D.

or molecules[1]) of which each is modulated in the same way by the substrate, i.e., all $h_{\mu\nu} = h_\nu$. Then, Equ. 4.21 can be split into two factors:

$$F(\boldsymbol{S}, m, n) = iS_\perp \left[\sum_{\mu=1}^{N} f_\mu(\boldsymbol{S}) \mathrm{e}^{i(\boldsymbol{G}^{\mathrm{ads}}_{hk} \cdot \boldsymbol{r}_\mu + S_\perp r_{\mu,\perp})} \right] \left[\sum_{\nu=1}^{M} h_\nu(\boldsymbol{G}^{\mathrm{sub}}_{mn}) \mathrm{e}^{i\boldsymbol{G}^{\mathrm{sub}}_{mn} \cdot \boldsymbol{r}_\nu} \right]. \tag{4.38}$$

Should either of the (unmodulated) lattices exhibit systematic extinctions of its structure factor this would translate into systematic absences for the modulated structure as well. Hence, even though for glide-symmetry-like systematic absences in LEED the adsorption heights of the respective partner atoms must be exactly the same in general, heights that are regularly modulated by the substrate constitute an exception and allow for a persistence of the absences. Specifically, systematic extinctions would not require the occupation of distinct adsorption sites as assumed elsewhere [108, p. 312]. Unfortunately, there is no data available yet on a potential modulation of the $\mathrm{SnCl_2Pc}$ structure to confirm or refute this expectation.

4.3 Application to Fourier-transformed STM images

The signal of a scanning tunneling microscope, i.e., the tunneling current or the tip position perpendicular to the surface, is converted into a brightness scale and mapped as a 2D function of space. If the structure in the image is periodic, the map can be expanded into a 2D Fourier series $I(\boldsymbol{r}) = \sum_{\boldsymbol{G}^{\mathrm{ads}}_{hk}} F(\boldsymbol{G}^{\mathrm{ads}}_{hk}) \mathrm{e}^{-i\boldsymbol{G}^{\mathrm{ads}}_{hk} \cdot \boldsymbol{r}}$ with all vectors defined in $\mathbb{R}^2$ and a fast Fourier transform (FFT) would show discrete spots at the spatial frequencies $\{\boldsymbol{G}^{\mathrm{ads}}_{hk}\}$. STM images, especially of organic layers, frequently exhibit so-called Moiré patterns, i.e., a longer-range modulation of the periodic brightness, if the overlayer lattice is not commensurate with the substrate lattice. This can be due to a varying local density of states or a real height modulation. Analogously to Section 4.1.3, a modulation of the brightness due to an underlying periodic substrate changes the series into $I(\boldsymbol{r}) = \sum_{\boldsymbol{G}^{\mathrm{ads}}_{hk} + \boldsymbol{G}^{\mathrm{sub}}_{mn}} F(\boldsymbol{G}^{\mathrm{ads}}_{hk} + \boldsymbol{G}^{\mathrm{sub}}_{mn}) \mathrm{e}^{-i(\boldsymbol{G}^{\mathrm{ads}}_{hk} + \boldsymbol{G}^{\mathrm{sub}}_{mn}) \cdot \boldsymbol{r}}$ and produces additional spots geometrically yielding a 2D convolution of the adlayer and substrate lattices. Hence, it is possible to apply a geometric analysis to STM FFTs featuring Moiré patterns similar to the LEED analysis in Section 4.2, allowing for a fit of the epitaxy matrix. The suggested approach inherently differs from the simulation of Moiré patterns applied elsewhere, [58, 61] or [P5], where a manual comparison with the experiment is necessary. However, there are some

---

[1] The sum over μ may as well be seen as a sum over all molecules in the unit cell, not atoms. In that case, the form factors f_μ contain the information about the scattering "shape" of each molecule, not each atom.

peculiarities that need to be addressed.

Distortions in STM images

STM images are usually distorted due to limitations of the piezo scanner. These range from merely imperfect scaling calibrations and thermal drift to the non-linearity and hysteresis of the piezo elements. A linear distortion can be described (and in principal corrected) by a single transformation matrix $\underline{M}$ that maps position vectors from the distorted image into a virtual undistorted image: $\underline{M}\boldsymbol{v}^{\text{distorted}} = \boldsymbol{v}^{\text{undistorted}}$, the most important examples being scaling and shear distortions. At the low temperatures of the STM used in this work (1.1 . . . 4.4 K), the distortions due to thermal drift are very small and almost linear throughout an image. Naturally, an imperfect calibration of the lateral scan dimensions correspond to a linear distortion as well. Non-linear distortions will result in smeared frequencies in the FFT and are hence undesirable. However, non-linear effects can be reduced to nearly linear distortions by cropping parts of the STM image where the non-linearity dominates. Usually this would be the edges of the image.

The advantage of having only linear distortions in an STM image is that the epitaxy matrix resulting from the geometric Fourier analysis is not influenced by them. A sheared STM image still produces sharp frequencies in a corresponding FFT with the shear translating into reciprocal space as well. However, since both the adsorbate and the substrate are sheared in the same way, the relation between them, i.e., the epitaxy matrix, is retained (cf. Appendix A.II for a mathematical description) and can in principle be extracted without systematic errors. For this LEEDLab can be employed.

Using LEEDLab with STM FFTs

Figure 4.12a shows an STM image of 1 ML of PbPc on NG, the system that exhibits a point-on-line (POL) registry according to LEED measurements discussed in Sec. 4.2.1. As is normally the case, only the top lattice (PbPc) is directly visible in the image while the convolution approach in LEEDLab requires two lattices, i.e., those of the adsorbate and the substrate. However, due to the POL epitaxy type, the adsorption sites of the PbPc molecules with respect to the substrate unit cells vary across the domain producing a Moiré pattern in form of a brightness modulation. This can be seen in the form of spots besides the red PbPc lattice in the corresponding FFT in Fig. 4.12b.

If no starting point at all is available for the simulation of the substrate lattice, however, it may be difficult to correctly assign the observed spots to the simulated convoluted spots. The sensitivity of the pattern towards small changes of the substrate lattice is simply too strong. The azimuthal rotation of the substrate might be unknown as well as the amount of shear in the image. Nevertheless, there are three possible scenarios that might allow a Fourier analysis of the Moiré pattern:

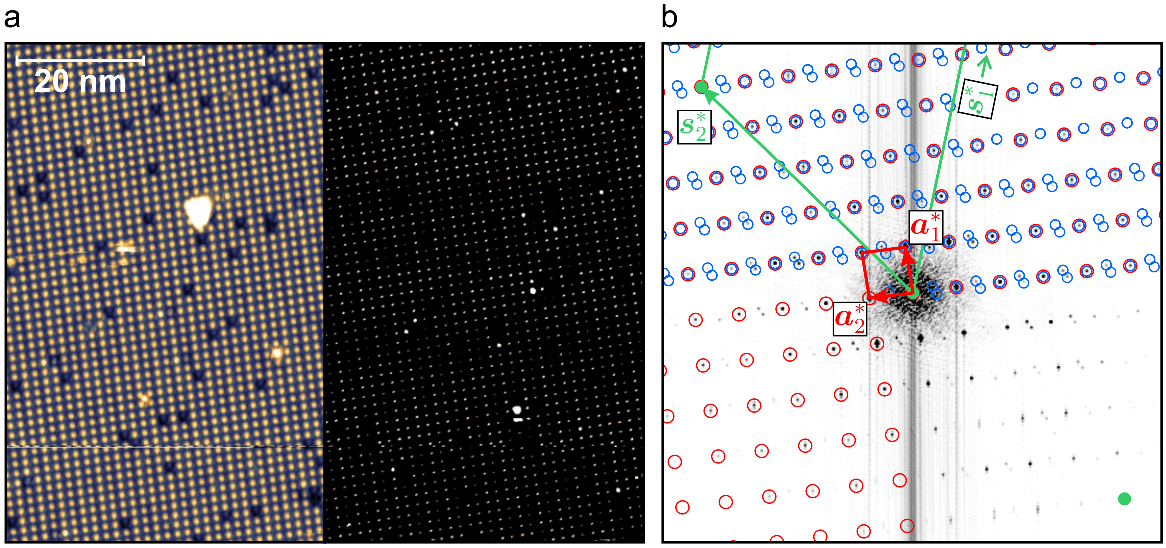

Figure 4.12: **a**: STM image of 1 ML PbPc on NG at +1.2 V, 15 pA and 1.2 K. The contrast has been enhanced in the right half of the image to make the Moiré pattern visible. **b**: Inverted FFT of the normal-contrast image of panel **a** featuring the PbPc lattice (red) and the convolution spots (blue) due to an assumed substrate lattice (green).

1. Direct information about the substrate lattice is available in the image either by resolving the substrate below the adsorbate or by having an area next to the adsorbate where the bare substrate is resolved.
2. There exist other STM images of the bare substrate from the same sample and under similar conditions (which affect orientation and scaling) from which an estimate of the substrate lattice can be inferred.
3. There is at least approximate information on the epitaxy matrix from other methods like LEED.

In the first 2 cases, the reciprocal substrate lattice and hence the convolution with the adsorbate lattice can be simulated directly. Here, the third way can be implemented as LEED data is available in form of the epitaxy matrix C (cf. Section 4.2). Since the adsorbate lattice can be measured directly in the image, the inverse of the epitaxy matrix can be applied to the PbPc lattice $\underline{C}^{-1}\underline{A} = \underline{S}$ in order to obtain an estimate of the substrate lattice $\underline{S}$ with respect to the PbPc lattice and hence where to expect substrate spots in the FFT. This works independently of a correct calibration of either the STM image scale or the reciprocal scale in LEEDLab because it is based merely on the epitaxy matrix' relative character. However, if the STM scanner is well-calibrated it is possible to state the correct calibration factor to be used in LEEDLab in order to obtain correct, absolute reciprocal distances (cf. Appendix A.III).

The PbPc on graphite case illustrates the most difficult example for the Fourier analysis.

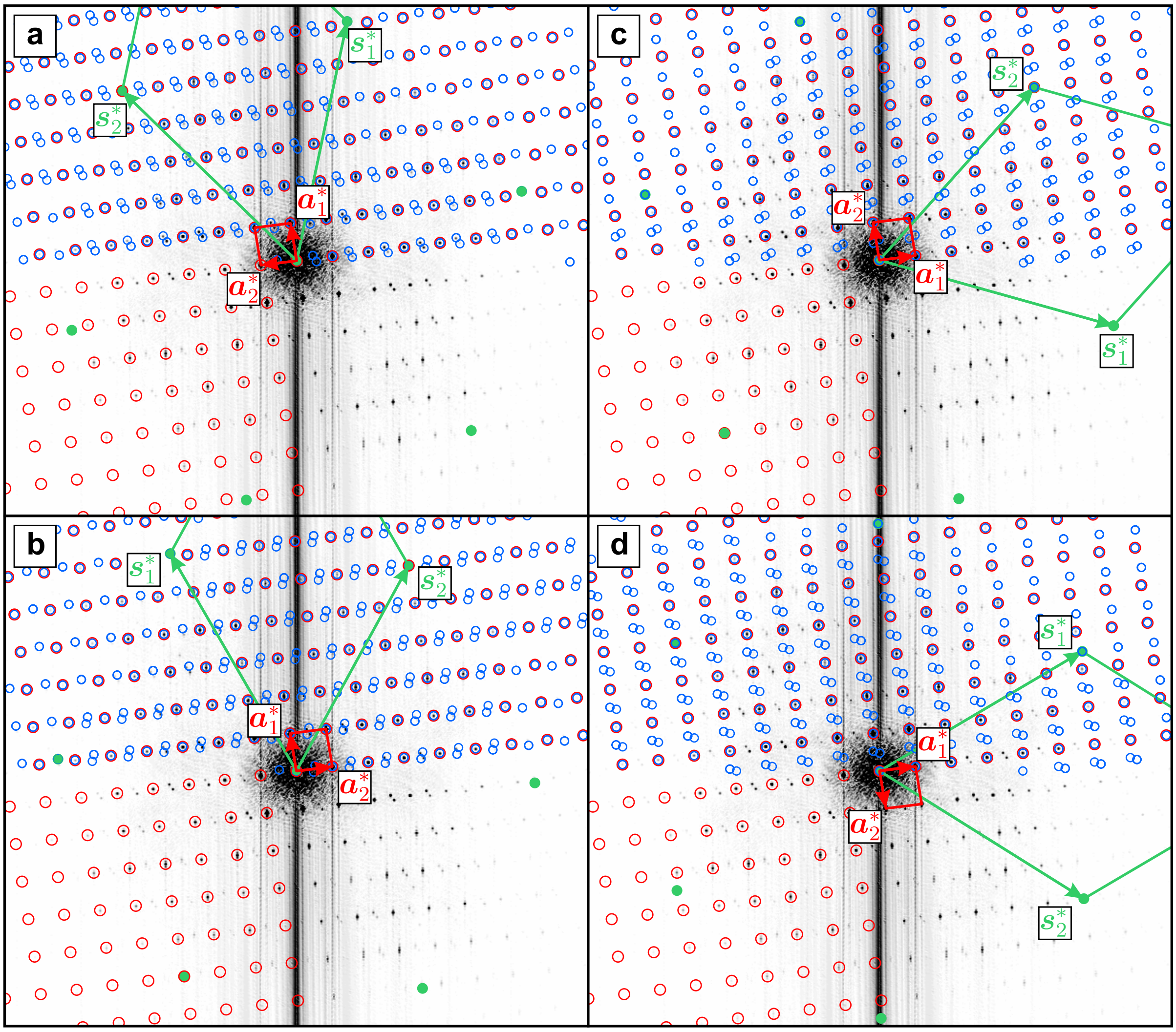

Figure 4.13: Inverted FFT of the STM image in Fig. 4.12a with four different definitions of the PbPc unit cell (red) and the substrate lattice (green) resulting from applying the inverse epitaxy matrix known from LEED to the PbPc unit cell vectors. The blue circles correspond to the convolution of the two lattices.

It features a unit cell that is almost but not exactly a square - it is neither rectangular nor equilateral. Hence, it is difficult to choose the unit cell vectors such that they are directly comparable with the structure measured in LEED. As mentioned above, STM images are always distorted to some degree, i.e., an obtuse-angled unit cell in the measured image, with $\boldsymbol{a}_1$ being the shorter vector in accordance with Table 4.1, might actually be acute-angled in a distortion-corrected version of the image. Applying the inverse epitaxy matrix of Table 4.1 to a wrongly defined PbPc lattice would obviously result in the wrong substrate lattice. Figure 4.13 shows the four possible definitions of the nearly square PbPc unit cell that describes the same observed PbPc spot pattern. Note that this includes right-handed and left-handed unit cells to also consider mirror domains with respect to the unit cell definition in Table 4.1.

Table 4.2: Epitaxy matrices of 1 ML PbPc on NG and corresponding lattice parameters (experimental uncertainties of the last significant digit in parentheses), with $\Gamma = \angle(\boldsymbol{a}_1, \boldsymbol{a}_2)$ and $\theta = \angle(\boldsymbol{a}_1, \boldsymbol{s}_1)$. The columns contain the LEED result from the center column of Table 4.1 and the fit results of the structures in Fig. 4.13a and Fig. 4.13b.

LEED result	Fig. 4.13a	Fig. 4.13b
$\begin{bmatrix} 6.085(7) & 5.000(5) \\ -2.464(7) & 4.000(5) \end{bmatrix}$	$\begin{bmatrix} 6.067(1) & 5.000(1) \\ -2.463(1) & 4.000(1) \end{bmatrix}$	$\begin{bmatrix} 6.068(1) & 5.000(1) \\ -2.540(1) & 4.000(1) \end{bmatrix}$
$\lvert\boldsymbol{a}_1\rvert = 13.84(7)$ Å	$\lvert\boldsymbol{a}_1\rvert = 13.81$ Å	$\lvert\boldsymbol{a}_1\rvert = 13.81$ Å
$\lvert\boldsymbol{a}_2\rvert = 13.91(7)$ Å	$\lvert\boldsymbol{a}_2\rvert = 13.90$ Å	$\lvert\boldsymbol{a}_2\rvert = 14.05$ Å
$\Gamma = 91.8(1)^\circ$	$\Gamma = 91.65^\circ$	$\Gamma = 92.14^\circ$
$\theta = 50.38(8)^\circ$	$\theta = 50.52^\circ$	$\theta = 50.51^\circ$

Although the same inverse matrix has been applied to each unit cell it obviously results in different patterns of additional convolution spots – and without fitting, Figs. 4.13c and 4.13d are not compatible with the FFT at all, while Fig. 4.13a represents the best description of the FFT pattern. Therein, the identification of the spots is not a problem and hence an epitaxy matrix can be fitted. It would not be useful here though to use the same LEEDLab function as in Sec. 4.2.1 which allows the adsorbate lattice to vary freely and the substrate lattice to only scale and rotate. The shear of the substrate makes it necessary to fit the epitaxy matrix while freely varying all adsorbate and substrate lattice parameters. Hence, a corresponding new fit routine was proposed for LEEDLab. Again, it has been kindly implemented by Falko Sojka (Institute for Solid State Physics, FSU Jena, Germany) as well. The result is an optimized epitaxy matrix that best describes the observed pattern of spots. Additionally, information on how to rectify the linear distortion of the STM image is included (see below).

The structure in Fig. 4.13a produces an epitaxy matrix in reasonable agreement with the one obtained via LEED analysis (cf. the center and left columns of Table 4.2, respectively). The fact that the margins of errors do not overlap might be due to the different temperatures during each measurement. While the sample used for the LEED measurement was only cooled to ≈ 130 K, the STM measurement was performed at 1.2 K. Even though there never was a sign of a structural change in LEED during cooling, a small deviation as implied by the above matrix cannot be ruled out – especially since structural changes due to cooling within a bilayer of PbPc on graphite have been suggested by others [138]. The given lattice parameters result from applying the fitted matrix to the undistorted known substrate lattice and hence do not possess an error margin directly from the fit.

Further, it has to be pointed out that, as is common for analyses in reciprocal space, the solution might not be unique, especially in a case with such similar unit cell vectors. The structure in Fig. 4.13b produces convoluted spots close to observed frequencies. If each convoluted diffraction order is assigned to the spot that lies closest to it, a subsequent fit results in an epitaxy matrix which also describes the FFT pattern reasonably well (cf. the right column in Table 4.2). However, this would imply a somewhat different shear of the image and a very different substrate orientation. Moreover, the epitaxy matrix differs significantly from that of Fig. 4.13a in one element. Of course, only one solution can be correct. In order to distinguish between meaningful solutions and others, more information about the image distortion or complementary structural data can be helpful. For example, a subsequent reversal of the slow scan direction or a scan within a frame rotated by 90° directly after the original one can help to identify the shorter unit cell vector and the obtuse unit cell angle.

Here, the identification of the shorter unit cell vector and the obtuse unit cell angle did not change with a subsequent scan with reversed slow scan axis (not shown, as basically identical to Fig. 4.12a). Therefore, Fig. 4.12a and the corresponding fit are the correct description of the structure. Additionally, a comparison with the LEED fit result implies that Fig. 4.12a indeed represents the correct solution. The very small error margins of the fit results originate from statistical deviations of determined spot positions from the simulated ones of the final fit result and do not account for potential systematic errors. Obviously, the fit describes the pattern with very small statistical error. However, the spot diameter in the FFT is very small compared to typical LEED spots, often only 2 to 4 pixels compared to 10 pixels or more. The peak-finding algorithm of LEEDLab, which fits 2D Gaussian functions to the spots, has very little information to mark the spot positions in that case. Therefore, if the intensities of many FFT spots are unfavorably distributed over the few pixels, i.e., if digitization errors are significant, small systematic errors are possible which are not within the error margins.

A final remark is concerned with the similarity of this approach to a real space Moiré pattern analysis. The Fourier-based analysis of Moiré patterns is related to the manual comparisons between the observed Moiré pattern and simulated ones [61], since it also relies on the size and shape of the Moiré pattern in relation to the adsorbate lattice. While it is convenient to count the number of unit cells that are included in the apparent Moiré period, the Moiré pattern is not necessarily periodic with the adsorbate lattice, i.e., non-commensurate, rendering the analysis subjective to some degree. On the other hand, fitting the positions of modulation frequencies can be regarded as objective if sufficient information for the spot identification is available.

A new way to correct STM distortions

While the correction of drift or any linear distortions in STM images is easy in the case of hexagonal or square lattices, it is difficult for arbitrary lattices if they are not known exactly. Previously, it may have been necessary to use complementary means such as LEED to calibrate such STM images and rectify distortions. However, if the STM images exhibit Moiré patterns due to a known substrate lattice, this can potentially be used for the correction without the need for an additional technique. If the spots due to the Moiré pattern provide enough information to locate two linearly independent substrate lattice vectors, the epitaxy matrix can be fitted. As a side product, the LEEDlab fit routine that allows for a shearing of the substrate lattice produces the substrate unit cell vectors $\underline{S}_{\text{sheared}}$ in Cartesian coordinates. Based on the desired (known) substrate vector matrix $\underline{S}$ a transformation matrix $\underline{M} = \left(\left(\underline{S}_{\text{sheared}} \right)^{-1} \underline{S} \right)^{\top}$ can be calculated and used to rectify the distortion by linear transformation. Such a matrix would transform a vector from the sheared to the correct image: $\underline{M} \boldsymbol{v}^{\text{sheared}} = \boldsymbol{v}$.

5 Epitaxial ordering of an incommensurate organic layer

In this chapter, many of the previously discussed topics will be applied to the case of a hexa-*peri*-hexabenzocoronene (HBC) monolayer on graphite. This system has been studied before, always with the conclusion of commensurate growth [30, 31, 139, 140]. Since the structure and symmetry of this “nanographene” molecule can be likened to a small sheet of graphene, the commensurate growth seemed like a natural consequence. Moreover, other aromatic hydrocarbons with the same D_{6h} symmetry, namely coronene and benzene, likewise have been reported previously as commensurate on graphite [139, 141]. Some authors reasoned that the molecular orientation is likely determined exclusively by the underlying graphite lattice, with the respective honeycomb structures being aligned like sheets of graphite [31].

It shall be shown in the following that a HBC monolayer is in fact not commensurate with graphite (both with EG and NG) and, more importantly, serves as a comprehensive prove of the epitaxy mechanism of orientational epitaxy described by Novaco and McTague (cf. Sec. 3.2.1). Parts of the results in this chapter have been published previously in a collaborative study [P9]. The HBC molecules were synthesized and provided by Prof. Dr. Klaus Müllen and Prof. Dr. Xinliang Feng (both at that time: Max Planck Institute for Polymer Research, Mainz, Germany). Falko Sojka (Institute for Solid State Physics, FSU Jena, Germany) helped with the analysis of LEED and STM measurements, especially by adapting code of the LEEDLab software to facilitate some of the non-standard fit procedures to obtain epitaxy matrices from LEED and STM images with the convolution approach and to use the same software for automatically locating molecules in an STM image. Dr. Lars Matthes (at that time: Institute of Condensed Matter Theory and Solid State Optics, FSU Jena, Germany) performed DFT calculations needed to model interaction energies of HBC on graphite. For technical details on the DFT calculations the reader is referred to Publication [P9]. In this chapter, the focus will be on how DFT data can be used to model a monolayer of HBC on graphite. Prof. Dr. Stefan Mannsfeld provided software to perform potential energy calculations based on force-field methods.

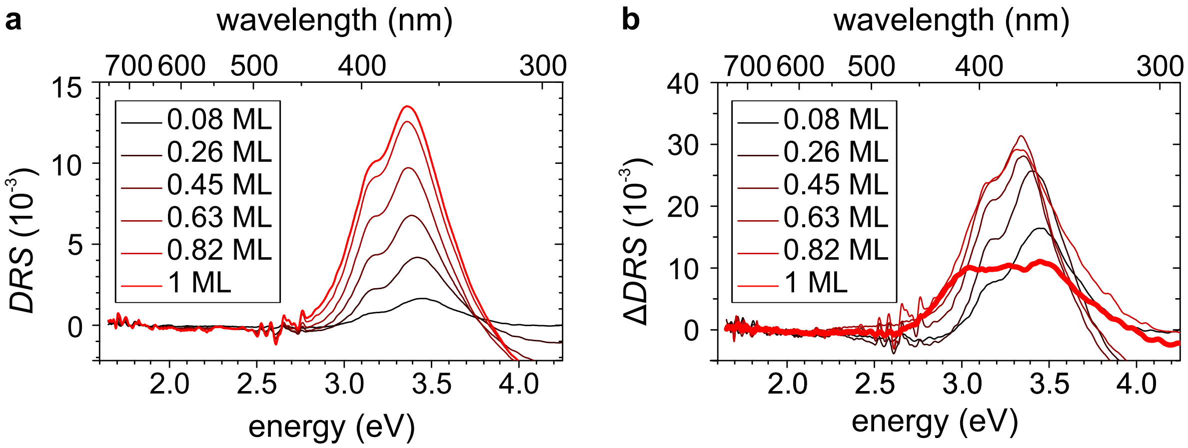

Figure 5.1: **a**: *DRS* of ≈1 ML HBC on EG. **b**: Corresponding ΔDRS spectra. The layer thickness is estimated based on the spectral change upon the start of the second monolayer (thick red line in panel **b**) and given with 2 decimals to avoid large rounding errors.

5.1 Sample preparation

HBC-on-graphite samples were prepared in chambers A and B, with thickness control facilitated via DRS as described in Chap. 2 with a xenon lamp as light source. Both NG and EG were used as substrates, depending their suitability for the respective experiment (see below), and were kept at room temperature during the deposition. Figure 5.1 shows *DRS* and ΔDRS spectra, drift-corrected in the low energy range, of an exemplary measurement during the deposition of HBC on EG. The deposition rate in the chosen example is about 40 % faster than the one used to prepare the samples discussed below. However, the good signal-to-noise ratio renders it an illustrative example for the thickness control. The accumulated spectra in Fig. 5.1a reveal a strong signal between 3 eV and 3.75 eV due to a molecular absorption band in that range [142]. It increases nearly linearly over time, corresponding to a film thickness increase in equal steps. However, in the last spectrum, the signal growth slows promptly, indicating a change in the optical properties of the layer due to the start of molecules stacking on top of each other. This can be recognized much better in the ΔDRS in Fig. 5.1b where the spectral shape changes abruptly from one spectrum to the next. In all measurements discussed in the following, the deposition was stopped immediately when this change appeared. STM measurements discussed in the next section indeed reveal that the sample coverage is slightly more than 1 ML under these circumstances. Hence, the layer thickness is determined with respect to this spectrum. Typical values of deposition rates used for the following samples are 0.1 ML/min, with 30 s between subsequent accumulated spectra. Since it sometimes takes two consecutive ΔDRS spectra to validate a spectral change, the nominal layer thicknesses can be conservatively estimated to be 1.1 ± 0.1 ML and will be referred to as 1 ML in the following.

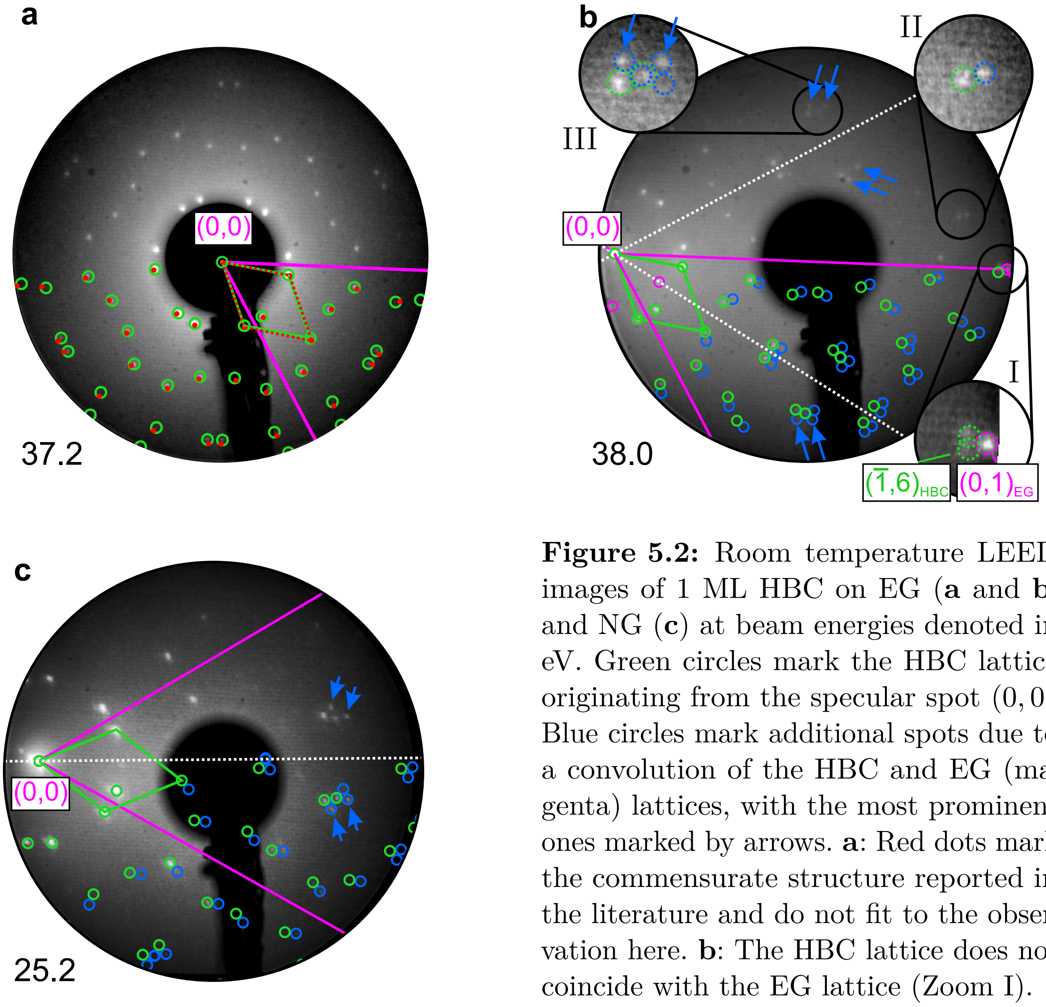

Figure 5.2: Room temperature LEED images of 1 ML HBC on EG (**a** and **b**) and NG (**c**) at beam energies denoted in eV. Green circles mark the HBC lattice originating from the specular spot $(0,0)$. Blue circles mark additional spots due to a convolution of the HBC and EG (magenta) lattices, with the most prominent ones marked by arrows. **a**: Red dots mark the commensurate structure reported in the literature and do not fit to the observation here. **b**: The HBC lattice does not coincide with the EG lattice (Zoom I).

5.2 Epitaxial relation of hexa-*peri*-hexabenzocoronene on graphite

LEED measurements

The epitaxy of HBC on graphite can most easily be examined with LEED. Figure 5.2 shows LEED images of a monolayer of HBC on EG and NG at room temperature. The pattern of HBC spots originating from the specular spot (green circles) constitute a hexagonal HBC lattice similar to measurements in the literature [139], based on which a commensurate HBC layer was concluded therein. Indeed, in the image of the non-tilted sample in Fig. 5.2a, there is no obvious indication of a non-commensurate epitaxy type in form of additional (convoluted) spots. The deviation from the reported commensurate structure is very small which is illustrated by an additional overlay of the commensurate lattice (red dots). However, in Fig. 5.2b, the sample is tilted by 15° and a beam energy was chosen such that both the specular spot $(0,0)$ near the left screen edge and a first diffraction order of graphite near the right edge are visible. With the tilt distortion having

Table 5.1: HBC on graphite epitaxy matrices and lattice parameters at room temperature (RT) and low temperature (LT), obtained with LEED and STM, respectively. The matrix in the right column is equivalent to the reported commensurate structure [139]. Γ is the unit cell opening angle enclosed by $\boldsymbol{a}_1$ and $\boldsymbol{a}_2$ and θ is the unit cell orientation angle enclosed by $\boldsymbol{a}_1$ and $\boldsymbol{s}_1$. Experimental uncertainties of the last significant digit are given in parentheses.

RT (300 K)	LT (1.2 K)	commensurate
$\begin{bmatrix} 5.147(5) & -0.969(4) \\ 0.969(4) & 6.116(5) \end{bmatrix}$	$\begin{bmatrix} 5.113(5) & -0.986(1) \\ 0.985(1) & 6.092(6) \end{bmatrix}$	$\begin{bmatrix} 5 & -1 \\ 1 & 6 \end{bmatrix}$
$a_{1/2} = 14.01(8)$ Å	$a_{1/2} = 13.95(2)$ Å	$a_{1/2} = 13.70$ Å
$\Gamma = 120.00(5)^\circ$	$\Gamma = 120.00(3)^\circ$	$\Gamma = 120^\circ$
$\theta = -8.48(4)^\circ$	$\theta = -8.66(2)^\circ$	$\theta = -8.95^\circ$

been corrected, the image reveals that the $(\bar{1}, 6)$ diffraction order of HBC and its equivalents do not coincide with the nearby first-order reflection of EG (cf. Zoom I in Fig. 5.2b). Commensurate epitaxy, as it was reported in the literature, can therefore be excluded. Moreover, spots appear which cannot be explained with the green lattice originating from $(0, 0)$. The additional spots in the vicinity of $(0, 0)$ arise from the $6\sqrt{3} \times 6\sqrt{3} - 30^\circ$ reconstruction of the underlying EG with respect to the SiC substrate, as described in Sec. 4.2.2. Therefore, they are depicted in the same color as the EG substrate lattice. A number of other spots mostly in the right half of the image can be explained with the approach of Sec. 4.2.1, convoluting the green HBC lattice with the substrate lattice (cf. Zooms II and III in Fig. 5.2b). Those spots are observable in a broad energy range of at least $\approx 20 \ldots 60$ eV, but are never observed close to the specular spot. Hence, based on the non-commensurability and the discussion in Sec. 4.1.3 about the sensitivity of LEED with respect to lateral and perpendicular modulations, it can be expected that HBC layer features a significant lateral modulation due to the underlying graphene lattice. On NG, the same spot patterns are observed and there is no notable difference concerning the epitaxial relation. Hence, even though EG features a surface reconstruction, the HBC molecules arrange just like on natural graphite and EG can be regarded as graphite in that respect, in agreement with a study on another molecule adsorbed on the same substrates [P1]. However, LEED measurements on EG exhibit a better diffraction quality compared to the buckled natural graphite, which is why a quantitative LEED analysis is described next using the EG sample.

Applying the geometric convolution approach in order to fit the epitaxy matrix, one obtains from the image in Fig. 5.2b the result in the first column of Tab. 5.1, referred to as the room-temperature (RT) structure in the following. While describing a perfectly hexagonal unit cell within the margin of error, it deviates slightly, but significantly, from the matrix with strictly integer elements corresponding to the reported commensurate structure (cf. right column of Tab. 5.1). The deviation translates into a value for the lattice constant that is larger and an absolute value of the unit cell orientation θ that is smaller than the respective commensurate values. Moreover, since the lattice is hexagonal like that of the underlying substrate, there is no possibility that the two structures can constitute a point-on-line (POL) or line-on-line (LOL) epitaxy type. Both types require a coincidence of reciprocal adsorbate and substrate lattice points in only a single direction. However, due to the same sixfold rotational symmetry of HBC and graphite, any coincidence would repeat at multiples of 60°. Such coincidences in different directions are only possible with either commensurate (ruled out already) or higher-order commensurate (HOC) growth. HOC epitaxy produces epitaxy matrices containing only rational numbers. However, the measurement, as any experimental determination of an epitaxy matrix, contains a finite margin of error. Hence, at this point, lattice epitaxy in form of the HOC type cannot be ruled out yet. This requires a discussion of the layer's energetic characteristics which will follow in the next section.

The non-commensurability of the HBC LEED pattern is not obvious if the faint features discussed above are overlooked and a lattice simulation is compared manually to the measurement. Hence, it is possible that the convoluted spots originating from a first order substrate spot are mistaken as ones originating from the specular spot due to the relatively small differences in the spot positions. The presented system should therefore serve as an example that the ability to fit lattices to many LEED spots at the same time in distortion-corrected images may be crucial. In fact, the non-commensurability can already be inferred from fitting the pattern in Fig. 5.2a, without the convolution approach. The matrix is equivalent to the one given in Tab. 5.1, with an additional scaling uncertainty due to the lack of convoluted spots, and is therefore not shown separately.

STM measurements

In order to obtain information about the molecular packing in real space, STM measurements were performed on 1 ML of HBC on NG at low temperatures in chamber A. NG was chosen over EG in this case because HBC is likewise not commensurate with it and the absence of a surface reconstruction in the images renders an analysis easier. At small scan ranges and negative sample bias (cf. Fig. 5.3) the HBC molecules are imaged with sub-molecular resolution. The contrast can be predominantly attributed to the highest occupied molecular orbital (HOMO) of HBC which is depicted in the inset of Fig. 5.3b and was determined by Lars Matthes via DFT. The molecules lie flat or almost flat on the surface. Deviations from a perfect D_{6h} symmetry are most likely tip-induced, as can be inferred from varying contrasts in Fig. 5.3a. Since HBC features a hexagonal lattice on the hexagonal graphite, rotationally equivalent domains are identical to each other. Hence,

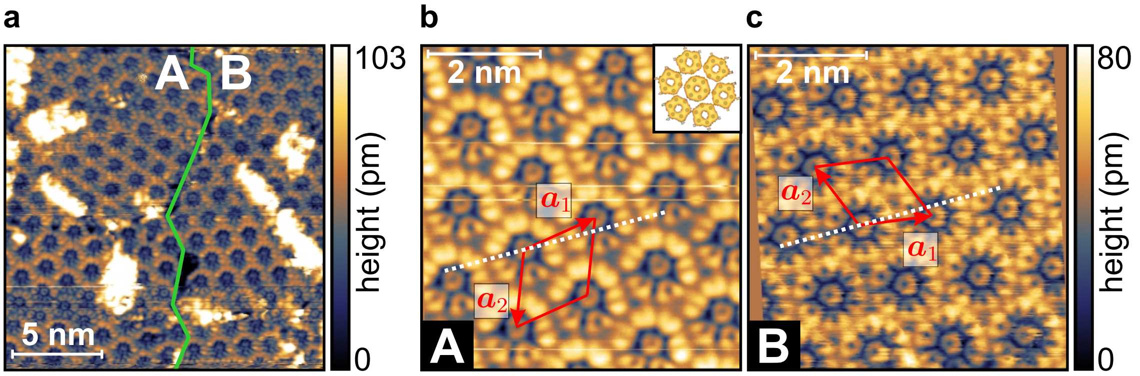

Figure 5.3: Small-scale STM images of 1 ML HBC on NG, at 4.4 K, -3 V, and 3 pA in all cases. **a**: Boundary between the two possible mirror domains, one on the left-hand side (A) and one on the right-hand side (B) of the image. Panels **b** and **c** show close-ups of each domain with sub-molecular resolution. Both images were corrected for a linear distortion based on the hexagonal lattice determined via LEED. The combination of these images with LEED data allows for determination of the molecular orientation within the unit cell (marked in red, see text for details). The inset in panel **b** depicts the HOMO of HBC.

there are only two possible mirror domains and both are observable in the same image in Fig. 5.3a. This information is very helpful to determine the molecular orientation within the HBC unit cell and with respect to the substrate lattice (see Fig. 5.4a for an illustration of the angles). Since the unit cell orientation $\theta = \angle(\boldsymbol{a}_1, \boldsymbol{s}_1) = -8.48(4)^\circ$, measured from $\boldsymbol{s}_1$, is known from LEED[m] there is only one possible orientation of $\boldsymbol{s}_1$, depicted as a dotted line in Figs. 5.3b and 5.3c, that encloses the angle $|\theta|$ with $\boldsymbol{a}_1$ of both mirror domains. By determining the molecular orientation β with respect to $\boldsymbol{a}_1$, one therefore obtains the angle $\alpha = \beta + \theta$ as well, measured from $\boldsymbol{s}_1$.

For this, circular line profiles were extracted along the outmost benzene rings of all fully imaged molecules in Fig. 5.3b and Fig. 5.3c using ImageJ with the Oval Profile Plot plugin [143] (cf. Fig. 5.4b). Due to the symmetry of HBC the nodes along the full circle should be separated by steps of 30°, at least on average. Hence, by averaging the curves and determining the position of every minimum, the angular position and hence the molecular orientation can be fitted with a linear regression of multiples of 30°. The orientation of the lattice vector $\boldsymbol{a}_1$ is obtained directly by averaging over several nearest-neighbor distances. With this, the molecular orientation with respect to $\boldsymbol{a}_1$ can be determined to be $\beta = 5.1(5)^\circ$.

Large-scale STM measurements (cf. Fig. 5.5a) reveal molecularly resolved domains that are hundreds of nanometers wide, proving that the observed HBC growth mode is not merely a finite-size effect. In such images, the molecular centers appear dark at positive

---

[m] As will be shown next, the HBC structure slightly changes upon cooling. However, those changes are below the error margin of the molecular-angle determination and do not influence the result.

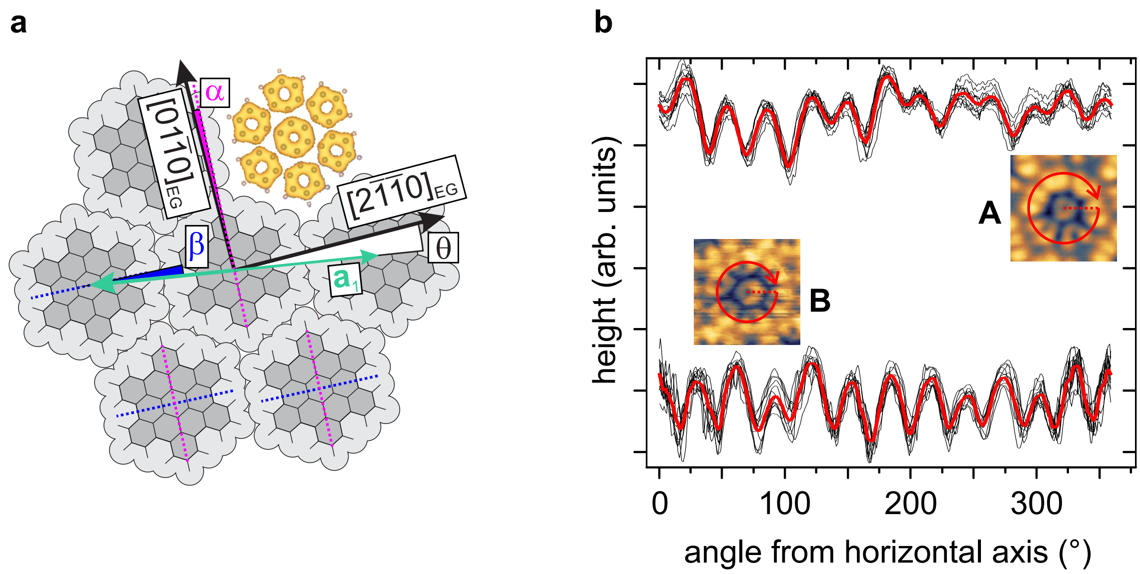

Figure 5.4: **a**: Molecular orientation angles determined via STM and LEED measurements. The orientation and handedness of the figure correspond to domain B and the data in Tab. 5.1. One molecule depicts the HOMO of HBC. **b**: Angular profiles (black) and their averages (red) around 12 molecules in Fig. 5.3b (top curve; domain A) and 13 molecules in Fig. 5.3c (bottom curve; domain B). Adapted from [36].

sample bias. Additionally, a two-dimensional Moiré pattern consisting of triangles becomes visible, with most of them revealing a slight chirality (cf. contrast-enhanced right-hand side of Fig. 5.5a). This further confirms in real space that the HBC layer is indeed not commensurate since the adsorption sites of the molecules vary over a long distance. Even though the Moiré pattern is locally disturbed by some bright point defects mostly at the triangles' corners, it is rather regular over the entire image[n]. Moreover, it produces sharp spots in a fast Fourier transform (FFT) of the STM image (cf. Fig. 5.5b) and therefore allows for a convolution-based determination of the epitaxy matrix as described in Sec. 4.3.

The spots marked with red circles correspond to the HBC lattice which can be fitted directly using LEEDLab. By applying the inverse of the epitaxy matrix determined via LEED at room temperature to this lattice $\underline{C}^{-1}\underline{A} = \underline{S}$, an approximate position of the reciprocal substrate lattice can be derived, which in turn provides the positions of convoluted spots (blue circles). In the presented case, those estimated positions are very close to the actually observable spots, implying that the structure changed very little upon cooling and allowing for an easy fit of the epitaxy matrix. The result is referred to as the LT structure in Tab. 5.1. If applied to the undistorted graphite lattice, it reveals a slightly smaller lattice constant and larger angle $|\theta|$ compared to the RT structure. The corresponding values are

---

[n] The defects are too small to be HBC molecules and presumably are rest gas molecules adsorbed at prone sites during the pre-cooling phase (≈ 80 K), prior to the sample insertion into the STM stage.

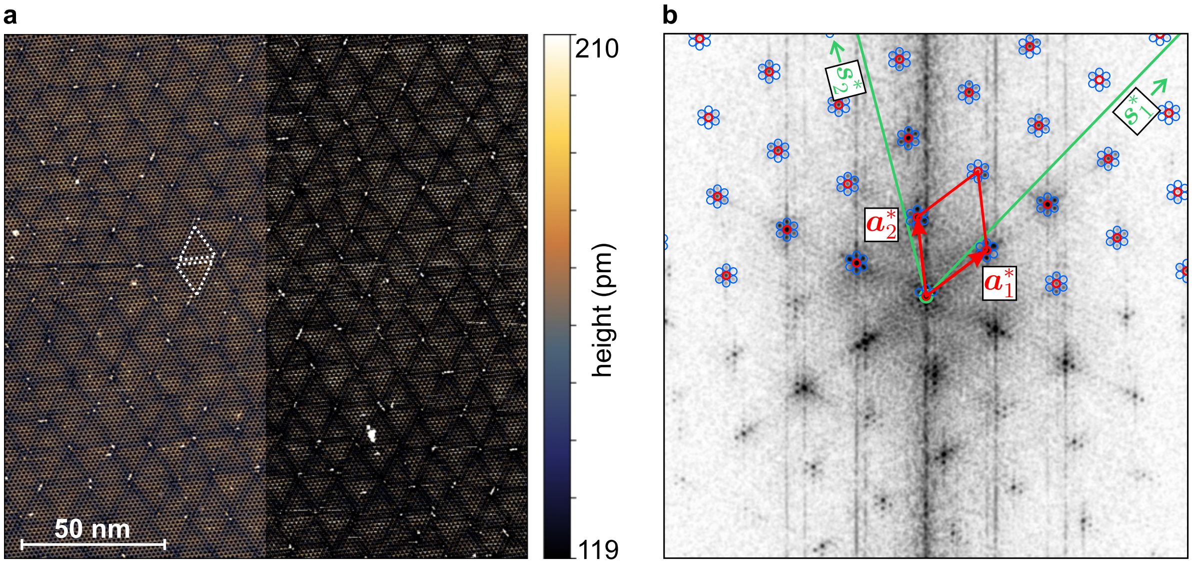

Figure 5.5: **a**: Large-scale STM image of 1 ML HBC on NG, at 1.2 K, +3 V, and 2 pA. A long-range Moiré pattern is visible, especially in the strongly constrast-enhanced right-hand side, and marked with white triangles as guide to the eye. **b**: FFT of the image in panel **a**, featuring spots due to the HBC lattice (red circles) and satellites (blue circles) describable via a convolution with the substrate lattice (in the direction of the green lines).

given in Tab. 5.1 as well. Due to the relative character of the epitaxy matrix, the decrease in the lattice constant is relative to graphite as well. However, the lattice constant of graphite has been determined to hardly change with decreasing temperature [144], likely rendering the decrease in the lattice constant at low temperatures absolute.

In combination with the analysis of the small-scale images in Fig. 5.3 the molecular orientation with respect to the substrate can be given for the LT structure as $\alpha = \beta + \theta = -3.6(5)^\circ$, measured from the substrate $[01\bar{1}0]$ direction (cf. Fig. 5.4a). The angle α is defined such that $\alpha = 0^\circ$ corresponds to an alignment of the HBC honeycomb structure with that of the substrate, as suggested in Ref. [31]. However, the molecules are apparently rotated away from such a configuration.

5.3 Exclusion of lattice epitaxy

In the previous section, three types of lattice epitaxy could already be excluded as an explanation for the orientation of the HBC monolayer with respect to graphite. The HOC type, however, relies on the epitaxy matrix elements being all rational and not irrational which is not possible to determine experimentally. Yet, it can be shown that the LT structure determined above with high precision does not experience any meaningful

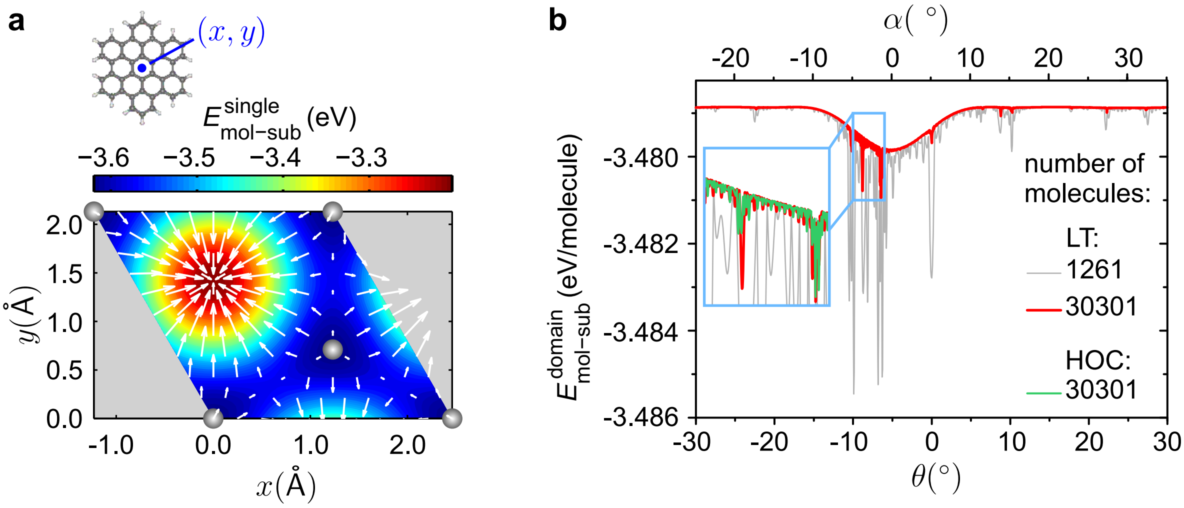

Figure 5.6: **a**: Map of $E^{\text{single}}_{\text{mol-sub}}(\boldsymbol{r}, \alpha)$ for the center position (x, y) of a single HBC molecule with orientation $\alpha = 0°$, i.e., with its honeycomb aligned to that of the substrate, over one graphite unit cell. It has been scaled to match DFT values (see text for details). Carbon atoms of the top graphite layer are depicted and mark points with low-energy AB stacking of HBC on graphite. White arrows depict the gradient (cf. Appendix A.IV) **b**: Domain energies $E^{\text{domain}}_{\text{mol-sub}}$ per molecule of *unmodulated* HBC domains with the LT structure and a similar structure producing a HOC coincidence at $\theta = -8.57°$ (only within zoom), rotated over graphite. The energy varies only within a range of < 2 meV per molecule for the larger domains and neither the LT nor the HOC structure produce a meaningful epitaxial energy minimum.

epitaxial energy minimum if its structure is assumed unmodulated with strict translational symmetry, even if HOC coincidence is enforced.

For this, force-field calculations using the grid technique of the software *POWERGRID* [36,70] are performed. Therein, assuming only additive two-body interactions at zero Kelvin and using the Merck molecular force field (mmff94) [145], the interaction of one flat-lying HBC molecule with a large circular domain ($\varnothing = 80$ Å) of two layers of graphite in bernal (AB) stacking is calculated via summing up pairwise atomic interaction potentials. The resulting potential energy $E^{\text{single}}_{\text{mol-sub}}(\boldsymbol{r}, \alpha)$ is mapped over one substrate unit cell for different orientation angles α of the molecule[o,p] with respect to the substrate (cf. Fig. 5.6a). The lateral mapping resolution is 51×51 points, and the angular resolution is 0.1°, allowing for a linear interpolation of the data. Additionally, for each configuration the adsorption height is optimized. It is approximately directly proportional to $E^{\text{single}}_{\text{mol-sub}}(\boldsymbol{r}, \alpha)$ and resembles the map in Fig. 5.6a, in accordance to an assumption made at the end of Sec. 4.1.3, and is therefore not shown separately.

---

[o] To emphasize that the adsorbate consists of molecules, the index “mol-sub” is used from here.

[p] Since DFT results from Dr. Matthes were available, the DFT-optimized structure of HBC was used in the force-field calculations as well.

A different approach used for inorganic layers expands $E^{\mathrm{single}}_{\mathrm{mol-sub}}$ in a Fourier series as in Equ. 3.9, based on only the first few important Fourier coefficients [146]. However, it loses its advantage here and is not applied since $E^{\mathrm{single}}_{\mathrm{mol-sub}}(\boldsymbol{r}, \alpha)$ depends strongly on the molecular orientation α due to the more complex shape of the molecule compared to an atom – the coefficients would have to be recalculated for each α. On the other hand, it is known that the corrugation of force-field energy maps on graphite is strongly underestimated, with the one from DFT calculations being larger by a factor of more than 10 [147]. For these reasons, the $E^{\mathrm{single}}_{\mathrm{mol-sub}}(\boldsymbol{r}, \alpha)$ maps are obtained via *POWERGRID* as described, but scaled based on selected DFT calculations of a single HBC molecule on a bilayer of graphite. Due to the periodic boundary conditions of DFT a large 8 x 8 supercell of graphite was used to obtain the single-molecule values. The $E^{\mathrm{single}}_{\mathrm{mol-sub}}$ maps with the largest corrugation in both methods, force-field and DFT, at $\alpha = 0°$ are matched by correcting the offset and scaling of the force-field map. These corrections are then applied to the maps of all other angles α. The lowest-energy configuration with an effective AB stacking between the HBC internal structure and the top graphite layer corresponds to an adsorption energy of -3.62 eV, the maximum energy in the AA stacking configuration is -3.20 eV, and the scaling factor is 14.6, in agreement with Ref. [147]. The minimum and maximum values for the adsorption height based on the DFT calculations are 3.32 Å (AB stacking) and 3.46 Å (AA stacking), respectively. The resulting map has been cross-checked with exemplary, additional DFT calculations within the same map and for other angles α (not shown, see Publication [P9] for details). They are in good agreement, rendering the scaling approach useful.

With this, the domain energy $E^{\mathrm{domain}}_{\mathrm{mol-sub}}(\theta)$ of an unmodulated HBC domain can be calculated in dependence of the unit cell orientation θ, with the experimental parameters of the LT structure, i.e., a lattice constant of 13.95 Å and an angle $\beta = 5.1°$. Hence, when the domain is rotated over the substrate the molecular orientation β within the HBC unit cell is kept fixed at the value obtained experimentally, while the molecular orientation $\alpha = \theta + \beta$ with respect to the substrate changes. Importantly, the lateral registry of the entire domain with respect to the substrate is optimized within one graphite unit cell in each step. Otherwise, physically not meaningful maxima would occur [63]. The results are shown for two domains of different sizes in Fig. 5.6b. While the red and gray curves show a number of sharp minima, including some around the experimentally determined $\theta = -8.66(2)°$, the depths of the minima are insignificant. Moreover, the positions and depths of the minima depend strongly on the domain size, in contrast to cases of lattice epitaxy where the minima are increasingly well-determined in both angular position and depth with increasing domain sizes [70]. Here, however, the lack of any significant coincidences between the reciprocal HBC and graphite lattices leads to an increasing number of different adsorption sites with increasing domain size which suppresses the sharp minima. Within the unmodulated, and strictly periodic lattice concept, there is therefore no explanation for the experimentally determined LT structure. The same is true for the RT structure, which, however, shall not be discussed here (see Publication [P9] for more details in that regard).

To emphasize that this result does not depend on a deliberate avoidance of any exact HOC configuration, the calculation was repeated with a lattice constant of 13.9552 Å which would result in a HOC coincidence of the extremely high $(h, k) = (39, 20)$ diffraction order of HBC with the $(m, n) = (8, 2)$ order of graphite at $\theta = -8.57°$. This would be close to the experimental value of -8.66(2), even though outside of the error margin, and produce a long-range Moiré pattern similar to the one seen in Fig. 5.5a. However, this structure results in almost the same insignificant energy minima as the LT structure, which is why the energy curve is only shown in the small zoom inset of Fig. 5.6b.

A small feature, which is present for all domain sizes though, is the very broad minimum around $\theta \approx -5°$. Through different simulations it was realized that this minimum always appears at $\theta = -\beta$, i.e., when the molecular honeycomb structure is aligned with the substrate's one at $\alpha = 0°$. Since this feature appears with and without coincidence lattices for all domain sizes, the incommensurate energy E_0 from Equ. 3.9 must depend on α. Indeed, it was mentioned above that the Fourier coefficients of $E^{\text{single}}_{\text{mol}-\text{sub}}(\boldsymbol{r}, \alpha)$ depend on α, and E_0 is simply the first Fourier coefficient of the series. This has not been reported before, and in principle, it would allow an infinite (unmodulated) HBC domain without any other epitaxial energy minima to prefer the angle $\theta = -\beta$. However, the high precision of the above structure analysis clearly excludes this possibility for the presented case as well, since $\theta = -8.66(2)°$ in the case of the LT structure.

In summary, all types of (unmodulated) lattice epitaxy can be excluded as an explanation for the orientation of a HBC monolayer on graphite and other mechanisms must be at play. Therefore, a monolayer HBC on graphite can safely be regarded as incommensurate. In order to determine whether the Novaco-McTague mechanism of orientational epitaxy can explain the overlayer orientation, STM images are analyzed next with respect to the static distortion waves (SDWs) this mechanism relies on.

5.4 Measuring static distortion waves

While the observation of Moiré patterns in STM images is very common, the presence of a brightness modulation itself is not a proof for a displacive modulation of the surface crystal, as it might represent a modulated local density of states. Moreover, even if a displacive modulation perpendicular to the surface can be confirmed, this alone cannot

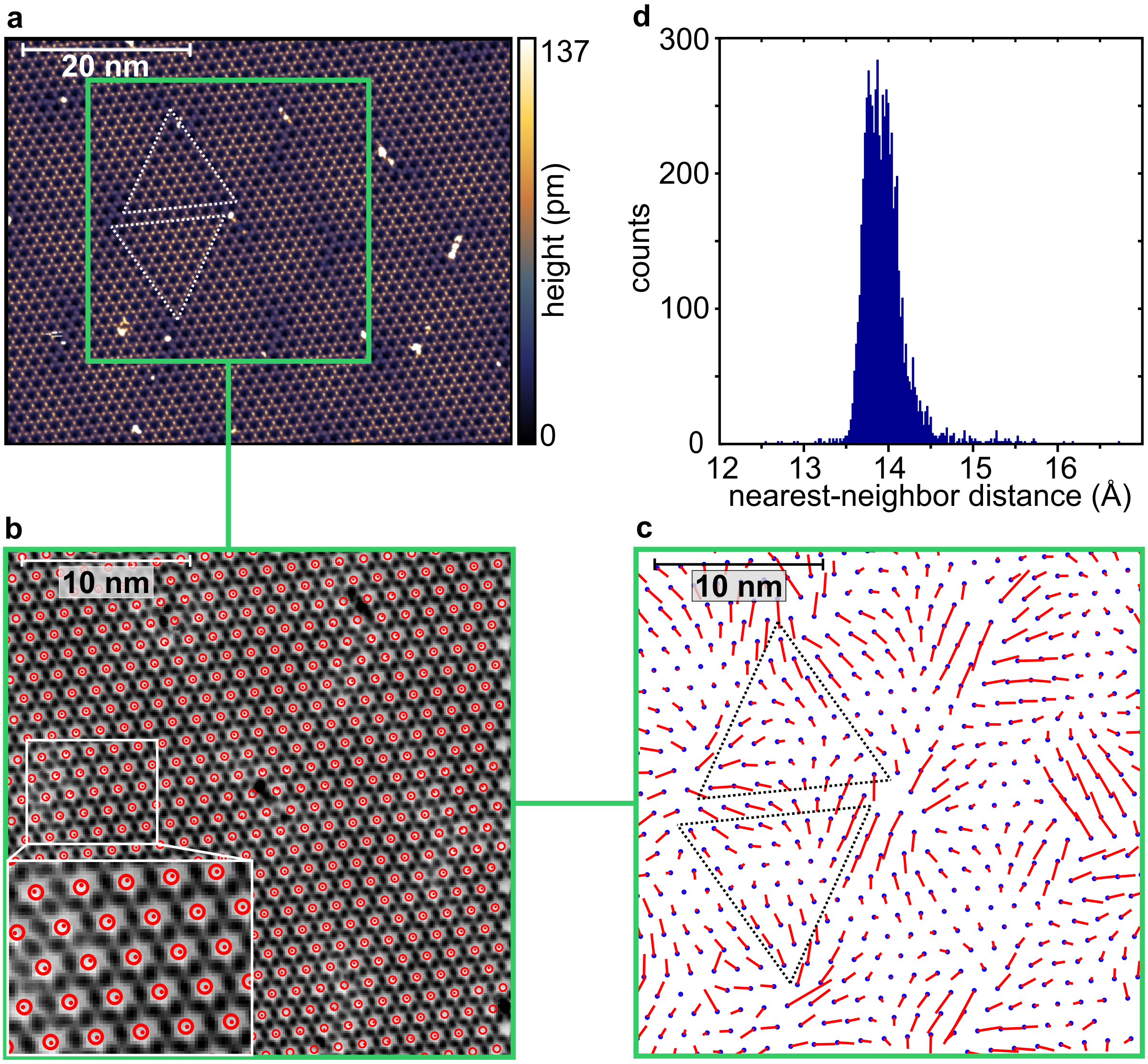

Figure 5.7: **a**: STM image of 1 ML HBC on graphite showing again the Moiré pattern marked by the triangles, at 1.2 K, +3 V, and 2 pA. Molecular centers are dark. **b**: Contrast-inverted zoom (marked in green) of panel **a**. Found molecular positions are marked with small dots, a (reference) lattice fitted to these positions is marked with circles. **c**: Reference lattice (dots) and molecular displacements from it (red lines, magnified by a factor of 15), determined from **b**. **d**: Histogram of nearest-neighbor distances within the green frames.

explain the relative orientation of structures [72, 85]. However, lateral displacements in the form of static distortion waves (SDWs) were proposed by Novaco and McTague to solve the mystery of incommensurate yet epitaxial films.

In order to determine whether this effect is present in a monolayer of HBC on graphite, large-scale STM images with still sufficient resolution such as in Fig. 5.7a are analyzed using the peak-finding algorithm of LEEDLab. By fitting 2D Gaussian functions to intensity distributions, it allows for the determination of the centers of sufficiently Gaussian-like distributions with sub-pixel resolution [P2]. In the contrast-inverted image in Fig. 5.7b the symmetry of each molecular center is sufficient for the algorithm to reliably locate each molecule (cf. red dots in Fig. 5.7b). A smaller area close to the center of the original image was chosen to avoid the non-linear distortions discussed above. Therefore, in the second step a lattice can be fitted that best describes all of those found positions and will be referred to as reference lattice (cf. red circles in Fig. 5.7b).

Differences between the found positions and the reference lattice are hardly visible in Fig. 5.7b. However, their magnified versions in Fig. 5.7c are clearly not random. Even though the molecular positions are somewhat disturbed by the bright point defects, the distribution of the molecular displacements resembles a smooth vector field as would be expected for SDWs: the displacements approximately follow the Moiré triangle edges and generally point away from the triangles' corners. The average displacement is only 0.52 Å while the resulting distribution of nearest-neighbor HBC bond lengths has a standard deviation of 0.28 Å (see Fig. 5.7d for the corresponding histogram). This amounts to only 3.7 % and 2 %, respectively, of the average nearest-neighbor distance of 13.95 Å. In order to obtain the histogram and these numbers from the data, it was necessary to correct for a small linear distortion in the image. A molecule in the hexagonal lattice has nearest neighbors in three independent directions. In general, a shear of the image distorts these directions unequally and results in a broadened histogram. While the correction could have been performed on the image itself before the fitting, it is tantamount to transform the fitted lattice into the hexagonal one given in Tab. 5.1.

Hence, in agreement with implications of the LEED data at room temperature in Sec. 5.2, a significant lateral modulation is present within the HBC layer at low temperatures. Importantly, neither the Moiré pattern nor the pattern of displacements implies the presence of a periodic supercell or an assembly of many commensurate patches separated by incommensurate domain walls. Rather, they may be interpreted as a continuous domain of HBC molecules whose positions are modulated with respect to an incommensurate reference lattice. The incommensurability was already reasoned based on the discussion of periodic lattice models which did not produce any sizable epitaxial energy minimum even in the case of a HOC coincidence similar to the experimentally determined structure. As will be shown next, the insignificance of a HOC coincidence is retained if local displacements are allowed, and the HBC layer represents a true case of Novaco's and McTague's orientational epitaxy.

5.5 Calculation of local relaxation in organic layers

In order to verify that the measured distortions indeed represent SDWs in an incommensurate layer and that the SDWs decisively minimize the system's total energy, a model is introduced to simulate the spatial relaxation of each molecule away from exact lattice points for realistically large domains of thousands of molecules. The approach is based on a self-consistent iterative determination of the total force $-\nabla E_{\mathrm{total}}^{\mathrm{domain}}$ experienced by each molecule due to gradients in the total energy landscape and moving a molecule a small step in the corresponding direction, before re-evaluating the energy gradients again. These forces generally change in every iteration step due to the varying molecular registry with the substrate and the varying positions of each molecule's nearest neighbors. Since the intermolecular interaction is short-range, neighbors further away can be neglected. Hence, the displacement $\boldsymbol{u}_p^{(s)}$ of molecule p in iteration step s, and those of its nearest neighbors $\{\boldsymbol{u}_q^{(s)}\}$ are used to refine the displacements in the next iteration step $s+1$ by evaluating the resulting change of gradients:

$$\boldsymbol{u}_p^{(s+1)} = \boldsymbol{u}_p^{(s)} - \tau \nabla E_{\mathrm{total}}^{\mathrm{domain}}(\boldsymbol{u}_p^{(s)}, \boldsymbol{u}_q^{(s)}) \tag{5.1}$$

The step size τ needs to be small enough for a stable convergence of the relaxation, but is otherwise not a critical parameter and is kept constant.

The DFT-based potential energy maps $E_{\mathrm{mol-sub}}^{\mathrm{single}}(\boldsymbol{r}, \alpha)$, or rather the corresponding gradients $\nabla E_{\mathrm{mol-sub}}^{\mathrm{single}}(\boldsymbol{r}, \alpha)$ (cf. Fig. 5.6a), act as the driving force for the local relaxation. The counter force is constituted by the straining of intermolecular bonds which can be modeled based on DFT as well (see below). In the starting configuration, all molecules reside in their respective unmodulated lattice sites $\boldsymbol{r}_p$, i.e., all displacements $\boldsymbol{u}_p^{(0)}$ are zero and the intermolecular bonds are assumed relaxed. However, in a non-commensurate layer the gradients $\nabla E_{\mathrm{mol-sub}}^{\mathrm{single}}(\boldsymbol{r}_p, \alpha)$ will generally not be zero, causing the start of the relaxation. No boundary conditions are applied, and a realistically large domain with thousands of molecules can be simulated without the presence of any periodic arrangement with respect to the substrate. However, in order to keep numerical costs manageable, the molecules are assumed to be rigid, flat-lying, and retain their orientational angles β within the unit cell throughout the energy minimization. Both assumptions are consistent with the STM measurements while the latter assumption also can be rationalized by the steric hindrance preventing the molecules from significant rotations in densely packed domains. The algorithm outlined above is implemented in MATLAB.

The potential energy $E_{\mathrm{mol-sub}}^{\mathrm{single}}(\boldsymbol{r}, \alpha)$ due to the interaction of a HBC molecule with the substrate has already been determined in Sec. 5.3. Therein, the adsorption height was optimized for each data point of the map. Therefore, a lateral displacement in the final relaxation algorithm automatically corresponds to effective three-dimensional adjustment of the molecular position. However, due to the relatively small adsorption height differences of less than 15 pm this minor effect is neglected in the intermolecular interaction. What is yet missing, in the picture of the Frenkel-Kontorova model, are the springs between the molecules. The original Novaco-McTague theory requires calculated or experimental data for the phonon dispersion in the adsorbate layer [14]. However, the phonon dispersion relations are usually not available for large aromatic molecules. Therefore, the intermolecular interaction is modeled based on DFT calculations as well in the next section.

There are various other approaches to achieve similar goals, most of which, however, are concerned with atomic adsorbates and cannot simply be applied here due to the α-dependence of $E^{\text{single}}_{\text{mol-sub}}(\boldsymbol{r}, \alpha)$. It has been argued that the orientation of incommensurate layers may be governed solely by symmetry principles [97, 98], but those would require the difference vector between the two closest-lying reciprocal adsorbate and substrate spots to be parallel to either a reciprocal adsorbate $\boldsymbol{a}^*_{1/2}$ or substrate vector $\boldsymbol{s}^*_{1/2}$. In the case of HBC, e.g., the $(\bar{1}, 6)_{\text{HBC}}$ order is the closest one to the $(0, 1)_{\text{EG}}$ order. It is a simple geometry problem, and will not be explicitly demonstrated, to show that the difference vector is not parallel to any of those vectors. Other models are more complex and include dynamical processes [148–150]. Such effects, especially thermodynamical ones are not needed to understand and describe the presented system. Rather, the algorithm proposed in the following represents a quasi-static relaxation within the overlayer. Another previous work on the epitaxy of HBC on graphite found a deviation from commensurate registry via *POWERGRID* similar to the one found here in experiments [36]. However, the calculation was based on a rigid lattice and a very small domain of 85 molecules. In the light of the previous discussion, the result can therefore be attributed to the finite size of the system.

5.5.1 Extraction of intermolecular forces from first principles calculations

In a modulated incommensurate overlayer, the bonds of a molecule to each of its nearest neighbors may be strained differently, longitudinally as well as transversally. In order to obtain intermolecular forces *per bond* from the DFT calculations provided by Dr. Matthes, the following has to be considered: In a 2D hexagonal lattice such as the one of the HBC monolayer, there are 3 times as many nearest-neighbor bonds as there are lattice points, or in other words, a unit cell containing one HBC molecule contains the binding energy of three nearest-neighbor bonds (*not six*). Due to the periodic boundary conditions in the

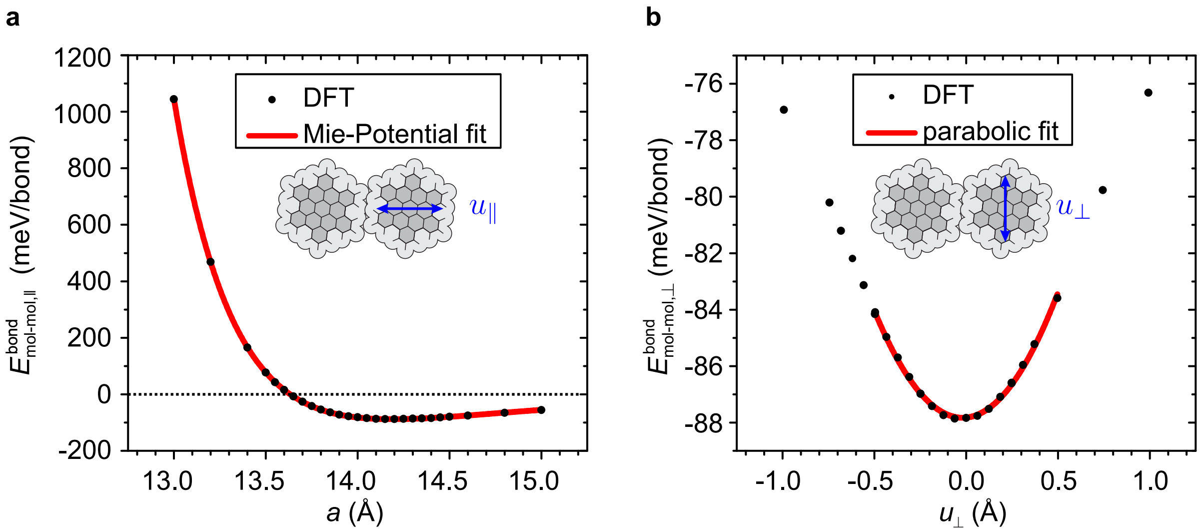

Figure 5.8: DFT-based potential energies (black dots) of a single nearest-neighbor bond between two HBC molecules for the case of a longitudinal strain (panel **a**) and a transversal strain of the bond (panel **b**). Both contributions are fitted separately with Equs. 5.2 and 5.5, respectively (red curves; see Tab. 5.2 for results).

DFT calculations, all of these bonds are included. Therefore, increasing the size of the DFT cell a with one molecule to calculate the energy cost due to the longer nearest-neighbor distances in fact corresponds to the cost of straining three nearest-neighbor bonds. Hence, all intermolecular binding energies obtained from Dr. Matthes are divided by a factor of three.

The equilibrium configuration of a free-standing HBC layer has been determined by Dr. Matthes to be a hexagonal cell with a lattice constant of a_0=14.15 Å and a molecular angle of $\beta_0 = 6°$. The overestimation of both values compared to the experimental ones of the LT structure (13.95 Å and 5.1°, respectively) is in a reasonable range so that straining of the bonds will be modeled with respect to the DFT equilibrium configuration and later applied to the experimental structure parameters by rigidly shifting the corresponding energy curves (see below).

Longitudinal strain

Figure 5.8a shows the resulting values for $E^{\mathrm{bond}}_{\mathrm{mol-mol}}(a)$ for the case of a simple size variation of the DFT cell around the equilibrium value of 14.15 Å, with the HBC molecule rotated to $\beta_0 = 6°$. This corresponds to a longitudinal (i.e., parallel) strain of a single intermolecular bond. The shape of the curve can be fitted very well with a Mie potential

$$E^{\mathrm{bond}}_{\mathrm{mol-mol},\parallel}\left(a\ [\text{Å}]\right)\ [\mathrm{meV}] = \left(\frac{c_1}{a}\right)^m - \left(\frac{c_2}{a}\right)^n, \tag{5.2}$$

with the fit result given in Tab. 5.2. Using $a' = a + \Delta a$ with $\Delta a = 0.2$ Å instead of

Table 5.2: Fit parameters of Equs. 5.2 and 5.5 for the curves in Fig. 5.8.

c_1 [Å]	c_2 [Å]	m	n	c_3
16.01(2)	19.32(5)	35.8(2)	16.5(2)	16.4(2)

a, shifts the curve to match the minimum to the experimentally found lattice constant. The shape of the curve allows the molecules to assume easily larger distances from one another while preserving the short-distance repulsion. Note that the standard deviation of nearest-neighbor distances was determined experimentally to be ≈ 0.3 Å which renders this difference significant. This is the reason why a simple 2D Frenkel-Kontorova model with harmonic springs would not be sufficient here.

Longitudinal displacements can now be accounted for: A molecule p shifted by $\boldsymbol{u}_p$ from its unmodulated lattice site $\boldsymbol{r}_p$, and a nearest neighbor q shifted by $\boldsymbol{u}_q$ from $\boldsymbol{r}_q$ cause a longitudinal deformation of their bond by the projection

$$u_{pq,\|} = (\boldsymbol{u}_p - \boldsymbol{u}_q) \cdot (\boldsymbol{r}_p - \boldsymbol{r}_q)/|\boldsymbol{r}_p - \boldsymbol{r}_q| =: (\boldsymbol{u}_p - \boldsymbol{u}_q) \cdot \hat{\boldsymbol{r}}_{pq} \tag{5.3}$$

and result in a bond energy of

$$E^{\text{bond}}_{\text{mol-mol},\|}(\boldsymbol{u}_p, \boldsymbol{u}_q) = \left(\frac{c_1}{a' + u_{pq,\|}}\right)^m - \left(\frac{c_2}{a' + u_{pq,\|}}\right)^n \tag{5.4}$$

Transversal strain

A transversal bond deformation (cf. inset of Fig. 5.8b) changes both the separation and the mutual orientation of the molecules. The energy contribution due to this strain with respect to the DFT equilibrium configuration is obtained as follows. The transversal mutual-displacement component of the molecules p and q, namely $u_{pq,\perp} = \sqrt{(\boldsymbol{u}_p - \boldsymbol{u}_q)^2 - u^2_{pq,\|}}$, from the equilibrium position can be considered in DFT with a size change of the single-molecule cell to $a = \sqrt{a_0^2 + u^2_{pq,\perp}}$ and a simultaneous rotation of the HBC molecule in the cell to an angle $\beta = \beta_0 + \arctan(u_{pq,\perp}/a_0)$. Such calculations were suggested to, and performed by, Dr. Matthes and Fig. 5.8b shows the corresponding values. They can be fitted satisfactorily within a displacement range of ±0.5 Å with a parabola:

$$E^{\text{bond}}_{\text{mol-mol},\perp}(\boldsymbol{u}_p, \boldsymbol{u}_q) = E_{\perp,0} + c_3 u^2_{pq,\perp}. \tag{5.5}$$

The fitted value of c_3 is given in Tab. 5.2 as well. Since the energy minimum per bond is already included in $E^{\text{bond}}_{\text{mol-mol},\|}$, the transversal contribution $E^{\text{bond}}_{\text{mol-mol},\perp}$ is simply $c_3 u^2_{\perp}$. With this, the total bond energy in dependence of individual displacements can be fully parametrized:

$$E^{\text{bond}}_{\text{mol}-\text{mol}}(\boldsymbol{u}_p, \boldsymbol{u}_q) = \left(\frac{c_1}{a' + u_{pq,\parallel}}\right)^m - \left(\frac{c_2}{a' + u_{pq,\parallel}}\right)^n + c_3 u^2_{pq,\perp}. \tag{5.6}$$

Total energy and gradients

Finally, the total adsorption energy $E^{\text{domain}}_{\text{total}}$ of a domain with N molecules that are individually displaced by $\boldsymbol{u}_p$ can be obtained by summing up the molecule-substrate contributions $E^{\text{single}}_{\text{mol}-\text{sub}}(\boldsymbol{r} + \boldsymbol{u}_p)$ and the contributions from each molecule due to the interaction with its nearest neighbors $E_{\text{mol}-\text{mol}}(\boldsymbol{u}_p, \{\boldsymbol{u}_q\})$, over all molecules. Note however, that due to the summing over molecules instead of bonds, each intermolecular bond (p, q) contributes twice to the total sum – once when molecule q is the neighbor of molecule p and vice versa the second time. Therefore, the intermolecular contribution per single molecule is half that of the bond energy: $E^{\text{single}}_{\text{mol}-\text{mol}}(\boldsymbol{u}_p, \boldsymbol{u}_q) = \frac{1}{2} E^{\text{bond}}_{\text{mol}-\text{mol}}(\boldsymbol{u}_p, \boldsymbol{u}_q)$. With this, the total domain energy is given by

$$E^{\text{domain}}_{\text{total}} = \sum_{p=1}^{N} \left[E^{\text{single}}_{\text{mol}-\text{sub}}(\boldsymbol{r}_p + \boldsymbol{u}_p, \alpha) + \frac{1}{2} \sum_q E^{\text{bond}}_{\text{mol}-\text{mol}}(\boldsymbol{u}_p, \boldsymbol{u}_q) \right]. \tag{5.7}$$

Note that the number of nearest-neighbors may change at the domain boundary, but that the second sum then simply runs over fewer neighbors and hence domain boundaries are automatically accounted for. Due to the attractive potential between the molecules there is no need to set any artificial boundary condition.

The advantage of this parametrization is the ability to analytically calculate the gradient of the total domain energy with respect to the individual displacement $\boldsymbol{u}_p$ of a molecule p and therefore the total force $-\nabla_p E^{\text{domain}}_{\text{total}} = -{\partial}/{\partial \boldsymbol{u}_p} E^{\text{domain}}_{\text{total}}$ that applies to the molecule:

$$\begin{aligned} -\nabla_p E^{\text{domain}}_{\text{total}} &= -\nabla_p E^{\text{single}}_{\text{mol}-\text{sub}} - \sum_q \nabla_p E^{\text{bond}}_{\text{mol}-\text{mol}}(\boldsymbol{u}_p, \boldsymbol{u}_q) \\ &= -\nabla_p E^{\text{single}}_{\text{mol}-\text{sub}} \\ &\quad - \sum_q \left\{ \left[\frac{-m c_1^m}{(a' + u_{pq,\parallel})^{m+1}} + \frac{-n c_2^n}{(a' + u_{pq,\parallel})^{n+1}} \right] \hat{\boldsymbol{r}}_{pq} + 2 c_3 u_{pq,\perp} \hat{\boldsymbol{r}}_{pq,\perp} \right\}, \end{aligned} \tag{5.8}$$

with the unit vector $\hat{\boldsymbol{r}}_{pq,\perp}$ perpendicular to the bond direction. For the same reason that the factor 1/2 was introduced in Equ. 5.7, i.e., because each nearest-neighbor bond appears twice in the sum, the same gradient $\nabla_p E^{\text{bond}}_{\text{mol}-\text{mol}}$ appears twice as well which cancels the factor 1/2 in Equ. 5.8. These total gradients can now be used in Equ. 5.1 to locally relax large incommensurate domains with computationally moderate means.

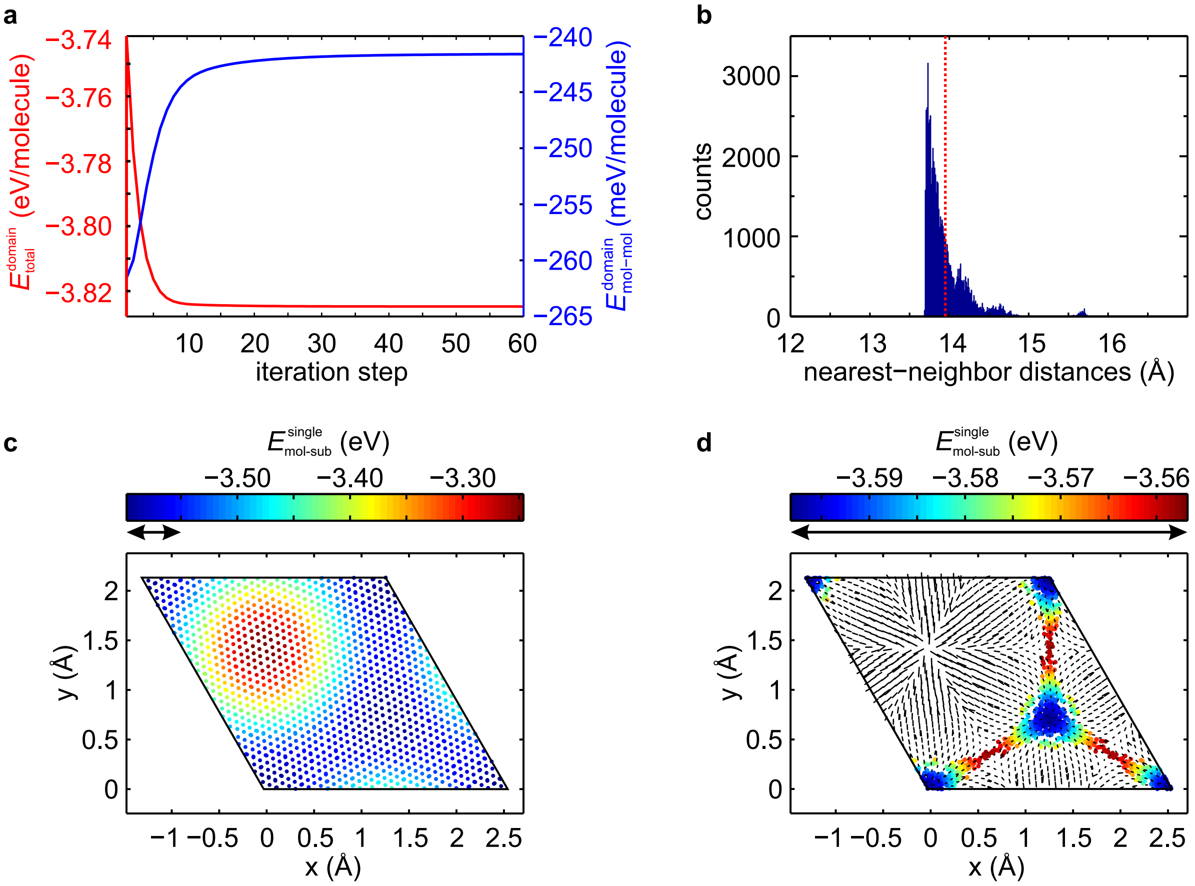

Figure 5.9: Relaxation of a domain with the LT structure (see text for details). **a**: Total domain energy per molecule and total intermolecular energy per molecule during the relaxation iteration. **b**: Histogram of the nearest-neighbor distances after the relaxation (initial value marked with dotted line). **c**: Molecular positions over the substrate unit cells before the relaxation, folded back into one substrate unit cell, with $E_{\mathrm{mol-sub}}^{\mathrm{single}}(\boldsymbol{r}_p)$ color-coded. **d**: Same plot as panel **c** after the relaxation. The final displacements from the original points in panel **c** to the final points in panel **d** are depicted and shortened for clarity. Note that the energy scale has shrunk due to the relaxation, marked by comparable arrows. Panels **c** and **d** only feature the innermost ≈ 10% of the domain's molecules for a better data point distinction.

5.5.2 Calculation versus experiment

The calculations described above are first performed and discussed using the experimentally determined LT structure of HBC on graphite in order to compare the results with the STM observations in Sec. 5.4, before being applied in the next section to explain the orientation of the overlayer altogether.

In order to simulate the relaxation of the LT structure, a hexagon-shaped domain containing 10981 molecules (diameter ≈ 170 nm) was initialized in the corresponding unmodulated configuration: a hexagonal lattice with $|\boldsymbol{a}_{1/2}| = 13.95$ Å, a unit cell orientation $\theta = -8.66°$ with respect to graphite and a molecular orientation $\beta = 5.1°$ within the unit cell (or

$\alpha = \theta + \beta = -3.56°$ with respect to the substrate). While the domain size could have been chosen smaller, this size has proved useful to prevent any notable influence of the domain boundaries to these and the following results. The iterative relaxation is performed until the total domain energy $E_{\text{total}}^{\text{domain}}$ has converged, approximately 85 meV/molecule below the initial value in this case (cf. Fig. 5.9a). At the same time, stress builds up within the HBC layer and converges as well, contributing about 20 meV/molecule.

As can be inferred already from the histogram of nearest-neighbor distances in the relaxed layer (cf. Fig. 5.9b), some molecules moved closer together down to the lattice constant of the reported commensurate structure, i.e., 13.7 Å, but many others ended up at larger distances as well. This shows that the HBC layer is not simply one consisting of many commensurate patches. The sharp cutoff at the "commensurate" value is due to the quasi-static relaxation algorithm – the molecules will simply not get closer because there is no such force once they reach the "commensurate" distance, with each lying in a corresponding minimum of $E_{\mathbf{mol-sub}}^{\mathbf{single}}$. Yet, the shape of the histogram is in good agreement to the one obtained experimentally (cf. Fig 5.7d), despite the broadening of the measured distribution due to defects and statistical errors of the localization algorithm.

An intuitive visualization of the relaxation process is given in Figs. 5.9c and 5.9d. They show the molecular (center) positions, folded back into one substrate unit cell with a color corresponding to the energy $E_{\mathbf{mol-sub}}^{\mathbf{single}}$ of their respective position. Only the innermost $\approx$ 10% of the domain's molecules are included in both panels so that groups of data points can still be distinguished. Nevertheless, in the initial configuration representing the unmodulated lattice with the LT lattice constant and orientation (cf. 5.9c), the entire unit cell is filled with spots due to the incommensurate relation between the HBC lattice and graphite. This explains visually that the domain energy simply corresponds to the average value of the entire map, i.e., the incommensurate energy. However, after the relaxation the molecules adopt more advantageous positions (cf. 5.9d). While by far not all occupy the lowest-energy registry above a carbon atom of graphite (blue areas), they have been driven towards them. Hence, the average energy $E_{\mathbf{mol-sub}}^{\mathbf{domain}}$ per molecule has decreased substantially, as can be judged from the energy scales as well. The balance of locally experienced gradients in $E_{\mathbf{mol-sub}}^{\mathbf{single}}$ and favorable interactions with the nearest-neighbors allowed many molecules to avoid energetically disadvantageous positions. This is also why a mere height modulation will not result in any significant epitaxial energy minimum, as has been reported before [85]. For any incommensurate orientation, the data points would still fill the entire unit cell in Fig. 5.9d without lateral displacements, leading to the domain's energy corresponding to the incommensurate energy. Moreover, Fig. 5.9d explains the absence of convoluted LEED spots in the vicinity of the specular spot. While the lateral displacements are significant (see below for quantitative results), the difference

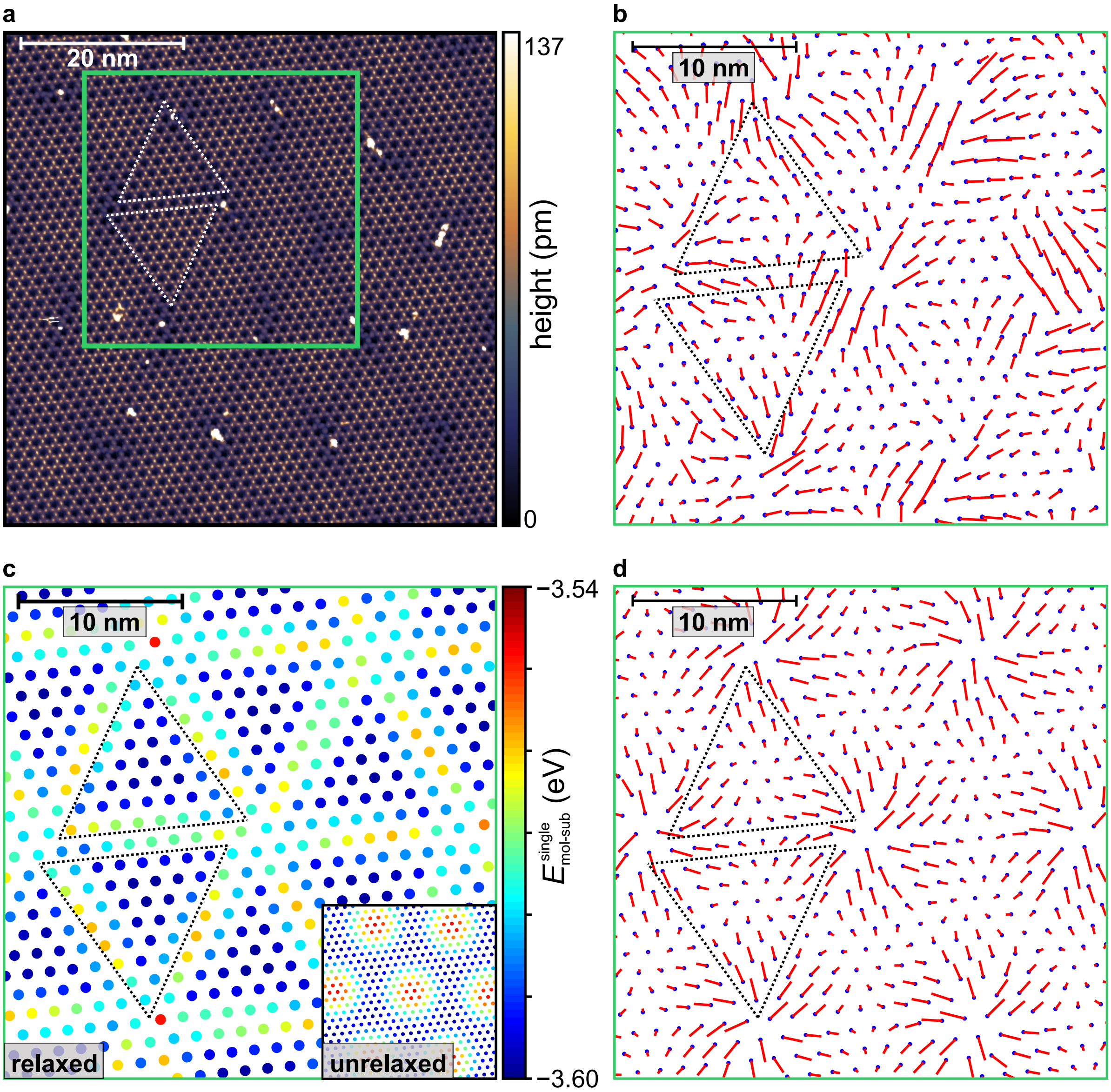

Figure 5.10: For comparison, panels **a** and **b** are re-plots from Fig. 5.7. **c**: Calculated, relaxed positions of HBC molecules, color-coded with $E^{\mathrm{single}}_{\mathrm{mol-sub}}(\boldsymbol{r}_p + \boldsymbol{u}_p)$. For the appearance before the relaxation see inset. **d**: HBC lattice before the relaxation (dots) and simulated molecular displacements (red lines; magnified by the same factor 15 as in panel **b**).

in adsorption heights diminishes proportionally to the energy scale to ≈ 2 pm. Hence, even for maximum values of $S_\perp$, the sensitivity with respect to such small perpendicular modulations is not sufficient for an observation of the corresponding spots.

The short black lines in Fig. 5.9d originate from the spots in 5.9c and point to the direction of the respective final spot positions after the relaxation – they have been shortened for a better overview. It is obvious that the molecules approximately “slid down the hill” according to the (negative) gradient of the $E^{\mathbf{single}}_{\mathbf{mol-sub}}(\boldsymbol{r})$ energy map (cf. Fig. 5.6a). This renders the second assumption at the end of Sec. 4.1.3 plausible with which the low energy dependence of a LEED pattern from such a structure was concluded.

Finally, the relaxed structure can be directly compared to the STM observations. Figs. 5.10a and 5.10b again show the Moiré pattern and experimentally determined molecular displacements from Fig. 5.7, respectively. Figure 5.10c displays the calculated positions of the relaxed LT structure, this time in absolute coordinates, with the final molecule-substrate potential energy $E^{\text{single}}_{\text{mol-sub}}(\boldsymbol{r}_p + \boldsymbol{u}_p)$ color-coded. The calculated molecular displacements are shown in Figure 5.10d, magnified by the same factor as the experimental ones in 5.10b. The similarities between the calculated patterns and their experimental counterparts are striking, including the slight chirality and especially compared to the sinusoidal Moiré pattern before the relaxation (cf. inset of Fig. 5.10c) which cannot explain the measurement. In addition to the successful application of the convolution approach in the Fourier analysis of this system, it is even more apparent in the context of this simulation that the measured displacements are the result of the HBC layer's interaction with the substrate lattice and follow rather regular patterns. Hence, they constitute static distortion waves (SDWs) as proposed by Novaco and McTague. Yet more importantly, the calculated mean displacement of 0.44 Å and the standard deviation of the nearest-neighbor distances of 0.29 Å are in excellent agreement with the experimentally determined values of 0.52 Å and 0.28 Å, respectively. Since these values depend on how the driving force, i.e., the corrugation of $E^{\textbf{single}}_{\textbf{mol-sub}}(\boldsymbol{r})$ scales in comparison to the intermolecular forces, both contribution are apparently described with a realistic relation to each other.

An additional conclusion can be drawn from the comparison of the calculated and experimental Moiré pattern. While the centers of the triangular regions in the STM image appear brightest, they correspond to the lowest-energy areas in the calculated pattern. As was stated before, the calculated adsorption height follows the energy map $E^{\text{single}}_{\text{mol-sub}}(\boldsymbol{r})$ in Fig. 5.6a proportionally. Hence, the (weak) brightness modulation in the STM is in fact reversed compared to the topology of the surface and must be a result of a modulated local density of states, with the lowest-lying molecules providing points of more efficient electron tunneling.

5.5.3 Prediction of the epitaxial orientation

The model described above is able to simulate the local relaxation of the LT structure at $\theta = -8.66°$ in remarkable consistency with the experiment. However, it can be used as well to understand why the HBC layer reproducibly growths with the same orientation with respect to graphite. For this, the relaxation is repeated with the same LT lattice constant as the starting configuration, but for varying unit cell orientations θ with respect

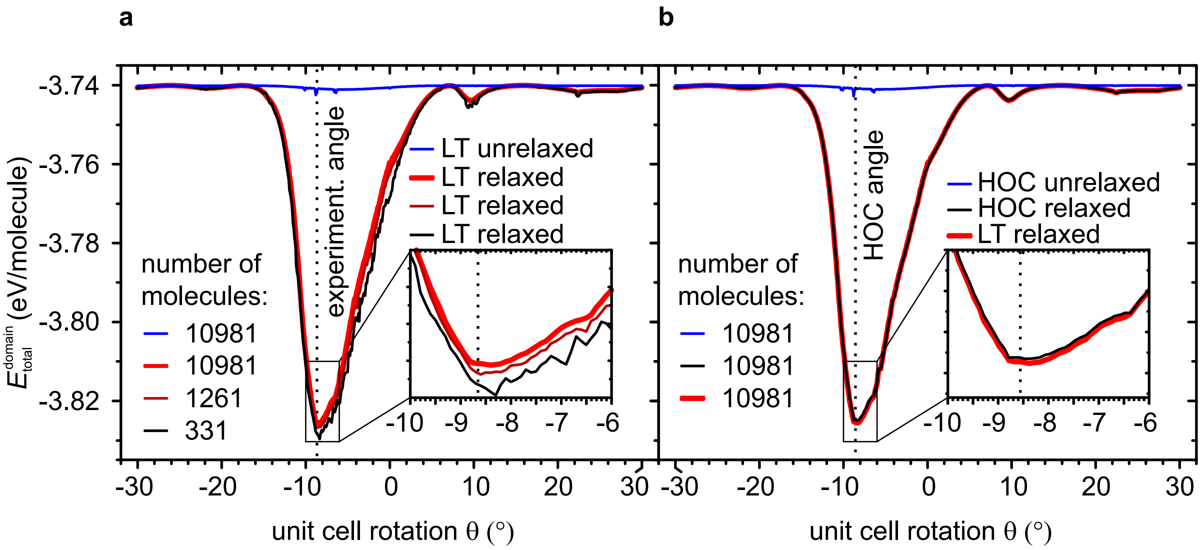

Figure 5.11: a: Total adsorption energy per molecule before (blue) and after relaxation (black to red) of HBC domains with different sizes, with the initial LT lattice constant of 13.95 Å. For better comparison, small offsets (increasing with decreasing domain size) due to domain-edge molecules have been corrected for the two smaller domains, using the values -6 meV and -14 meV. The experimental LT angle $\theta = -8.66°$ is marked by a dotted line. **b**: Similar calculations as in panel **a**, but with a lattice constant of 13.9552 Å (blue and black lines) that exactly produces a HOC coincidence at $\theta = -8.57°$ (dotted vertical line), being comparable but not identical to the measured LT structure. Apparently, a HOC coincidence in addition to local relaxation is not relevant in this case, with the curve being almost identical to the incommensurate (LT) one re-plotted from panel **a**.

to graphite, i.e., the domain is rotated over graphite and relaxed for each angle. The orientation $\beta = 5.1°$ of the molecules with respect to the rotating unit cell is kept fixed. The reasoning behind this condition is again the steric hindrance of the molecules in a dense monolayer due to the interlocked hydrogen atoms. The optimization of the entire domain's registry with the substrate is not of the same importance for the relaxed structures below as it is for the rigid, unrelaxed domains in Sec. 5.3. Due to the incommensurability of the HBC layer and the local relaxation, an initially disadvantageous registry of the entire domain is quickly compensated. However, in order to reduce the number of necessary iteration steps, the initial domains are rigidly optimized over one substrate unit cell as well.

The thick red curve in Fig. 5.11a is the corresponding result of such a series of relaxations, with an angular resolution of 0.1° and the same domain size as the previous single-θ calculation. It confirms that the total energy is indeed minimal for a unit cell orientation $\theta = -8.5(2)°$, matching the experiments very well and differing significantly from the commensurate value of -8.95°. Moreover, it affirms that the optimal total domain energy is substantially lower (by 85 meV/molecule) than the incommensurate energy. This can be seen in comparison to the blue curve which corresponds to the total domain energy before the relaxation. Note that the blue curve is basically identical to the unmodulated-layer curves in Fig. 5.6b, providing evidence that any minima in that figure are insignificant compared to the global minimum here, obtained through local relaxation.

The location of the minimum represents the orientation at which the molecules are able to take the most advantage from the molecule-substrate interaction before the intermolecular bonds counterbalance the relaxation. In this angular range $E_{\mathrm{mol-sub}}^{\mathrm{single}}(\boldsymbol{r})$ features large gradients, and the apparent Moiré period is especially long, allowing for larger displacements before strained nearest-neighbor bonds stop the relaxation. However, neither condition is fulfilled to its maximum, and the optimal angle can only be found by realistically describing the energy contributions and gradients.

The minimum's shape is of very different nature than an epitaxial energy minimum within the lattice epitaxy model. While the former is very broad, the latter is typically extremely narrow and becomes narrower with increasing domain size [58, 70]. In contrast, the minimum in Fig. 5.11a is very stable at various domain sizes (mostly smoother for larger domains), as shown with additional calculations in the same graph using smaller domains with the same LT starting configuration. Due to the increasing influence of the domain boundaries in the smaller domains and the normalization of the total energy using the total molecule number, small offsets in $E_{\mathrm{mol-mol}}^{\mathrm{domain}}$ would separate the total energy curves and were corrected in order to improve the comparability (see also the caption of Fig. 5.11). The offsets are due to the varying ratio of inner molecules and domain-edge molecules with fewer than six nearest-neighbors, with the latter contributing less intermolecular binding energy per molecule. It is also the domain-edge molecules that cause the "noise" in the curves of smaller domains. They can be displaced further than molecules surrounded by six nearest-neighbors. Hence, a domain containing a higher ratio of edge molecules is more sensitive to varying forces at the domain boundary, which change with θ.

In Sec. 5.3 it was argued that a rigid, unmodulated HBC monolayer does not experience any significant epitaxial energy minimum, even if a HOC coincidence is enforced (cf. also the blue curve in Fig. 5.11b). In order to demonstrate that the hypothetical existence of a HOC coincidence is of no advantage to the *relaxed* HBC layer either, the angle-dependent relaxation series was repeated under the same conditions, however, with the lattice constant slightly changed again to enforce a HOC coincidence close to the experimental LT structure. The result is given in form of the black curve in Fig. 5.11b, together with the thick red curve of the incommensurate relaxed structure from Fig. 5.11a for comparison. Both curves are practically indistinguishable and there is no additional energy minimum when the HOC condition is met as compared to the incommensurate relaxed layer. Hence, the formation of the static distortion waves (SDWs) constitutes the only mechanism behind the epitaxial energy minimum. Therefore, based on the insignificance of a HOC coincidence to the epitaxy of a monolayer of HBC on graphite even in the presence of SDWs, it can be concluded that this system has no reason to prefer such a special case and is indeed incommensurate.

All of the calculations were repeated for the RT structure as well with almost identical results in terms of the correct prediction of the epitaxial alignment, even without the inclusion of temperature effects (see Publication [P9] for details). Therefore there is no reason to believe at this point, that this effect is limited to low temperatures. However, an adaptation of the model may be necessary in the future to ensure reliability at higher temperatures.

6 General conclusions and outlook

The main objectives of this study were to focus on the often non-commensurate epitaxy of organic overlayers on inorganic substrates, to improve the understanding of the mechanisms driving the epitaxy in such cases, and to examine the layers' structural properties both in real and reciprocal space. Based on a complete overview of known types of epitaxy it was concluded that a variety of structures, including those explained by lattice epitaxy, may feature a modulation of the overlayer due to the substrate. Therefore, it was analyzed how such modulated layers affect diffraction experiments and the reciprocal space in general. The existing diffraction theory of modulated crystals is quite complicated. However, it was possible to extract essential properties of modulated crystal surfaces from a simplified theoretical approach deriving a corresponding LEED structure factor in Chap. 4, based on a more general theory from Ref. [73].

While LEED patterns and spot intensities generally change with the energy of the incident beam electrons and multiple scattering is normally necessary to calculate spot intensities, the pattern of modulated overlayers is remarkably insensitive to a change of this energy, in agreement with the derived structure factor, and multiple scattering only seems to play a minor role. This could be evidenced with both simplified calculations of electron scattering and experimental LEED data of epitaxial graphene on SiC(0001). Therefore, rather than viewing *modulated* overlayers as long-range reconstructions of the surface leading to large lattice bases and complex energy dependencies, they should be understood based on their primitive unit cells which are then regularly modulated by a function determined by the periodic substrate. This regular modulation manifests itself via a pattern of additional (satellite) spots with well-defined positions *and* intensities (the latter only approximately, for small modulation amplitudes). Due to the general character of the structure factor these assertions are expected to be valid for inorganic as well as organic overlayers. In fact, LEED experiments on non-commensurate organic overlayers, namely PbPc and HBC monolayers, on graphite corroborated many of the conclusions derived theoretically.

Additionally, an analytical method was proposed that combines the geometrical predictions of the structure factor, namely a convolution-based description of the LEED pattern, and the distortion correction of LEED patterns in order to extract highly precise epitaxy matrices. The advantage of this approach is that the substrate lattice can be indirectly fitted to a pattern which does not even include the first diffraction orders of the substrate. This cancels any scaling uncertainties of quantitative LEED analyses which normally remain even after a calibration and correction of distortions [P2]. Moreover, it was demonstrated that this method can even be applied to extract precise epitaxy matrices from fast Fourier-transformed (FFT) STM images of overlayers modulated by the substrate, since those feature the same convoluted spot patterns. A helpful side effect is the ability to use this information to correct linear distortions which are always present in STM images.

Finally, both the theoretical and methodological approaches from Chap. 4 could be applied to the interesting case of a monolayer HBC on graphite. In contrast to previous studies which reported a commensurate registry, the observation of convoluted spot patterns in LEED and STM FFTs, as well as the application of the suggested approach to fit the epitaxy matrix to such a pattern, proved that this system is neither commensurate nor a case of point-on-line (POL) or line-on-line (LOL) epitaxy. The analysis of the adsorption energy of HBC molecules with the substrate via DFT-scaled force-field calculations proved that no epitaxy concept based on strictly periodic lattices can explain the overlayer orientation, rendering the layer incommensurate yet epitaxial. Only the direct observation of lateral molecular displacements in the form of static distortion waves (SDWs) provided clues for the mechanism behind the epitaxy. Via modeling the intermolecular forces based on DFT calculations as well it was possible to simulate the local relaxation with a gradient approach which reproduced all experimental findings excellently and confirmed that the found overlayer orientation is indeed the energetically most favorable one. For the first time, this directly confirmed the stabilizing role of SDWs for incommensurate layers, as proposed by Novaco and McTague decades ago for rare gas overlayers [14]. Since the incommensurability, in combination with the local relaxation, results in the abandonment of strict translational symmetry, this system represents an example of aperiodic crystals in which the positions of the displaced components (molecules) can be studied directly.

HBC on graphite was especially suited to study this phenomenon due to the high symmetry of both the adsorbate and the substrate so that certain epitaxy types could be quickly excluded, due to the disk-like shape of HBC in the STM images allowing for an automatic localization of each molecule therein, and due to the relatively soft intermolecular bonds producing displacements large enough for direct detection. Yet, it is assumed that other incommensurate (organic) overlayers with not fully understood epitaxy [151, 152] may be governed by the same effect and could likewise be explained with the algorithm presented here. Moreover, in addition to implications of the LEED measurements on a monolayer of PbPc on graphite in Sec. 4.2.1, there is evidence in the literature that local relaxation is present in POL or LOL layers [79, 101] as well. It remains to be examined via an approach fully flexible in terms of local relaxations, such as the one introduced in this work, how the presence of both local relaxation and common sets of lattice lines influences the epitaxial orientation of an overlayer.

A Appendix

A.I Anisotropic Debye-Waller factor

The usual Debye-Waller factor from Equ. 4.27, before taking the average, modifies the static structure factor $F_0(\boldsymbol{S})$ [116]:

$$F(\boldsymbol{S}, t) = F_0(\boldsymbol{S}) \exp\left(-\frac{1}{2}\left(\boldsymbol{S} \cdot \boldsymbol{\delta}(t)\right)^2\right). \tag{A.1}$$

The prefactor of $\frac{1}{6}$ in Equ. 4.27 in comparison to $\frac{1}{2}$ in Equ. A.1 is a result of assuming isotropic three-dimensional displacements and calculating a time average [116].

However, the result is different for anisotropic displacements. Splitting both $\boldsymbol{S}$ and $\boldsymbol{\delta}(t)$ into their components parallel and perpendicular to the crystal surface, one obtains in the exponent $(\boldsymbol{S} \cdot \boldsymbol{\delta}(t))^2 = (\boldsymbol{S}_\parallel \cdot \boldsymbol{\delta}_\parallel(t) + S_\perp \delta_\perp(t))^2$. Since $\boldsymbol{S}_\perp$ and $\boldsymbol{\delta}_\perp(t)$ are always aligned, their scalar product is merely the product of their magnitudes. The parallel components are generally not aligned though. Due to the fixed nature of the momentum transfer $\boldsymbol{S}$ under evaluation, the time-dependent orientation angle $\phi(t)$ of $\boldsymbol{\delta}_\parallel(t)$ with respect to of $\boldsymbol{S}_\parallel$ changes rapidly. Therefore, the exponent becomes $S_\parallel^2 \delta_\parallel^2(t) \cos^2\phi(t) + 2S_\parallel S_\perp \delta_\parallel(t) \delta_\perp(t) \cos\phi(t) + S_\perp^2 \delta_\perp^2(t)$.

In a standard procedure for Debye-Waller factors, a time average on Equ. A.1 is equivalent to performing an angular average of the cosine factors if the orientation $\phi(t)$ is evenly distributed in the surface plane for sufficiently large time intervals. Therefore, the term containing $\cos\phi(t)$ is canceled in an average over a full circle. The average of $\cos^2\phi(t)$ results in $1/2\pi \int_0^{2\pi} \cos^2\phi \, d\phi = 1/2$. With this, the average of Equ. A.1 is

$$\langle F(\boldsymbol{S}, t)\rangle = F_0(\boldsymbol{S}) \exp\left(-\frac{1}{4} S_\parallel^2 \left\langle \delta_\parallel^2 \right\rangle\right) \exp\left(-\frac{1}{2} S_\perp^2 \left\langle \delta_\perp^2 \right\rangle\right) \tag{A.2}$$

For an unknown reason, the different prefactors due to averaging in two instead of three dimensions are not correctly accounted for in other works [102, 117].

A.II Epitaxy matrix properties

Epitaxy matrix in reciprocal space

Based on the definition of the reciprocal lattice vectors in Equ. 3.2, a lattice vector matrix $\underline{A} = \begin{bmatrix} \boldsymbol{a}_1 \\ \boldsymbol{a}_2 \end{bmatrix}$ as defined in Equ. 3.1 is connected to its reciprocal matrix $\underline{A}^* = \begin{bmatrix} \boldsymbol{a}_1^* \\ \boldsymbol{a}_2^* \end{bmatrix}$ by

$$\underline{A}\underline{A}^{*\top} = \underline{A}^*\underline{A}^\top = 2\pi\mathbb{1}. \tag{A.3}$$

Thus, the reciprocal vector matrix is $\underline{A}^* = 2\pi\underline{A}^{\top^{-1}}$. So an epitaxy matrix $\underline{C}$ in real space

$$\underline{A} = \underline{C}\underline{S}$$

translates into reciprocal space according to

$$\underline{A}^* = 2\pi\left[\underline{S}^\top\underline{C}^\top\right]^{-1} = \left[\underline{C}^\top\right]^{-1} 2\pi\left[\underline{S}^\top\right]^{-1} = \left[\underline{C}^\top\right]^{-1}\underline{S}^*$$

or

$$\underline{S}^* = \underline{C}^\top\underline{A}^*.$$

Behavior under linear transformations

An epitaxy matrix is *not* a transform matrix in the classic sense. A linear transform matrix $\underline{M}$ (rotation, reflection, shear, compression/dilation for example in an STM image) that transforms a column vector $\boldsymbol{v}$ according to $\boldsymbol{v}' = \underline{M}\boldsymbol{v}$, has to be transposed and applied to a lattice vector matrix from the right in order to transform both vectors accordingly:

$$\underline{A}\underline{M}^\top = \begin{bmatrix} \boldsymbol{a}_1 \\ \boldsymbol{a}_2 \end{bmatrix}\underline{M}^\top = \begin{bmatrix} \boldsymbol{a}_1' \\ \boldsymbol{a}_2' \end{bmatrix} \tag{A.4}$$

With this, it becomes clear that a linear transformation of an STM image leaves the epitaxy matrix $\underline{C}$ unchanged:

$$\underline{A}' = \underline{A}\underline{M}^\top = \underline{C}\underline{S}\underline{M}^\top = \underline{C}\underline{S}'.$$

This can be translated into reciprocal space with

$$\begin{aligned}\underline{A}'^* &= 2\pi(\underline{A}'^\top)^{-1} = 2\pi\left[(\underline{A}\underline{M}^\top)^\top\right]^{-1} = 2\pi\left[\underline{A}^\top\right]^{-1}\underline{M}^{-1} \\ &= \underline{A}^*\underline{M}^{-1} = \underline{C}^*\underline{S}^*\underline{M}^{-1} = \underline{C}^*\underline{S}'^*,\end{aligned}$$

meaning the epitaxial relation remains unchanged in real and reciprocal space when an STM or LEED image is linearly transformed (rotation, reflection, shear, compression/dilation).

When such a linear transform is applied only to the top structure $\underline{A}$ and the new epitaxy matrix due to this change is of interest it can easily be calculated by

$$\underline{C}_{\mathrm{new}} = \underline{CSM}^{\top}\underline{S}^{-1}. \tag{A.5}$$

This, for example, is relevant when a symmetrically equivalent domain on a symmetric substrate shall be found. With a rotation matrix

$$\underline{M}_{\mathrm{Rot}} = \begin{bmatrix} \cos(\alpha) & -\sin(\alpha) \\ \sin(\alpha) & \cos(\alpha) \end{bmatrix},$$

where α is the angle by which the adsorbate is rotated, and a reflection matrix

$$\underline{M}_{\mathrm{Refl}} = \begin{bmatrix} \cos(2\beta) & \sin(2\beta) \\ \sin(2\beta) & -\cos(2\beta) \end{bmatrix},$$

where β is the angle between $\boldsymbol{s}_1$ and the x-axis, all equivalent domains are attainable. If $\underline{S}$ is chosen such that $\boldsymbol{s}_1$ is parallel to the x-axis the reflection matrix, of course, simply becomes

$$\underline{M}_{\mathrm{Refl}} = \begin{bmatrix} 1 & 0 \\ 0 & -1 \end{bmatrix}.$$

Epitaxy matrix properties of point-on-line structures

The matrices transforming $\underline{C}$ in equation A.5 can be combined to a transformation matrix $\underline{T} = \underline{SM}^{\top}\underline{S}^{-1}$. For hexagonal lattices the transformation matrices for rotationally equivalent domains are summarized in table A.1. A POL structure "wrongly" defined with $\underline{C}$ consisting of only irrational numbers can be transformed by $\underline{T}_{60/120/240/300}$ to obtain an equivalent domain with an integer column. With $\angle(\boldsymbol{s}_1, \boldsymbol{s}_2) = 120°$ the transformation matrix elements obviously require line differences in $\underline{C}$ to be integers in such a case.

Table A.1: Matrices that transform epitaxy matrices according to Equ. A.5 for the case of hexagonal substrates ($\boldsymbol{s}_{1/2}$) and adsorbate lattice rotations of multiples of 60°. The condition for POL matrices with only irrational elements is given as well.

$\angle(\boldsymbol{s}_1, \boldsymbol{s}_2)$	$\underline{T}_{60}$	$\underline{T}_{120}$	$\underline{T}_{180}$	$\underline{T}_{240}$	$\underline{T}_{300}$	integer line...
120°	$\begin{bmatrix} 1 & 1 \\ \bar{1} & 0 \end{bmatrix}$	$\begin{bmatrix} 0 & 1 \\ \bar{1} & \bar{1} \end{bmatrix}$	$\begin{bmatrix} \bar{1} & 0 \\ 0 & \bar{1} \end{bmatrix}$	$\begin{bmatrix} \bar{1} & \bar{1} \\ 1 & 0 \end{bmatrix}$	$\begin{bmatrix} 0 & \bar{1} \\ 1 & 1 \end{bmatrix}$	**differences**
60°	$\begin{bmatrix} 0 & 1 \\ \bar{1} & 1 \end{bmatrix}$	$\begin{bmatrix} \bar{1} & 1 \\ \bar{1} & 0 \end{bmatrix}$	$\begin{bmatrix} \bar{1} & 0 \\ 0 & \bar{1} \end{bmatrix}$	$\begin{bmatrix} 0 & \bar{1} \\ 1 & \bar{1} \end{bmatrix}$	$\begin{bmatrix} 1 & \bar{1} \\ 1 & 0 \end{bmatrix}$	**sums**

A.III LEEDLab calibration factor for fast Fourier transforms

In LEEDLab, the calibration factor CF normally is determined from known samples and used to correctly scale LEED images in reciprocal space for all incident beam energies. In order to correctly scale STM FFTs in reciprocal space as well, it must be determined differently.

As a result of the definition of CF [P2], it corresponds to the ratio between a length in pixels in the image and the corresponding reciprocal length if the beam energy is set to 1 eV (with the offset in the LEEDLab interface set to zero): $CF[\mathrm{px}\,\text{Å}\,\sqrt{\mathrm{eV}}] = r[\mathrm{px}]/r^*[\text{Å}^{-1}]$. In an N [px] × N [px] STM image of an L [Å] × L [Å] area the highest measurable frequency with LEEDLab is $r^*_{\mathrm{max}} = \frac{1}{2}2\pi\frac{N}{L}$ due to the Nyquist theorem. At the same time, an FFT retains the number of pixels of the original image. Hence, the corresponding vector from the image center is $r[\mathrm{px}] = \frac{N}{2}$ and the correct LEEDLab calibration factor is

$$CF[\mathrm{px}\,\text{Å}\,\sqrt{\mathrm{eV}}] = \frac{N}{2}\frac{L[\text{Å}]}{\pi N} = \frac{L[\text{Å}]}{2\pi}. \tag{A.6}$$

A.IV Gradient of the molecule-substrate energy

The $E^{\mathrm{single}}_{\mathrm{mol-sub}}(\boldsymbol{r})$ maps resulting from DFT-scaled force-field calculations are stored as matrices for each alpha, i.e., in a kind of *relative* Cartesian coordinate system $E(x,y)$ which has to be mapped to the hexagonal substrate lattice $\underline{S}$: $E^*(u(x,y),v(x,y)) = E(x,y)$, with $\begin{pmatrix} u \\ v \end{pmatrix} = \underline{S}^\top \begin{pmatrix} x \\ y \end{pmatrix}$ due to the definition of $\underline{S}$ (cf. Appendix A.II). Because of this transformation, $\frac{\partial u}{\partial x} = S_{11}$, $\frac{\partial u}{\partial y} = S_{21}$, $\frac{\partial v}{\partial x} = S_{12}$, and $\frac{\partial v}{\partial x} = S_{22}$. In Matlab, it is easiest to perform the calculation of $\nabla_{xy}E(x,y)$ in the Cartesian system with MATLAB-provided functions first. It follows that

$$\begin{aligned} \nabla_{xy}E(x,y) = \nabla_{xy}E^*(u,v) = \begin{pmatrix} \frac{\partial}{\partial x} \\ \frac{\partial}{\partial y} \end{pmatrix} E^*(u,v) &= \begin{pmatrix} \frac{\partial}{\partial u}\frac{\partial u}{\partial x} + \frac{\partial}{\partial v}\frac{\partial v}{\partial x} \\ \frac{\partial}{\partial u}\frac{\partial u}{\partial y} + \frac{\partial}{\partial v}\frac{\partial v}{\partial y} \end{pmatrix} E^*(u,v) \\ &= \begin{pmatrix} S_{11}\frac{\partial}{\partial u} + S_{12}\frac{\partial}{\partial v} \\ S_{21}\frac{\partial}{\partial u} + S_{22}\frac{\partial}{\partial v} \end{pmatrix} E^*(u,v) = \underline{S}\nabla_{uv}E^*(u,v) \end{aligned} \tag{A.7}$$

Therefore, from the calculated gradient in the relative coordinate system $\nabla_{xy}E(x,y)$ the gradient in the coordinate system of the substrate can be obtained by $\nabla_{uv}E^*(u,v) = \underline{S}^{-1}\nabla_{xy}E(x,y)$. The resulting gradient correctly fits the map in Fig. 5.6a.

Bibliography

[1] C. K. Chiang, C. R. Fincher, Y. W. Park, A. J. Heeger, H. Shirakawa, E. J. Louis, S. C. Gau, and A. G. MacDiarmid: *Electrical Conductivity in Doped Polyacetylene.* Phys. Rev. Lett. **39**, 1098–1101 (1977).

[2] A. L. Briseno, S. C. B. Mannsfeld, M. M. Ling, S. Liu, R. J. Tseng, C. Reese, M. E. Roberts, Y. Yang, F. Wudl, and Z. Bao: *Patterning organic single-crystal transistor arrays.* Nature **444**, 913–917 (2006).

[3] Z. B. Wang, M. G. Helander, J. Qiu, D. P. Puzzo, M. T. Greiner, Z. M. Hudson, S. Wang, Z. W. Liu, and Z. H. Lu: *Unlocking the full potential of organic light-emitting diodes on flexible plastic.* Nat. Photonics **5**, 753–757 (2011).

[4] S. R. Forrest: *The path to ubiquitous and low-cost organic electronic appliances on plastic.* Nature **428**, 911–918 (2004).

[5] M. Cocchi: *Tuning the colour and efficiency of OLEDs.* In: A. Buckley (Ed.), *Organic Light-Emitting Diodes (OLEDs)*, Woodhead Publishing Series in Electronic and Optical Materials, chap. 10, 293–318. Woodhead Publishing (2013).

[6] S. Kim, H.-J. Kwon, S. Lee, H. Shim, Y. Chun, W. Choi, J. Kwack, D. Han, M. Song, S. Kim, S. Mohammadi, I. Kee, and S. Y. Lee: *Low-Power Flexible Organic Light-Emitting Diode Display Device.* Adv. Mater. **23**, 3511–3516 (2011).

[7] P. Görrn, M. Sander, J. Meyer, M. Kröger, E. Becker, H.-H. Johannes, W. Kowalsky, and T. Riedl: *Towards See-Through Displays: Fully Transparent Thin-Film Transistors Driving Transparent Organic Light-Emitting Diodes.* Adv. Mater. **18**, 738–741 (2006).

[8] K. M. Coakley and M. D. McGehee: *Conjugated Polymer Photovoltaic Cells.* Chem. Mater. **16**, 4533–4542 (2004).

[9] S. Reineke, M. Thomschke, B. Lüssem, and K. Leo: *White organic light-emitting diodes: Status and perspective.* Rev. Mod. Phys. **85**, 1245–1293 (2013).

[10] N. Karl: *Charge carrier transport in organic semiconductors.* Synth. Met. **133-134**, 649–657 (2003).

[11] H. Li, B. C.-K. Tee, J. J. Cha, Y. Cui, J. W. Chung, S. Y. Lee, and Z. Bao: *High-Mobility Field-Effect Transistors from Large-Area Solution-Grown Aligned* C_{60} *Single Crystals.* J. Am. Chem. Soc. **134**, 2760–2765 (2012).

[12] R. Hayakawa, M. Petit, T. Chikyow, and Y. Wakayama: *Analysis of carrier transport in quaterrylene thin film transistors formed by ultraslow vacuum deposition.* J. Appl. Phys. **104**, 024506 (2008).

[13] D. E. Hooks, T. Fritz, and M. D. Ward: *Epitaxy and Molecular Organization on Solid Substrates.* Adv. Mater. **13**, 227–241 (2001).

[14] A. D. Novaco and J. P. McTague: *Orientational Epitaxy - the Orientational Ordering of Incommensurate Structures.* Phys. Rev. Lett. **38**, 1286–1289 (1977).

[15] W. Demtröder: *Experimentalphysik 3: Atome, Moleküle und Festkörper*, vol. 3. Springer (2005).

[16] W. Brütting: *Physics of organic semiconductors.* Weinheim: Wiley-VCH-Verl. (2005).

[17] M. Gruenewald: *Organische Heteroepitaxie von PTCDA und SnPc auf einkristallinem Silber.* Diplomarbeit, Friedrich-Schiller-Universität Jena (2011).

[18] P. von Ragué Schleyer and H. Jiao: *What is aromaticity?* Pure Appl. Chem. **68**, 209–218 (1996).

[19] A. Heinfling, M. J. Martínez, A. T. Martínez, M. Bergbauer, and U. Szewzyk: *Transformation of Industrial Dyes by Manganese Peroxidases from Bjerkandera adusta and Pleurotus eryngii in a Manganese-Independent Reaction.* Appl. Environ. Microbiol. **64**, 2788–2793 (1998).

[20] W. Herbst and K. Hunger: *Industrial Organic Pigments: Production, Properties, Applications.* Wiley-VCH: Weinheim, 3rd edn. (2004).

[21] Y. Qiu, Y. Gao, P. Wei, and L. Wang: *Organic light-emitting diodes with improved hole-electron balance by using copper phthalocyanine/aromatic diamine multiple quantum wells.* Appl. Phys. Lett. **80**, 2628–2630 (2002).

[22] M. G. Walter, A. B. Rudine, and C. C. Wamser: *Porphyrins and phthalocyanines in solar photovoltaic cells.* J. Porphyrins Phthalocyanines **14**, 759–792 (2010).

[23] W. R. Scheidt and W. Dow: *Molecular Stereochemistry of Phthalocyanatozinc(II).* J. Am. Chem. Soc. **99**, 1101–1104 (1977).

[24] Y. Iyechika, K. Yakushi, I. Ikemoto, and H. Kuroda: *Structure of Lead Phthalocyanine (Triclinic Form).* Acta Crystallogr., Sect. B **38**, 766–770 (1982).

[25] Z. H. Cheng, L. Gao, Z. T. Deng, Q. Liu, N. Jiang, X. Lin, X. B. He, S. X. Du, and H.-J. Gao: *Epitaxial Growth of Iron Phthalocyanine at the Initial Stage on Au(111) Surface.* J. Phys. Chem. C **111**, 2656–2660 (2007).

[26] W. Chen, H. Huang, S. Chen, X. Y. Gao, and A. T. S. Wee: *Low-Temperature Scanning Tunneling Microscopy and Near-Edge X-ray Absorption Fine Structure Investigations of Molecular Orientation of Copper(II) Phthalocyanine Thin Films at Organic Heterojunction Interfaces.* J. Phys. Chem. C **112**, 5036–5042 (2008).

[27] H. Huang, S. L. Wong, W. Chen, and A. T. S. Wee: *LT-STM studies on substrate-dependent self-assembly of small organic molecules.* J. Phys. D: Appl. Phys. **44**, 464005 (2011).

[28] D. Hao, C. Song, Y. Ning, Y. Wang, L. Wang, X.-C. Ma, X. Chen, and Q.-K. Xue: *Self-assembly of manganese phthalocyanine on Pb(111) surface: A scanning tunneling microscopy study.* J. Chem. Phys. **134**, 154703 (2011).

[29] H. J. Räder, A. Rouhanipour, A. M. Talarico, V. Palermo, P. Samorì, and K. Müllen: *Processing of giant graphene molecules by soft-landing mass spectrometry.* Nat. Mater. **5**, 276–280 (2006).

[30] P. Beyer, T. Breuer, S. Ndiaye, A. Zykov, A. Viertel, M. Gensler, J. P. Rabe, S. Hecht, G. Witte, and S. Kowarik: *Lattice Matching as the Determining Factor for Molecular Tilt and Multilayer Growth Mode of the Nanographene Hexa*-peri-*hexabenzocoronene.* ACS Appl. Mater. Interfaces **6**, 21484–21493 (2014).

[31] T. Schmitz-Hübsch, F. Sellam, R. Staub, M. Törker, T. Fritz, C. Kübel, K. Müllen, and K. Leo: *Direct observation of organic–organic heteroepitaxy: perylene-tetracarboxylic-dianhydride on hexa*-peri-*benzocoronene on highly ordered pyrolytic graphite.* Surf. Sci. **445**, 358–367 (2000).

[32] F. Sellam, T. Schmitz-Hübsch, M. Toerker, S. Mannsfeld, H. Proehl, T. Fritz, K. Leo, C. Simpson, and K. Müllen: *LEED and STM investigations of organic–organic heterostructures grown by molecular beam epitaxy.* Surf. Sci. **478**, 113–121 (2001).

[33] P. Ruffieux, O. Gröning, M. Bielmann, C. Simpson, K. Müllen, L. Schlapbach, and P. Gröning: *Supramolecular columns of hexabenzocoronenes on copper and gold (111) surfaces.* Phys. Rev. B **66**, 073409 (2002).

[34] R. Forker, D. Kasemann, T. Dienel, C. Wagner, R. Franke, K. Müllen, and T. Fritz: *Electronic Decoupling of Aromatic Molecules from a Metal by an Atomically Thin Organic Spacer.* Adv. Mater. **20**, 4450–4454 (2008).

[35] A. Stabel, P. Herwig, K. Müllen, and J. P. Rabe: *Diodelike Current-Voltage Curves for a Single Molecule-Tunneling Spectroscopy with Submolecular Resolution of an Alkylated, peri-Condensed Hexabenzocoronene.* Angew. Chem. Int. Ed. Engl. **34**, 1609–1611 (1995).

[36] S. Mannsfeld: *Ordering in weakly bound molecular layers: Organic-inorganic and organic-organic heteroepitaxy.* Dissertation, Technische Universität Dresden (2004).

[37] G. E. Bacon: *Unit-cell dimensions of graphite.* Acta Crystallogr. **3**, 137–139 (1950).

[38] S. Schreiber: *Untersuchungen zum epitaktischen Wachstum von 3C-SiC bei Verwendung einer C60-Kohlenstoffquelle.* Dissertation, Universität Augsburg (2006).

[39] F. Varchon, P. Mallet, J.-Y. Veuillen, and L. Magaud: *Ripples in epitaxial graphene on the Si-terminated SiC(0001) surface.* Phys. Rev. B **77**, 235412 (2008).

[40] A. J. van Bommel, J. E. Crombeen, and A. van Tooren: *LEED and Auger electron observations of the SiC(0001) surface.* Surf. Sci. **48**, 463–472 (1975).

[41] F. Owman and P. Mårtensson: *The SiC(0001)*$6\sqrt{3} \times 6\sqrt{3}$ *reconstruction studied with STM and LEED.* Surf. Sci. **369**, 126–136 (1996).

[42] W. Chen, H. Xu, L. Liu, X. Gao, D. Qi, G. Peng, S. C. Tan, Y. Feng, K. P. Loh, and A. T. S. Wee: *Atomic structure of the 6H–SiC(0001) nanomesh.* Surf. Sci. **596**, 176–186 (2005).

[43] J. Hass, J. E. Millán-Otoya, P. N. First, and E. H. Conrad: *Interface structure of epitaxial graphene grown on 4H-SiC(0001).* Phys. Rev. B **78**, 205424 (2008).

[44] K. V. Emtsev, F. Speck, T. Seyller, L. Ley, and J. D. Riley: *Interaction, growth, and ordering of epitaxial graphene on SiC*{0001} *surfaces: A comparative photoelectron spectroscopy study.* Phys. Rev. B **77**, 155303 (2008).

[45] S. Kim, J. Ihm, H. J. Choi, and Y.-W. Son: *Origin of Anomalous Electronic Structures of Epitaxial Graphene on Silicon Carbide.* Phys. Rev. Lett. **100**, 176802 (2008).

[46] K. V. Emtsev, A. Bostwick, K. Horn, J. Jobst, G. L. Kellogg, L. Ley, J. L. McChesney, T. Ohta, S. A. Reshanov, J. Röhrl, E. Rotenberg, A. K. Schmid, D. Waldmann, H. B. Weber, and T. Seyller: *Towards wafer-size graphene layers by atmospheric pressure graphitization of silicon carbide.* Nat. Mater. **8**, 203–207 (2009).

[47] M. Meissner: *Organische Moleküle auf epitaktischem Graphen.* Diplomarbeit, Friedrich-Schiller-Universität Jena (2010).

[48] R. Forker and T. Fritz: *Optical differential reflectance spectroscopy of ultrathin epitaxial organic films.* Phys. Chem. Chem. Phys. **11**, 2142–2155 (2009).

[49] R. Forker, M. Gruenewald, and T. Fritz: *Optical differential reflectance spectroscopy on thin molecular films.* Annu. Rep. Prog. Chem., Sect. C: Phys. Chem. **108**, 34–68 (2012).

[50] J. Li, W.-D. Schneider, and R. Berndt: *Local density of states from spectroscopic scanning-tunneling-microscope images: Ag(111).* Phys. Rev. B **56**, 7656–7659 (1997).

[51] L. Gross, N. Moll, F. Mohn, A. Curioni, G. Meyer, F. Hanke, and M. Persson: *High-Resolution Molecular Orbital Imaging Using a p-Wave STM Tip.* Phys. Rev. Lett. **107**, 086101 (2011).

[52] H. S. Wong, X. Feng, K. Müllen, N. Chandrasekhar, and C. Durkan: *Channel selective tunnelling through a nanographene assembly.* Nanotechnology **23**, 095601 (2012).

[53] M. P. Seah and W. A. Dench: *Quantitative electron spectroscopy of surfaces: A standard data base for electron inelastic mean free paths in solids.* Surf. Interface Anal. **1**, 2–11 (1979).

[54] Available at `http://www.omicron.de/en/products/350/1154`.

[55] Available at `http://www.omicron.de/en/products/350/1155`.

[56] D. Nečas and P. Klapetek: *Gwyddion: an open-source software for SPM data analysis.* Cent. Eur. J. Phys. **10**, 181–188 (2012).

[57] S. W. Bailey, V. A. Frank-Kamenetskii, S. Goldsztaub, A. Kato, A. Pabst, H. Schulz, H. F. W. Taylor, M. Fleischer, and A. J. C. Wilson: *Report of the International Mineralogical Association (IMA)–International Union of Crystallography (IUCr) Joint Committee on Nomenclature.* Acta Crystallogr., Sect. A **33**, 681–684 (1977).

[58] S. C. B. Mannsfeld, K. Leo, and T. Fritz: *Line-on-Line Coincidence: A New Type of Epitaxy Found in Organic-Organic Heterolayers.* Phys. Rev. Lett. **94**, 056104 (2005).

[59] E. A. Wood: *Vocabulary of Surface Crystallography.* J. Appl. Phys. **35**, 1306–1312 (1964).

[60] A. C. Hillier and M. D. Ward: *Epitaxial interactions between molecular overlayers and ordered substrates.* Phys. Rev. B **54**, 14037–14051 (1996).

[61] A. Hoshino, S. Isoda, H. Kurata, and T. Kobayashi: *Scanning tunneling microscope contrast of perylene-3,4,9,10-tetracarboxylic-dianhydride on graphite and its application to the study of epitaxy.* J. Appl. Phys. **76**, 4113–4120 (1994).

[62] T. Fritz: *Molecular Architecture in Heteroepitaxially Grown Organic Thin Films.* Habilitation thesis, Technische Universität Dresden (1999).

[63] S. C. B. Mannsfeld and T. Fritz: *Analysis of the substrate influence on the ordering of epitaxial molecular layers: The special case of point-on-line coincidence.* Phys. Rev. B **69**, 075416 (2004).

[64] C. Wagner, R. Forker, and T. Fritz: *On the Origin of the Energy Gain in Epitaxial Growth of Molecular Films.* J. Phys. Chem. Lett. **3**, 419–424 (2012).

[65] S. Irie, A. Hoshino, K. Kuwamoto, S. Isoda, M. J. Miles, and T. Kobayashi: *Point-on-line coincidence in epitaxial growth of* $CuPcCl_{16}$ *on graphite.* Appl. Surf. Sci. **113-114**, 310–315 (1997).

[66] S. Mannsfeld, M. Toerker, T. Schmitz-Hübsch, F. Sellam, T. Fritz, and K. Leo: *Combined LEED and STM study of PTCDA growth on reconstructed Au(111) and Au(100) single crystals.* Org. Electron. **2**, 121–134 (2001).

[67] Y. Kaneda, M. E. Stawasz, D. L. Sampson, and B. A. Parkinson: *STM Investigations of the Two-Dimensional Ordering of Perylenetetracarboxylic Acid N-Alkyl-diimides on HOPG and* MoS_2 *Surfaces.* Langmuir **17**, 6185–6195 (2001).

[68] R. Franke, S. Franke, C. Wagner, T. Dienel, T. Fritz, and S. C. B. Mannsfeld: *Epitaxial nanolayers of quaterrylene: Influence of the substrate on the growth of the first and second monolayers.* Appl. Phys. Lett. **88**, 161907 (2006).

[69] S. R. Forrest and Y. Zhang: *Ultrahigh-vacuum quasiepitaxial growth of model van der Waals thin films. I. Theory.* Phys. Rev. B **49**, 11297–11308 (1994).

[70] S. C. B. Mannsfeld and T. Fritz: *Advanced Modelling of Epitaxial Ordering of Organic Layers on Crystalline Surfaces.* Mod. Phys. Lett. B **20**, 585–605 (2006).

[71] M. W. H. Braun, H. S. Kong, J. T. Glass, and R. F. Davis: *The role of geometric considerations in the diamond-cubic boron nitride heteroepitaxial system.* J. Appl. Phys. **69**, 2679–2681 (1991).

[72] J. P. McTague and A. D. Novaco: *Substrate-induced strain and orientational ordering in adsorbed monolayers.* Phys. Rev. B **19**, 5299–5306 (1979).

[73] S. Van Smaalen: *Incommensurate Crystallography.* IUCr monographs on crystallography. OUP Oxford (2007).

[74] J. D. Jackson: *Classical Electrodynamics.* Wiley, New York, 3rd edn. (1999).

[75] H. Hoshi, S. Fang, and Y. Maruyama: *Epitaxial growth of lead phthalocyanine film on KI crystal.* J. Appl. Phys. **73**, 3111–3113 (1993).

[76] M. Fendrich, M. Lange, C. Weiss, T. Kunstmann, and R. Möller: *N,N'-dimethylperylene-3,4,9,10-bis(dicarboximide) on alkali halide (001) surfaces.* J. Appl. Phys. **105**, 094311 (2009).

[77] C. Stadler, S. Hansen, I. Kröger, C. Kumpf, and E. Umbach: *Tuning intermolecular interaction in long-range-ordered submonolayer organic films.* Nat. Phys. **5**, 153–158 (2009).

[78] L. Kilian, U. Stahl, I. Kossev, M. Sokolowski, R. Fink, and E. Umbach: *The commensurate-to-incommensurate phase transition of an organic monolayer: A high resolution LEED analysis of the superstructures of NTCDA on Ag(111).* Surf. Sci. **602**, 2427–2434 (2008).

[79] C. Tröppner, T. Schmitt, M. Reuschl, L. Hammer, M. A. Schneider, F. Mittendorfer, J. Redinger, R. Podloucky, and M. Weinert: *Incommensurate Moiré overlayer with strong local binding: CoO(111) bilayer on Ir(100).* Phys. Rev. B **86**, 235407 (2012).

[80] A. D. Novaco: *Theory of orientational epitaxy in the self-consistent phonon approximation.* Phys. Rev. B **19**, 6493–6501 (1979).

[81] A. D. Novaco: *Theory of the structure and lattice dynamics of incommensurate solids: A classical treatment.* Phys. Rev. B **22**, 1645–1659 (1980).

[82] O. M. Braun and Y. S. Kivshar: *The Frenkel-Kontorova Model: Concepts, Methods, and Applications.* Springer Berlin (2004).

[83] F. C. Frank and J. H. van der Merwe: *One-dimensional dislocations. I. Static theory.* Proc. R. Soc. London, Ser. A **198**, 205–216 (1949).

[84] F. C. Frank and J. H. van der Merwe: *One-dimensional dislocations. II. Misfitting monolayers and oriented overgrowth.* Proc. R. Soc. London, Ser. A **198**, 216–225 (1949).

[85] M. B. Gordon: *Comment on "Complete Wetting on 'Strong' Substrates: Xe/Pt(111)".* Phys. Rev. Lett. **57**, 2094–2094 (1986).

[86] D. Fisher and R. D. Diehl: *Structural study of the submonolayer phases of potassium overlayers on Ni(100).* Phys. Rev. B **46**, 2512–2522 (1992).

[87] C. Fuselier, J. Raich, and N. Gillis: *Equilibrium configurations of commensurate adsorbed monolayers: Argon on graphite.* Surf. Sci. **92**, 667–680 (1980).

[88] S. K. Chatterjee: *Crystallography and the World of Symmetry.* Springer Series in Materials Science. Springer (2008).

[89] C. G. Shaw, S. C. Fain, and M. D. Chinn: *Observation of Orientational Ordering of Incommensurate Argon Monolayers on Graphite.* Phys. Rev. Lett. **41**, 955–957 (1978).

[90] H. I. Li, K. J. Franke, J. I. Pascual, L. W. Bruch, and R. D. Diehl: *Origin of Moiré structures in C60 on Pb(111) and their effect on molecular energy levels.* Phys. Rev. B **80**, 085415 (2009).

[91] P. Järvinen, S. K. Hämäläinen, K. Banerjee, P. Häkkinen, M. Ijäs, A. Harju, and P. Liljeroth: *Molecular Self-Assembly on Graphene on SiO_2 and h-BN Substrates.* Nano Lett. **13**, 3199–3204 (2013).

[92] D. V. Gruznev, A. V. Matetskiy, L. V. Bondarenko, O. A. Utas, A. V. Zotov, A. A. Saranin, J. P. Chou, C. M. Wei, M. Y. Lai, and Y. L. Wang: *Stepwise self-assembly of C_{60} mediated by atomic scale moiré magnifiers.* Nat. Commun. **4**, 1679 (2013).

[93] C. R. Woods, L. Britnell, A. Eckmann, R. S. Ma, J. C. Lu, H. M. Guo, X. Lin, G. L. Yu, Y. Cao, R. V. Gorbachev, A. V. Kretinin, J. Park, L. A. Ponomarenko, M. I. Katsnelson, Y. N. Gornostyrev, K. Watanabe, T. Taniguchi, C. Casiraghi, H.-J. Gao, A. K. Geim, and K. S. Novoselov: *Commensurate-incommensurate transition in graphene on hexagonal boron nitride.* Nat. Phys. **10**, 451–456 (2014).

[94] J.-Z. Wang, M. Lan, T.-N. Shao, G.-Q. Li, Y. Zhang, C.-Z. Huang, Z.-H. Xiong, X.-C. Ma, J.-F. Jia, and Q.-K. Xue: *STM study of a rubrene monolayer on Bi(001): Structural modulations.* Phys. Rev. B **83**, 235433 (2011).

[95] P. E. Burrows, Y. Zhang, E. I. Haskal, and S. R. Forrest: *Observation and modeling of quasiepitaxial growth of a crystalline organic thin film.* Appl. Phys. Lett. **61**, 2417–2419 (1992).

[96] S. R. Forrest, P. E. Burrows, E. I. Haskal, and F. F. So: *Ultrahigh-vacuum quasiepitaxial growth of model van der Waals thin films. II. Experiment.* Phys. Rev. B **49**, 11309–11321 (1994).

[97] F. Grey and J. Bohr: *A Symmetry Principle for Epitaxial Rotation.* Europhys. Lett. **18**, 717–722 (1992).

[98] E. Vives and P. A. Lindgård: *Theory and simulation of epitaxial rotation: Light particles adsorbed on graphite.* Phys. Rev. B **47**, 7431–7445 (1993).

[99] M. Böhringer, K. Morgenstern, W.-D. Schneider, M. Wühn, C. Wöll, and R. Berndt: *Self-assembly of 1-nitronaphthalene on Au(111).* Surf. Sci. **444**, 199–210 (2000).

[100] D.-M. Smilgies and E. J. Kintzel: *Epitaxial orientations of para-sexiphenyl platelets grown on alkali halide (001) surfaces.* Phys. Rev. B **79**, 235413 (2009).

[101] F. Bocquet, L. Nony, S. C. B. Mannsfeld, V. Oison, R. Pawlak, L. Porte, and C. Loppacher: *Inhomogeneous Relaxation of a Molecular Layer on an Insulator due to Compressive Stress.* Phys. Rev. Lett. **108**, 206103 (2012).

[102] W. Moritz, J. Landskron, and T. Grünberg: *Analysis of Thermal Vibrations and Incommensurate Layers by Low Energy Electron Diffraction.* Surf. Rev. Lett. **04**, 469–478 (1997).

[103] S. K. Hämäläinen, M. P. Boneschanscher, P. H. Jacobse, I. Swart, K. Pussi, W. Moritz, J. Lahtinen, P. Liljeroth, and J. Sainio: *Structure and local variations of the graphene moiré on Ir(111).* Phys. Rev. B **88**, 201406 (2013).

[104] W. Moritz: *LEED studies on modulated surface structures.* Z. Kristallogr. - Cryst. Mater. **230**, 37 (2014).

[105] A. T. N'Diaye, J. Coraux, T. N. Plasa, C. Busse, and T. Michely: *Structure of epitaxial graphene on Ir(111).* New J. Phys. **10**, 043033 (2008).

[106] H. C. Galloway, P. Sautet, and M. Salmeron: *Structure and contrast in scanning tunneling microscopy of oxides: FeO monolayer on Pt(111).* Phys. Rev. B **54**, R11145–R11148 (1996).

[107] K. Heinz: *LEED for complex surface structures.* Curr. Opin. Solid State Mater. Sci. **3**, 434–438 (1998).

[108] M. A. Van Hove, W. H. Weinberg, and C.-M. Chan: *Low-Energy Electron Diffraction: Experiment, Theory and Surface Structure Determination.* No. 6 in Springer Series in Surface Sciences. Springer, Berlin (1986).

[109] E. Bauer: *Interpretation of Low-Energy Electron Diffraction Patterns of Adsorbed Gases.* Phys. Rev. **123**, 1206–1208 (1961).

[110] C. Giovanardi, L. Hammer, and K. Heinz: *Ultrathin cobalt oxide films on Ir(100)-(1x1).* Phys. Rev. B **74**, 125429 (2006).

[111] W. H. Bragg and W. L. Bragg: *The Reflection of X-rays by Crystals.* Proc. R. Soc. London, Ser. A **88**, 428–438 (1913).

[112] A. H. Narten: *X-ray diffraction pattern and models of liquid benzene.* J. Chem. Phys. **67**, 2102–2108 (1977).

[113] O. Bryngdahl: *Moiré: Formation and interpretation.* J. Opt. Soc. Am. **64**, 1287–1294 (1974).

[114] I. Amidror and R. D. Hersch: *Fourier-based analysis of phase shifts in the superposition of periodic layers and their moiré effects.* J. Opt. Soc. Am. A **13**, 974–987 (1996).

[115] I. Amidror and R. D. Hersch: *Fourier-based analysis and synthesis of moirés in the superposition of geometrically transformed periodic structures.* J. Opt. Soc. Am. A **15**, 1100–1113 (1998).

[116] R. Gross and A. Marx: *Festkörperphysik.* De Gruyter Oldenbourg, Berlin (2014).

[117] U. Löffler, U. Muschiol, P. Bayer, K. Heinz, V. Fritzsche, and J. B. Pendry: *Determination of anisotropic vibrations by tensor LEED.* Surf. Sci. **331–333**, 1435–1440 (1995).

[118] A. W. Overhauser: *Observability of Charge-Density Waves by Neutron Diffraction.* Phys. Rev. B **3**, 3173–3182 (1971).

[119] W. Adlhart: *Dynamic structure factors for excitations in modulated structures.* Acta Crystallogr., Sect. A: Found. Adv. **38**, 498–504 (1982).

[120] J. D. Axe: *Debye-Waller factors for incommensurate structures.* Phys. Rev. B **21**, 4181–4190 (1980).

[121] H. Z. Cummins: *Experimental studies of structurally incommensurate crystal phases.* Phys. Rep. **185**, 211–409 (1990).

[122] A. S. Dawydow: *Quantenmechanik.* Barth, Leipzig, 8th edn. (1992).

[123] J. C. Nickel, C. Mott, I. Kanik, and D. C. McCollum: *Absolute elastic differential electron scattering cross sections for carbon monoxide and molecular nitrogen in the intermediate energy region.* J. Phys. B: At., Mol. Opt. Phys. **21**, 1867 (1988).

[124] T. W. Shyn and G. R. Carignan: *Angular distribution of electrons elastically scattered from gases: 1.5-400 eV on* N_2*. II.* Phys. Rev. A **22**, 923–929 (1980).

[125] H. Tanaka, S. K. Srivastava, and A. Chutjian: *Absolute elastic differential electron scattering cross sections in the intermediate energy region. IV. CO.* J. Chem. Phys. **69**, 5329–5333 (1978).

[126] R. D. DuBois and M. E. Rudd: *Differential cross sections for elastic scattering of electrons from argon, neon, nitrogen and carbon monoxide.* J. Phys. B: At. Mol. Phys. **9**, 2657 (1976).

[127] D. Rolles, R. Díez Muiño, F. J. García de Abajo, C. S. Fadley, and M. A. Van Hove: *Elastic scattering of low-energy electrons by randomly oriented and aligned molecules: Influence of full non-spherical potentials.* J. Electron Spectrosc. Relat. Phenom. **114-116**, 107–113 (2001).

[128] D. D. Reid and J. M. Wadehra: *Differential cross section surfaces for low energy scattering of electrons and positrons from rare gas atoms.* Hyperfine Interact. **89**, 435–444 (1994).

[129] A. Masek: *Optische Spektroskopie und LEED an PbPc auf Graphen.* Bachelor thesis, Friedrich Schiller University Jena (2014).

[130] A. Weisskopf: *Scanning tunneling microscopy and spectroscopy of PbPc on graphite(0001).* Bachelor thesis, Friedrich Schiller University Jena (2015).

[131] K. Momma and F. Izumi: *VESTA 3 for three-dimensional visualization of crystal, volumetric and morphology data.* J. Appl. Cryst. **44**, 1272–1276 (2011).

[132] B. T. Kelly: *Thermal vibration amplitudes of carbon atoms in the graphite lattice parallel to the basal planes.* J. Nucl. Mater. **34**, 189–192 (1970).

[133] F. Varchon, P. Mallet, L. Magaud, and J.-Y. Veuillen: *Rotational disorder in few-layer graphene films on 6H-SiC(000-1): A scanning tunneling microscopy study.* Phys. Rev. B **77**, 165415 (2008).

[134] T. Hahn and A. Vos: *International tables for crystallography. Volume A, Space-group symmetry.* Kluwer Academic Publishers, Dordrecht, 3 edn. (1992).

[135] C. Hammond: *The Basics of Crystallography and Diffraction.* International Union of Crystallography Texts on Crystallography. OUP/International Union of Crystallography (1997).

[136] W. S. Yang and F. Jona: *Missing spots in low-energy electron-diffraction patterns.* Phys. Rev. B **29**, 899–906 (1984).

[137] J. Janczak and R. Kubiak: *Two isomorphous complexes: di-chloro-[phthalocyaninato(2-)]-tin(IV) and di-chloro-[phthalocyaninato(2-)]-germanium(IV).* Acta Crystallogr., Sect. C **59**, m237–m240 (2003).

[138] S. Kera, H. Fukagawa, T. Kataoka, S. Hosoumi, H. Yamane, and N. Ueno: *Spectroscopic evidence of strong π interorbital interaction in a lead-phthalocyanine bilayer film attributed to the dimer nanostructure.* Phys. Rev. B **75**, 121305 (2007).

[139] U. Zimmermann and N. Karl: *Epitaxial growth of coronene and hexa*-peri-*benzocoronene on MoS_2(0001) and graphite (0001): a LEED study of molecular size effects.* Surf. Sci. **268**, 296–306 (1992).

[140] P. Samorí, N. Severin, C. D. Simpson, K. Müllen, and J. P. Rabe: *Epitaxial Composite Layers of Electron Donors and Acceptors from Very Large Polycyclic Aromatic Hydrocarbons.* J. Am. Chem. Soc. **124**, 9454–9457 (2002).

[141] U. Bardi, S. Magnanelli, and G. Rovida: *LEED Study of Benzene and Naphthalene Monolayers Adsorbed on the Basal Plane of Graphite.* Langmuir **3**, 159–163 (1987).

[142] R. Forker, T. Dienel, T. Fritz, and K. Müllen: *Optical evidence for substrate-induced growth of ultrathin hexa-peri-hexabenzocoronene films on highly oriented pyrolytic graphite.* Phys. Rev. B **74**, 165410 (2006).

[143] C. A. Schneider, W. S. Rasband, and K. W. Eliceiri: *NIH Image to ImageJ: 25 years of image analysis.* Nat. Methods **9**, 671–675 (2012).

[144] Y. Baskin and L. Meyer: *Lattice Constants of Graphite at Low Temperatures.* Phys. Rev. **100**, 544–544 (1955).

[145] T. A. Halgren: *Merck molecular force field. II. MMFF94 van der Waals and electrostatic parameters for intermolecular interactions.* J. Comput. Chem. **17**, 520–552 (1996).

[146] R. Pushpa and S. Narasimhan: *Stars and stripes. Nanoscale misfit dislocation patterns on surfaces.* Pure Appl. Chem. **74**, 1663–1671 (2002).

[147] A. N. Kolmogorov and V. H. Crespi: *Registry-dependent interlayer potential for graphitic systems.* Phys. Rev. B **71**, 235415 (2005).

[148] E. Bitzek, P. Koskinen, F. Gähler, M. Moseler, and P. Gumbsch: *Structural Relaxation Made Simple.* Phys. Rev. Lett. **97**, 170201 (2006).

[149] M. M. van Wijk, A. Schuring, M. I. Katsnelson, and A. Fasolino: *Moiré Patterns as a Probe of Interplanar Interactions for Graphene on h-BN.* Phys. Rev. Lett. **113**, 135504 (2014).

[150] D. Mandelli, A. Vanossi, N. Manini, and E. Tosatti: *Friction Boosted by Equilibrium Misalignment of Incommensurate Two-Dimensional Colloid Monolayers.* Phys. Rev. Lett. **114**, 108302 (2015).

[151] S. Gärtner, B. Fiedler, O. Bauer, A. Marele, and M. M. Sokolowski: *Lateral ordering of PTCDA on the clean and the oxygen pre-covered Cu(100) surface investigated by scanning tunneling microscopy and low energy electron diffraction.* Beilstein J. Org. Chem. **10**, 2055–2064 (2014).

[152] T. Huempfner, F. Sojka, R. Forker, and T. Fritz: *Growth of coronene on (100)- and (111)-surfaces of fcc-crystals.* Surf. Sci. **639**, 80–88 (2015).

Publications

[P1] M. Meissner, M. Gruenewald, F. Sojka, C. Udhardt, R. Forker, and T. Fritz: *Highly ordered growth of PTCDA on epitaxial bilayer graphene.* Surf. Sci. **606**, 1709–1715 (2012).

[P2] F. Sojka, M. Meissner, C. Zwick, R. Forker, and T. Fritz: *Determination and correction of distortions and systematic errors in low-energy electron diffraction.* Rev. Sci. Instrum. **84**, 015111 (2013).

[P3] M. Gruenewald, K. Wachter, M. Meissner, M. Kozlik, R. Forker, and T. Fritz: *Optical and electronic interaction at metal-organic and organic-organic interfaces of ultra-thin layers of PTCDA and SnPc on noble metal surfaces.* Org. Electron. **14**, 2177–2183 (2013).

[P4] F. Sojka, M. Meissner, C. Zwick, R. Forker, M. Vyshnepolsky, C. Klein, M. Horn-von Hoegen, and T. Fritz: *To tilt or not to tilt: Correction of the distortion caused by inclined sample surfaces in low-energy electron diffraction.* Ultramicroscopy **133**, 35–40 (2013).

[P5] R. Forker, J. Peuker, M. Meissner, F. Sojka, T. Ueba, T. Yamada, H. S. Kato, T. Munakata, and T. Fritz: *The Complex Polymorphism and Thermodynamic Behavior of a Seemingly Simple System: Naphthalene on Cu(111).* Langmuir **30**, 14163–14170 (2014).

[P6] M. Gruenewald, C. Sauer, J. Peuker, M. Meissner, F. Sojka, A. Schöll, F. Reinert, R. Forker, and T. Fritz: *Commensurism at electronically weakly interacting phthalocyanine/PTCDA heterointerfaces.* Phys. Rev. B **91**, 155432 (2015).

[P7] M. Gruenewald, J. Peuker, M. Meissner, F. Sojka, R. Forker, and T. Fritz: *Impact of a molecular wetting layer on the structural and optical properties of tin(II)-phthalocyanine multilayers on Ag(111).* Phys. Rev. B **93**, 115418 (2016).

[P8] R. Forker, T. Dienel, A. Krause, M. Gruenewald, M. Meissner, T. Kirchhuebel, O. Gröning, and T. Fritz: *Optical transition energies of isolated molecular monomers and weakly interacting two-dimensional aggregates.* Phys. Rev. B **93**, 165426 (2016).

[P9] M. Meissner, F. Sojka, L. Matthes, F. Bechstedt, X. Feng, K. Müllen, S. C. B. Mannsfeld, R. Forker, and T. Fritz: *Flexible 2D Crystals of Polycyclic Aromatics Stabilized by Static Distortion Waves.* ACS Nano **10**, 6474–6483 (2016).

[P10] F. Sojka, M. Meissner, T. Yamada, T. Munakata, R. Forker, and T. Fritz: *Naphthalene's Six Shades on Graphite: A Detailed Study on the Polymorphism of an Apparently Simple System.* J. Phys. Chem. (submitted 2016).

Abbreviations

AFM	atomic force microscopy
DFT	density functional theory
DRS	differential reflectance spectroscopy
EG	epitaxial graphene
FFT	fast Fourier transform
HBC	hexa-*peri*-hexabenzocoronene
HOC	higher-order commensurate
LDOS	local density of states
LEED	low-energy electron diffraction
LOL	line-on-line
MCP	microchannel plate
ML	monolayer
NG	natural graphite
NM theory	Novaco-McTague theory
OFET	organic field effect transistor
OLED	organic light-emitting diode
OMBE	organic molecular beam epitaxy
PAH	polycyclic aromatic hydrocarbon
PbPc	lead phthalocyanine
POL	point-on-line
RHEED	reflection high-energy electron diffraction
SDW	static distortion wave
STM	scanning tunneling microscopy
STS	scanning tunneling spectroscopy
TED	transmission electron diffraction
TEM	transmission electron microscope
UHV	ultra-high vacuum

Acknowledgments / Danksagung

An dieser Stelle möchte ich mich bei den vielen Menschen bedanken, die mich auf die eine oder andere Weise bei der Erstellung dieser Arbeit unterstützt haben. Allen voran Prof. Dr. Torsten Fritz, der es mir ermöglicht hat, das Feld organischer Molekülschichten kennenzulernen und durch seine direkte Betreuung und umgängliche Art immer ein offenes Ohr bei Problemen jedweder Art hatte. Außerdem habe ich durch ihn und den Deutschen Akademischen Austauschdienst die Möglichkeit erhalten, 3 Monate in Japan zu forschen, was mein wissenschaftliches und privates Lebens nachhaltig bereichert hat. In diesem Zusammenhang bin ich auch Prof. Dr. Toshiaki Munakata und seiner Arbeitsgruppe, inbesondere Assistent Prof. Dr. Takashi Yamada, für ihre Gastfreundschaft und Unterstützung zu Dank verpflichtet. Bei Dr. Roman Forker möchte ich mich unter anderem bedanken für seine stets freundliche und wertvolle Unterstützung im anfänglichen Kennenlernen der Technik, beim Verständnis physikalischer Konzepte, beim Verfeinern des Schreibens wissenschaftlicher Abhandlungen und für das Vorbereiten der Messungen in Japan, die hier vorgestellt wurden. Dr. Bernd Schröter hat mich bereits vor und während der Diplomarbeit mit den Feldern der Vakuumphysik, dünnen Schichten und der Elektronenbeugung vertraut gemacht und mir damit den Einstieg in dieses interessante Feld erst ermöglicht. Dafür möchte ich ihm herzlich danken. Besonders bedanken möchte ich mich auch bei Dr. Lars Matthes, dessen physikalische Kenntnisse mir stets Vorbild und Hilfe waren, und dessen sportliche Ambitionen mich auch abseits der Arbeit zu Höherem antreiben - manchmal.

Meine Kollegen in der Arbeitsgruppe sind mir über die Jahre nicht nur ans Herz gewachsen, sie haben auch wesentlich zum Erfolg meiner Arbeit beigetragen. Auf den Erfahrungsschatz und die Hilfsbereitschaft der technischen Mitarbeiter Helga Rudolph, Uwe Eberhardt, Silke Frunzke, Holger Mühlig und Stefan Prass war immer Verlass. Mit allen Doktoranden konnte ich stets ideenreiche Diskussionen führen. Besonders danken möchte ich hierbei Falko Sojka für die enge Zusammenarbeit im Rahmen der Anwendung von LEEDLab auf neue Gebiete, Marco Grünewald für das bereitwillige Teilen seiner Expertise in optischen Messungen und Christian Zwick für die Frage: “Ist das Gleitsymmetrie?”, seine Beratungen in grafischem Design, sowie seine moralische Unterstützung. Dafür und mehr mein herzliches Dankeschön an die erwähnten und alle weiteren Arbeitsgruppenmitglieder!

Abseits der Fachwelt möchte ich den Anteil meiner gesamten Familie, aber allen voran meiner Eltern anerkennen, die mich mein ganzes Leben selbstlos und aufopferungsvoll unterstützt und mir alle großen Erfahrungen und Wege ermöglicht haben, die mich letztlich an diesen Punkt führten. Meine Schwester war mir lange Zeit Weggefährtin zur Promotion und hatte so eine besondere Perspektive, durch die sie mir stets eine Hilfe sein konnte. Unsere gemeinsamen, motivationssteigernden Schreib-Sitzungen werden mir unvergesslich bleiben. Meine Schwiegereltern in spe haben trotz eigenem nie enden wollenden Arbeitspensum immer positive und ermutigende Worte gefunden und zu meinem leiblichen Wohl beigetragen. Vielen Dank für euer aller Unterstützung!

Zu guter Letzt bin ich unendlich dankbar für meine Verlobte, die mich nun schon während meiner zweiten großen Abschlussarbeit unterstützt hat und immer für mich da war, nach guten wie nach schlechten Messungen.

Affidavit / Ehrenwörtliche Erklärung

Ich erkläre hiermit ehrenwörtlich, dass ich die vorliegende Arbeit selbständig, ohne unzulässige Hilfe Dritter und ohne Benutzung anderer als der angegebenen Hilfsmittel und Literatur angefertigt habe. Die aus anderen Quellen direkt oder indirekt übernommenen Daten und Konzepte sind unter Angabe der Quelle gekennzeichnet.

Bei der Auswahl und Auswertung folgenden Materials haben mir die nachstehend aufgeführten Personen in der jeweils beschriebenen Weise unentgeltlich geholfen:

1. Dr. Lars Matthes, durch die Ausführung von Dichtefunktional-Berechnungen, die ich für die Erstellung des Relaxationsmodells in Kapitel 5 verwendet habe, und durch den überwiegenden Teil der Anpassung des Programms zur Berechnung von Doppelstreuung in Abschnitt 4.2.2,
2. Falko Sojka, durch die Anpassung und Bereitstellung einer Version von LEEDLab, um die molekularen Auslenkungen in Abschnitt 5.4 zu vermessen,
3. Christian Zwick, durch die Durchführung und grafische Aufbereitung der Messung in Abb. 4.11,
4. Prof. Dr. Torsten Fritz als betreuender Hochschullehrer.

Weitere Personen waren an der inhaltlich-materiellen Erstellung der vorliegenden Arbeit nicht beteiligt. Insbesondere habe ich hierfür nicht die entgeltliche Hilfe von Vermittlungs- bzw. Beratungsdiensten (Promotionsberater oder andere Personen) in Anspruch genommen. Niemand hat von mir unmittelbar oder mittelbar geldwerte Leistungen für Arbeiten erhalten, die im Zusammenhang mit dem Inhalt der vorgelegten Dissertation stehen.

Die Arbeit wurde bisher weder im In- noch im Ausland in gleicher oder ähnlicher Form einer anderen Prüfungsbehörde vorgelegt.

Die geltende Promotionsordnung der Physikalisch-Astronomischen Fakultät ist mir bekannt.

Ich versichere ehrenwörtlich, dass ich nach bestem Wissen die reine Wahrheit gesagt und nichts verschwiegen habe.

Jena, den 23. September 2016 ....

Curriculum vitae / Lebenslauf

Persönliche Daten

Name	Meißner
Vorname	Matthias
Geburtsdatum	15.07.1984
Geburtsort	Berlin-Marzahn
Nationalität	Deutsch

Ausbildung

09/1991-06/1995	Käthe-Kollwitz-Grundschule, Nordhausen, Deutschland
09/1995-06/2001	Wilhelm-v.-Humboldt-Gymnasium, Nordhausen, Deutschland
08/2001-05/2002	Somerset High School in Somerset, Kentucky, USA (Austauschschüler); Abschluss: “high school diploma”
09/2002-06/2004	Wilhelm-v.-Humboldt-Gymnasium, Nordhausen, Deutschland
2004	Abitur
10/2004-06/2005	Grundwehrdienst
10/2005-12/2010	Studium, Physik, Friedrich-Schiller-Universität, Jena, Deutschland
14.12.2010	Hochschulabschluss als Diplomphysiker, Friedrich-Schiller-Universität, Jena, Deutschland

Berufliche Tätigkeit

01/2011-03/2016	Wissenschaftlicher Mitarbeiter, Institut für Festkörperphysik, Friedrich-Schiller-Universität, Jena, Deutschland

Jena, den 23. September 2016 ....